REPORT DOCUMENTATION PAGE

1. REPORT DATE *(DD-MM-YYYY)*	2. REPORT TYPE	3. DATES COVERED *(From - To)*

4. TITLE AND SUBTITLE

5a. CONTRACT NUMBER

5b. GRANT NUMBER

5c. PROGRAM ELEMENT NUMBER

6. AUTHOR(S)

5d. PROJECT NUMBER

5e. TASK NUMBER

5f. WORK UNIT NUMBER

7. PERFORMING ORGANIZATION NAME(S) AND ADDRESS(ES)

8. PERFORMING ORGANIZATION REPORT NUMBER

9. SPONSORING/MONITORING AGENCY NAME(S) AND ADDRESS(ES)

10. SPONSOR/MONITOR'S ACRONYM(S)

11. SPONSOR/MONITOR'S REPORT NUMBER(S)

12. DISTRIBUTION/AVAILABILITY STATEMENT

13. SUPPLEMENTARY NOTES

14. ABSTRACT

15. SUBJECT TERMS

16. SECURITY CLASSIFICATION OF:			17. LIMITATION OF ABSTRACT	18. NUMBER OF PAGES	19a. NAME OF RESPONSIBLE PERSON
a. REPORT	b. ABSTRACT	c. THIS PAGE			
					19b. TELEPHONE NUMBER *(Include area code)*

Center for Advanced Sensors

Final Technical Report 2006 Funding

Period of Performance 1 June 2006 – 30 November 2007

US Army Contract W911NF-05-2-0019

Dr. Carl Halford, Director

Center for Advanced Sensors

The University of Memphis

Memphis, Tennessee 38152-3180

Submitted February, 2008

1.0 Center for Advanced Sensors

1.1 Administrative

This report covers the activities in the Center for Year Two (FY06). Steven Murrill, the Cooperative Agreement Manager, from the Army Research Laboratory (ARL), Adelphi, MD, met frequently with the Director of the Center to discuss Year Two activities. A no cost extension for Year Two extended the period of performance through 30 November 2007, primarily to accommodate research at Vanderbilt University. Vanderbilt did not receive a subcontract from year three funds. Therefore, they requested extra time to bring their year two efforts to a conclusion.

1.2 Center Activities

The principal researchers at The University of Memphis report their research activities in Sections 2 through 6 of this report. Vanderbilt University researchers report their activities in Section 7 of this report.

The Center for Advanced Sensors continues to support NATO activities in the area of sensor performance modeling for sensors incorporating image processing enhancements. The Director attended the initial meeting of the Exploratory Team for Super resolution and Advanced Signal Processing for EO/IR Sensor Performance (ET51). The Exploratory Team is under the Sensors and Electronics Technology Panel for the Research and Technology Agency for NATO. Current activity is modeling multiband sensor performance with image processing enhancements.

1.2.1 Providing Support to Research Efforts

Center personnel provided support to research efforts at ARL in the area of Intelligence/Surveillance/Reconnaissance (ISR) sensors. This activity continues principally through the research of Drs. Robinson and Perry. Dr. Russomanno's research in sensor networks is also in conjunction with ARL research.

The Army's Night Vision and Electronic Sensors Directorate (NVESD) was supported by frequent contact with Dr. Halford and Robinson. Support was primarily for the Modeling and Simulation Division's research activities.

Dr. Halford continued to support Dr. Tim Edwards (under separate funding) from the Army's Redstone Technical Test Center (RTTC). One of the papers presented at SPIE Orlando reported human perception measurements at the Center. The effort established the relationship between the number of cues and observer performance in identifying combat vehicles.

1.2.2 Perception Laboratory

The Center's Perception Laboratory continues to support military research. NVESD perception experiments throughout the period of performance were conducted at The University of Memphis. Additional experiments are planned for the foreseeable future. The long wave IR imager continues to support Dr. Edward Perry's research. The multispectral MWIR imager has acquired images to support research on filter design by independent component analysis for feature extraction in multi-band images.

2.0   Ontology-Based Sensor Network Environment

This section summarizes the Year Two activities related to an ontology-based sensor network environment supported from FY2006 Center for Advanced Sensors funds. Dr. David Russomanno, along with graduate students Mr. Caleb Goodwin, Mr. Joseph Qualls, and Mr. Andy Lemmon, and undergraduate student Mr. Timothy Henley contributed to Year Two activities. Additional details on the activities can be obtained from the quarterly reports, which include the published and submitted articles during Year Two.

2.1 Milestone One: Develop ontology-based sensor network prototype environment

The primary objective of milestone one is to continue research and development of an ontology-based sensor network prototype environment to investigate the use of Semantic Web infrastructure and service-oriented architecture (SOA) [Singh, 2005] in the deployment of sensors and wireless sensor networks which can be dynamically discovered and tasked.

2.1.1 Activity

1. Monitored the activity surrounding the SensorML initiative [OGC 04-019, 2004] and its applicability to the prototype. Reviewed the revised OGC SensorML specification [OGC 05-086r2, 2006] and its impact on the design of OntoSensor [Russomanno, 2005; Goodwin, 2006]. Determined that OntoSensor will require significant revision of its logical data model to be utilized by those researchers that adopt the SensorML specification.

2. Developed a test interface for the Crossbow MTS310 wireless sensors. The MTS310 has bi-axial accelerometer, bi-axial magnetometer, acoustic, temperature, and photo-sensitive light sensing elements [CrossBow, 2006]. Developed a graphical user interface (GUI) to program and test the MTS310. The GUI facilitates simple programming of the MTS310 sensors, including monitoring transmit/receive communications, as well as setting temperature alarm thresholds given a client identification and other functionality. The purpose of the application is to serve as a first step toward implementing a services-based architecture for a wide-variety of wireless sensors to broaden the prototype's capabilities.

3. Reviewed several research approaches to support semantic service description and matchmaking with registries that use an existing Universal Discovery and Description Interface (UDDI) specification for applicability to the prototype. Approaches reviewed included one proposed by the Naval Research Laboratory (NRL) [Luo, 2005]. Although the NRL effort does not specifically include sensors and sensor services in their research, the NRL activity outlined an approach to bulk-load semantic data into UDDI tModels before queries are issued. TModels provide a mechanism to extend UDDI repositories with external information. We elected to implement a modified approach for the prototype in which the entire sensor ontology is not bulk-loaded into tModels, but rather only that portion of the ontology that was used to satisfy a previous query for sensor

types or capabilities is loaded into tModels. In this approach, when subsequent queries are issued to the prototype concerning sensor capabilities, the tModels serve as a type of cache for satisfying the query.

4. Continued to refine the sensor semantic service description and match approach for the prototype environment. Activity focused on developing an approach to associate a relevant subset of OntoSensor with a UDDI registry of sensor services to enable semantic searching for specifications of sensor capabilities. There is a need to augment the specific facts in the UDDI repository with relevant ontological schema information to more effectively solve subsequent queries to locate sensor services that require semantic matchmaking. C. Goodwin completed his M.S. thesis entitled: "Ontology Integration within a Service-Oriented Architecture for Sensor Networks." His work advanced the prototype environment in the laboratory in that sensor services can be listed in a registry that references a machine-interpretable ontology. The registry conforms to the UDDI specification, but it is augmented with semantic matching via the OntoSensor ontology. Although the approach has several practical limitations, it is illustrative of how Semantic Web and SOA infrastructure can be used in sensor network deployments.

5. Continued to investigate Microsoft Research published efforts related to sensor services [Liu, 2005a; Liu, 2006b; Woo, 2006] for applicability to the prototype. Microsoft Research developed a *Networked Embedded Sensing Toolkit (MSR Sense)* which is "a collection of software tools that allow users to collect, process, archive, and visualize data from a sensor network." It is unclear at this time if MSR Sense fits within the conceptual framework of our work and can be leveraged within our prototype environment.

6. Investigated the concept of semantic streams for interpretation of sensor data [Whitehouse, 2006] using a logic-based framework. The approach may benefit from an ontology such as OntoSensor and a methodology for sensor service descriptions.

7. Evaluated the use of the Altova SemanticWorks product for used with the OntoSensor ontology.

8. Wrote three papers related to Year Two activities of which the first was published, the second was accepted and is currently in press, and the third is in peer review:

C. Goodwin, D.J. Russomanno and J. Qualls (2007) "Survey of Semantic Extensions to UDDI: Implications for Sensor Services," *Proceedings of the 2007 International Conference on Semantic Web and Web Services,* CSREA Press, Las Vegas, Nevada, pp. 16-22.

D.J. Russomanno and J.C. Goodwin (accepted, in press) "OntoSensor: An ontology for sensor network application development, deployment, and management," In G. Aggelou (ed.), *Handbook of Wireless Mesh & Sensor Networking*, McGraw-Hill International, New York, NY.

C. Goodwin and D.J. Russomanno (in peer review) "Ontology Integration within a Service-Oriented Architecture for Expert System Applications using Sensor Networks," *Expert Systems*.

2.2 Milestone Two: Modify/adapt existing sensor ontology to account for target acquisition (TA) sensors as well as Intelligence, Surveillance & Reconnaissance (ISR) sensors

This effort required investigating the use of Semantic Web compliant interfaces for IR cameras, TA and ISR sensors (or their surrogates) to join the prototype sensor network (that is, sensors that plug and play using Semantic Web infrastructure).

2.2.1 Activity

1. Pursued integration of a SONY XCD-SX910 camera within the prototype environment. Students configured an XCD-SX910 camera using National Instruments (NI) Vision Acquisition Software to acquire, display, and save images.

2. Investigated creating a SOA interface for a Sony XCD-SX910 camera. A new API was released for this camera and J. Qualls reviewed the API for possible integration into the ontology-based sensor network prototype environment. Several executables were created with calling conventions to enable invocation of the camera as a Web service.

2.3 References

[CrossBow, 2006] CrossBow Technology Inc., *Wireless Sensor Networks: Product Reference Guide*, 2006.

[Goodwin, 2006] C. Goodwin and D.J. Russomanno, "An Ontology-Based Sensor Network Prototype Environment," *Fifth International Conference on Information Processing in Sensor Networks (Poster),* IEEE, Nashville, TN, pp. 1-2, 2006.

[Liu, 2005a] J. Liu and F. Zhao (2005) "Towards Semantic Services for Sensor-Rich Information Systems," *2nd IEEE/CreateNet International Workshop on Broadband Advanced Sensor Networks*, Boston, MA.

[Liu, 2005b] J. Liu, E. Cheong, and F. Zhao (2005) "Semantics-Based Optimization Across Uncoordinated Tasks in Networked Embedded Systems," *Proceedings of the 5th ACM Conference on Embedded Software*, Jersey City, NJ.

[Luo, 2005] J. Luo, B. Montrose, and M. Kang (2005) "Adding Semantic Support to Existing UDDI Infrastructure," *Report No. NRL/MR/5540--05-8918*, Naval Research Laboratory, Code 5542.

[OGC 04-019, 2004] M. Botts (editor) "Sensor Model Language (SensorML) for In-situ and Remote Sensors," *OGC 04-019*, Open Geospatial Consortium Inc., 2004.

[OGC 05-086r2, 2006] M. Botts (editor) "Sensor Model Language (SensorML) for In-situ and Remote Sensors," *OGC 05-086r2*, Open Geospatial Consortium Inc., 2006.

[Nath, 2006] N. Suman Nath, J. Liu, and F. Zhao, "Challenges in Building a Portal for Sensors World-Wide," *First Workshop on World-Sensor-Web: Mobile Device Centric Sensory Networks and Applications*, 2006.

[Russomanno, 2005] D.J. Russomanno, C. Kothari, C., and O. Thomas, "Building a Sensor Ontology: A Practical Approach Leveraging ISO and OGC Models," *Proceedings of the International Conference on Artificial Intelligence (ICAI 2005)*, Las Vegas, NV, 2005.

[Singh, 2005] Singh, M., and Huhns, M. *Service-Oriented Computing*, West Sussex, UK: John Wiley & Sons, 2005.

[Whitehouse, 2006] K. Whitehouse, F. Zhao, and J. Liu (2006) "Semantic Streams: A Framework for Composable Semantic Interpretation of Sensor Data," *EWSN*, LNCS 3859, pp. 5-20.

[Woo, 2006] A. Woo, S. Seth, T. Olson, J. Liu, and F. Zhao (2006) "A Spreadsheet Approach to Programming and Managing Sensor Networks," *Proceedings of the 5th International Conference on Information Processing in Sensor Networks*, Nashville, TN, pp. 424-431.

3.0 Performance Modeling of Sensors with Image Processing Enhancements (Dr. Carl Halford)

Contacts: Dr. Ronald Driggers, Dr. Gary Wood
Reference ARL BAA Paragraph Reference: 2.6, 2.9

Papers Published:

 S. Chari, C.E. Halford, A.L. Robinson and E.L. Jacobs, "Multispectral infrared image classification using filters derived from independent component analysis," *Optical Engineering,* vol. 46, 116401, 2007.

R.L. Espinola, E.L. Jacobs, C.E. Halford, D.H. Tofsted and R. Vollmerhausen, "Modeling the target acquisition performance of active imaging systems," *Optics Express,* vol. 15, March, 2007.

C.E. Halford, A.L. Robinson, E.L. Jacobs and R.G. Driggers, "Tilted surfaces in SWIR imagery: speckle simulation and a simple contrast model," Optical Engineering, vol. 46, May, 2007.

R. Driggers, J. Reynolds, J. Visgaitis, S, Burks, J. Franck, C. Howell, C. Halford, N. Gat, K. Krapels, "Performance benefits of dual f-number infrared systems," National MSS Symposium, Las Vegas, NV, November, 2007.

V.A. Hodgkin, C.E. Halford and T. Maurer, "The impact of atmospheric path radiance on MWIR and LWIR sensor performance," *SPIE Conference Proceedings*, vol. 6543, April, 2007.

M.A. Brickell, T.C. Edwards, C.E. Halford and K.M. Dennen, "Correlation between human observer performance and the number of spatial, thermal, and total cues in LWIR imagery," *SPIE Conference Proceedings*, vol. 6543, April, 2007.

R.L. Espinola, E.L. Jacobs and C.E. Halford, "Active imaging system performance model for target acquisition," *SPIE Conference Proceedings*, vol. 6543, April, 2007.

S.M. Salem, R.K. Moore, P. Bijl, M.A. Hogervorst and C.E. Halford, "The effects of spatial band-limited noise on human performance for tank identification," *SPIE Conference Proceedings,* vol. 6543, April, 2007.

C.L. Howell, R.K. Moore, S.D. Burks and C.E. Halford, "An evaluation of fusion algorithms using image metrics and human identification performance," *SPIE Conference Proceedings*, vol. 6543, April, 2007.

S. Chari, C.E. Halford and E.L. Jacobs, "Multispectral infrared image classification using filters derived from independent component analysis*," SPIE Conference Proceedings*, vol. 6576, April, 2007.

R.K. Moore, E.L. Jacobs and C.E. Halford, "Cell-balancing for vehicle identification perception experiments and correcting for cell imbalance in test results," *SPIE Conference Proceedings*, vol. 6543, April, 2007.

R.K. Moore, C.E. Halford and C.L. Howell, "Finding a fusion metric that best reflects human observer preference*," SPIE Conference Proceedings*, vol. 6543, April, 2007.

J. Fanning, J. Miller, J. Park, G. Tener, J. Reynolds, P. O'Shea, C.E. Halford and R.G. Driggers, "IR system field performance with superresolution," *SPIE Conference Proceedings,* vol 6543*,* April, 2007.

3.1   Milestone One (2007): Develop Image Quality Metrics for Fused Imagery

Perception tests were conducted using fused visible and MWIR imagery to analyze human performance with identifying the eight target set developed by the Night Vision Electronics and Sensors Directorate (NVESD). We are determining if any of the metrics under investigation show significant correlation with human performance. For modeling purposes, we also wish to know how much improvement in ID performance is yielded by each fusion algorithm for thermal and visible fusion of tank vehicles. An initial analysis of the data from the perception testing has been carried out and the preliminary results are shown below in Figure 1. Examples of the images used in the perception test are given in Appendix B.
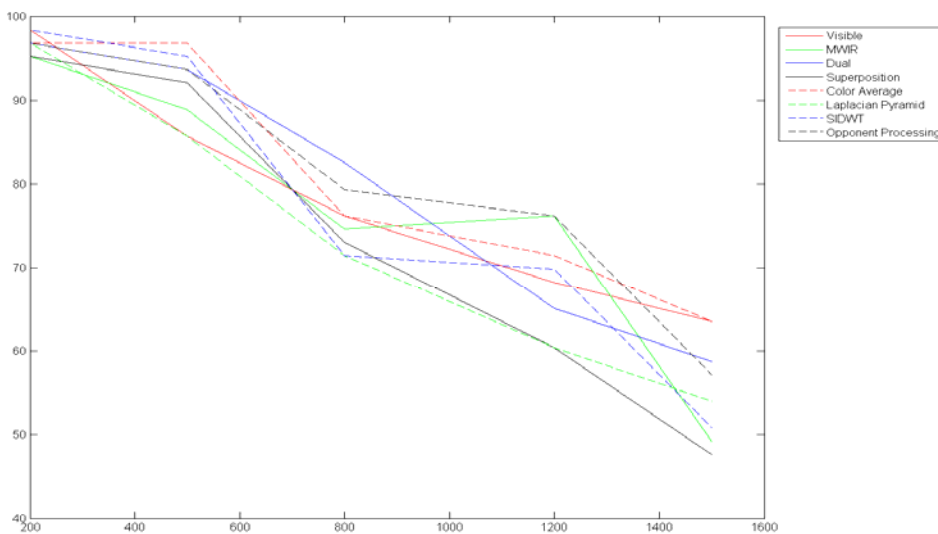

Figure 3.1.1: Initial results from the tank ID perception test.

During the perception test, each observer was shown either an image of both source bands side by side ("brain fusion"), an image of the individual source bands separately, or a fused image using the source bands as inputs. The observers were tasked to correctly identify the tank in the displayed image. The initial results suggest that the best performance is not to be expected by displaying the two source bands side by side as anticipated. Surprisingly, color averaging and the opponent processing fusion processes outperformed the "brain fusion" technique. This is in direct opposition to our original hypothesis that "brain fusion" would offer the best possible performance. Further testing is needed to investigate this matter. The current test results conflict with our previous fusion tank ID pilot experiment. Neither of these pilot experiments had enough observers to yield curves with non-overlapping error bars.

The above result supports that a gain in performance can be realized by using fusion. Ideally, a good fusion process should offer more salient information in the fused image compared to any of the source images alone. For example, Figure 2 shows a case where fusion helps with the identification of a vehicle. False coloring is used to assist with identifying those signatures specific to each spectral band.

Figure 3.1.2.1: Rear aspect; Top left: Visible band. Top right: MWIR band. Bottom: Fused
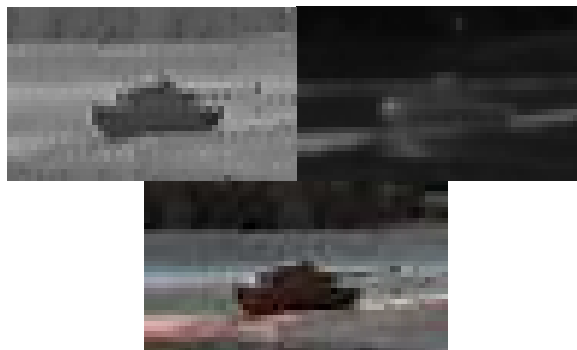

Figure 3.1.2.2: Side aspect; Top left: Visible band. Top right: MWIR band. Bottom: Fused

The top left images in Figure 3.1.2a & 3.1.2b are rear aspects of the visible images and the top right are side aspects of the MWIR images. The bottom images in each group are the fused images. Referring to Figure 2a, the MWIR image shows a clear identifiable thermal signature while no signature stands out in the visible image. In Figure 2b, the opposite is true. The side aspect allows for easy identifiable traits to be seen in the visible image but the MWIR image signatures can not readily be associated with any one particular target. By looking at the respective fused images, it is seen that the salient information from each band is included in the fused image and using the fused image alone gives a better indication of the type of target in the image than using one band independently.

The results offered in this report are preliminary results and more observers are scheduled to take the perception test August 20-24, 2007. We feel that the increase in observers will allow us to determine if any learning effects are affecting the results of the tests or if there is new information in the fused image uncommon to either of the individual source bands.

3.1.1 Fusion introduction

Images of different spectral bands can be combined in various ways to produce single images containing information from all of the source bands. Many image fusion algorithms have been devised and are found in open literature. At best, image fusion can produce better observer task performance than is possible using either of the source imagery bands. At worst, fused imagery can yield observer performance that is significantly lower than performance achieved using the source imagery. Fusion algorithms seem to differ in the degrees to which they successfully handle source imagery with noise, mis-registration, differing spatial resolution, and opposing contrast. The algorithms also have widely varying memory requirements and computational complexity. In an attempt to understand how several different image fusion algorithms affect the ability of observers to perform visual tasks, several perception tests were devised and performed at the Center for Advanced Sensors at the University of Memphis.

3.1.2 Fusion preference paired comparison

First, a paired comparison test was performed to see if observers prefer images from a particular fusion algorithm over the source bands or other fused images. An attempt was also made to find a fusion quality metric that reflects the perceived quality level of fused imagery. None of the fusion quality metrics that we investigated exhibited such a correlation with observer preference. The results were presented in the 2006 SPIE Defense and Security Symposium.

3.1.2.1 Results

Perception tests have been conducted to compare the fusion metrics [1] to human observer preference. Five observers participated in two alternative forced choice (2AFC) experiments. Observers were asked to indicate for pairs of images which image had higher quality. There were two perception experiments administered, one with the 'Lights' images and the other with the 'Bus' images. The preference results of the observers were calculated and plots of their perceived image quality are given below.
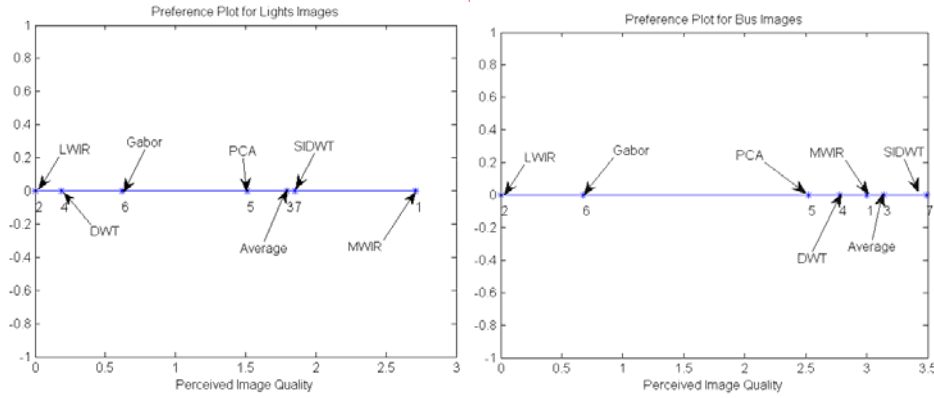
Figure 3-1.   Preference Plots

In both cases, the Gabor-fused images faired poorly. The fusion technique that we chose with Gabor filters introduced a noticeable blur that detracted from the perceived image quality. Pixel averaging, PCA averaging, and the SIDWT all yielded consistently high preferences in both the 'Bus' and 'Lights' image sets. The relative preference of the DWT-fused images changed drastically from the 'Lights' images to the 'Bus' images. This may be because the DWT-fused 'Lights' image exhibited obvious distortion artifacts due to fusion, while the DWT-fused 'Bus' image did not. This dropped the preference for the DWT in the 'Lights' images, while allowing the DWT to still perform well in the 'Bus' imagery test. This change in preference due to fusion-introduced distortion proved important in determining which fusion metric best represents observer preference.

It was also noted that in the 'Lights' test, the MWIR image was more preferred than any of the fused imagery. Upon reviewing the LWIR and MWIR images, it was noted that more information appears to be present in the MWIR image than in the LWIR image of the 'Lights' scene. Furthermore, the LWIR 'Lights' image does not seem to contain any information that is not also present in the MWIR image, so the 'Lights' images were not an ideal image set for a image fusion. A more appropriate image set would yield fused images that would be more preferred than either of the input images. This brings up an interesting issue in image fusion: when is fusion likely to be beneficial? When multiple spectral bands are available, one band may present a clear advantage over any other. In such a case, fusion will not be ideal. In other cases, two or more bands may contain unique information that could potentially be fused into a single image. It is likely, though, that an observer using a multi-spectral sensor will not know which of the available bands is most useful at an instant and may also rely on a fusion algorithm to 'sift through' the available bands for all available information, even if it is all to be found in a single band. Here, the fusion algorithm needs to be transparent enough to not introduce perceived degradation to the imagery. So, the case of image fusion with only one useful band is still worth investigation, since it may occur in practice.

12

The preference results were correlated with the fusion quality metrics listed in [1] to determine which fusion metric best correlates with the observers' preference. The correlation coefficients for the 'Lights' and 'Bus' images are listed in the following table.

Table 3.   **Correlation coefficients relating the fusion metrics to the observer preferences**

	FQI	WFQI	EDFQI	MINF	MS(F-L)	MS(F-M)
Correlation to preference for 'Lights'	0.3604	0.1476	-0.0374	0.7193	0.3207	0.3810
Correlation to preference for 'Bus'	0.6950	0.9825	0.9488	0.8231	-0.2967	0.5969

Both of the Mannos-Sakrison filter metrics yielded results that correlated poorly with observer preference. The FQI also did not perform particularly well when correlated with the measured observer performances for the 'Lights' or 'Bus' images. While none of the metrics performed especially well for the 'Lights' images, the mutual information metric correlated best with the observers' preference. The Mutual Information measure also correlated best overall when both the 'Lights' and 'Bus' results are considered. Both the WFQI and the EDFQI correlated extremely well with the 'Bus' preferences, but both also correlated quite poorly with the 'Lights' preferences. This may be because of the fusion distortion present in the DWT-fused 'Lights' image. Both of these metrics rated the DWT images highly for both the 'Bus' and 'Lights' images. Neither was able to tell, though, that distortion was present in the DWT-fused 'Lights' image that would cause its perceived quality to drop considerably.

The following scatter plots compare the different fusion metrics with the measured perceived image quality of the fused images. The correlation, or lack thereof, can be seen for each fusion metric.
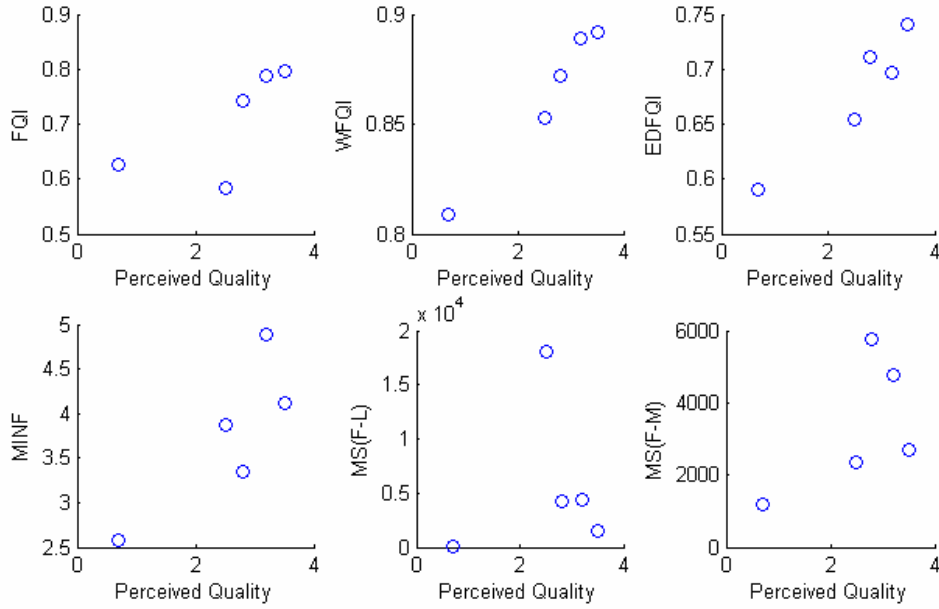
Figure 3-2. Scatter plots of the metrics and the measured preferences for the 'Bus' images.

It was noted previously in the 'Bus' images that the WFQI and EDFQI both demonstrated good correlation with the observer's preference. This is also apparent in the scatter plots. Both the WFQI and the EDFQI show strong linear correlations with the perceived image quality. The mutual information plot also shows some correlation to the perceived image quality. In Figure 5, the scatter plots are shown for the 'Lights' images. Visually, the correlations are quite poor for almost all of the metrics. The mutual information still exhibits some correlation to the perceived image quality, as was shown in the correlation coefficients of Table 3. Of the fusion metrics tested here, mutual information was found to be the best indicator of perceived image quality for MWIR/LWIR fused images. Among the fusion methods used in the paired comparison test, the SIDWT was consistently preferred above all other fusion methods. It is to be noted that the Pixel-averaged images also yielded a consistently high perceived image quality with a very small processing time.
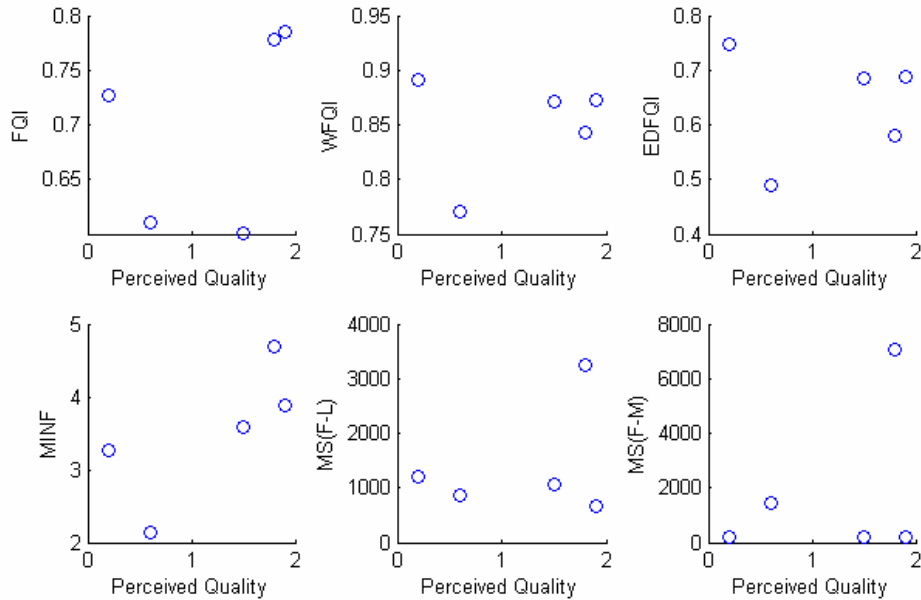
14

Figure 3-3. **Scatter plots of the metrics and the measured preferences for the 'Lights' images**

3.1.2.2 Fusion preference conclusions

While the mutual information most consistently correlated with the measured observer preferences, none of the fusion metrics tested here seemed to measure fused image quality in a way similar to the human observers. It is noted that observers consistently deemed the pixel-averaged and SIDWT fused images to be of high quality relative to the other images in the set. Future work will include task performance based perception experiments to find an image metric that correlates well to an observer's ability to perform a visual task. Knowing an image fusion metric that relates well to observer performance will help NVESD to model the effects of image fusion on target acquisition.

3.1.3 Number identification performance with fused imagery

A second perception test was run to determine if an improvement in performance due to fusion of source imagery could be measured. Two synthetic source bands were created by splitting up images of numbers. The source band were then fused several different ways and presented to observers for identification in a perception experiment. A significant improvement in observer performance was measured for several of the test fusion algorithms.

For image fusion to be useful, each source band must contain some information not present in the other band. Also, some of this unique information must be useful to the observer who is performing some assigned task. If these conditions are not met, fusion will not increase the observer's ability to perform his task. The task to be measured in

15

this test was number identification. Portions of number images in two source band images were fused together using several techniques before being presented to the observers for identification.

The five fusion methods tested were a discrete wavelet transform method, pixel averaging, a Gabor filtering method, a principle component analysis method, and a shift-invariant wavelet transform method. Most of the methods break down the source images with some set of basis functions and then compare coefficients to determine information content in each band of each source image. This information is then used to pick layers for the construction of the fused image. Observers were asked to identify images of numbers 0 through 9 in a 10 alternative forced-choice experiment. The source band images containing the incomplete images of the numbers were also displayed to the test subjects for identification. Six different font sizes were tested to allow performance curves to be generated for each fusion method. The numbers displayed were selected at random according to a uniform probability density function.

In the analysis, the mean probability of identification as a function of font size will be plotted to see which fusion method yielded the best observer performance on average. Confidence intervals will be used to help determine if the measured differences are significant or not. An investigation will be made into the nature of the incorrect responses from the observers as well. If an observer cannot correctly perform the task, will their incorrect answers be spread uniformly from 0 to 9? Or will their answers be clustered around visibly similar numbers, indicating that some useful information was presented to the observer?

3.1.3.1 Image Preparation

MATLAB was used to generate eye chart images of numbers at six different font sizes. The numbers were white on a gray background (127 grayscale value on an 8-bit scale). The clean number images were split into two source band images randomly using the process shown below:
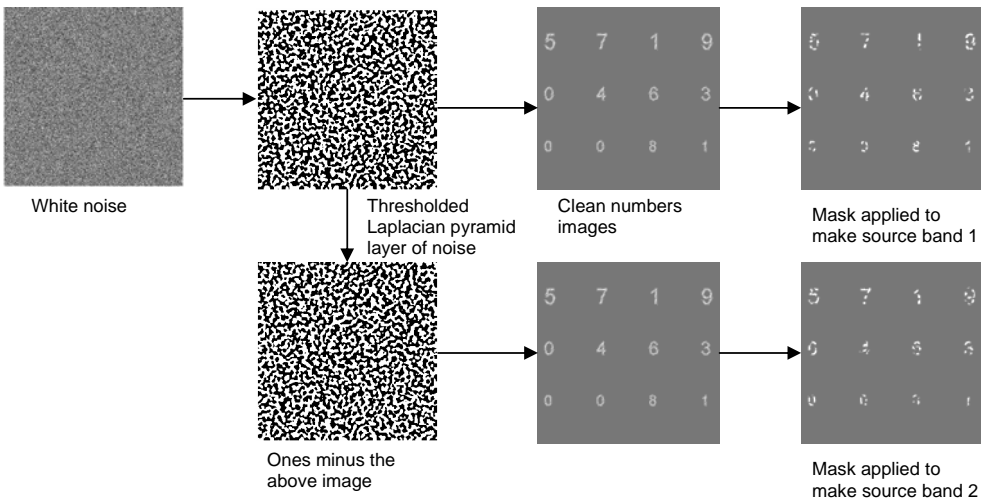
**Figure 3-4, Image processing to generate two source bands to fuse**

White noise was effectively band pass filtered by using a single layer of its Laplacian pyramid decomposition. A threshold was then applied to the resulting correlated noise to make an extraction mask to apply to the image of numbers. A complimentary mask was then generated by subtracting the first mask from a matrix of zeros. The center frequency of the noise was chosen to make identification difficult with a single source band image. Noise with higher or lower frequency content allows the number images to be more easily identified. The source bands generated by the noise mask process were then used as inputs to the image fusion algorithms. Examples of the stimulus images presented to the test subjects are shown below:

Source band 1   Source band 2
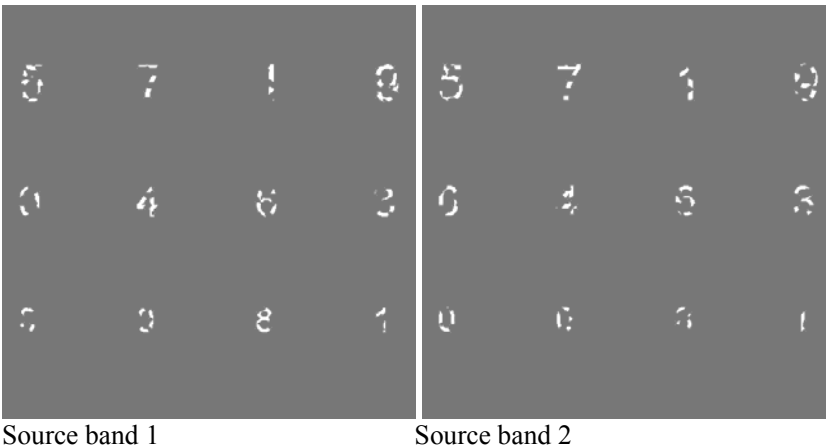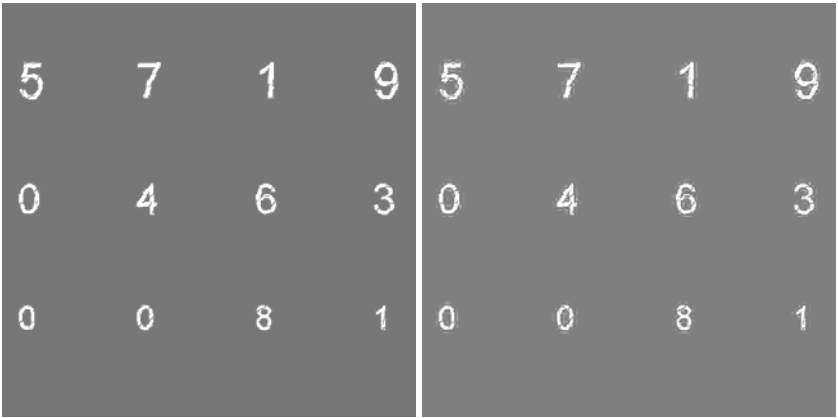
Averaged

DWT
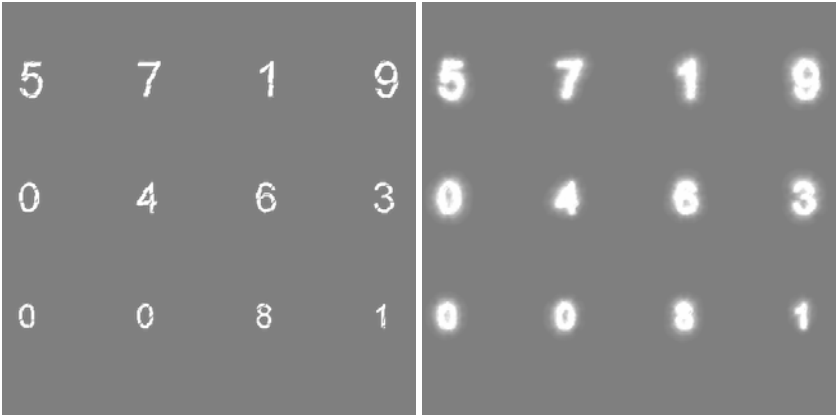
SIDWT

Gabor

PCA

Figure 3-5, Fused stimulus images used in the perception test

3.1.3.2 Analysis of Results

Ten observers participated in the fusion number identification perception experiment. Each observer was shown 40 instances of each image type (5 fusion methods plus 2 source bands) at each of the 6 font sizes. This resulted in a stimulus set of 1680 number images (6x7x40) that were presented to each observer. The mean probabilities of identification are plotted against the font size in figure 3-3.
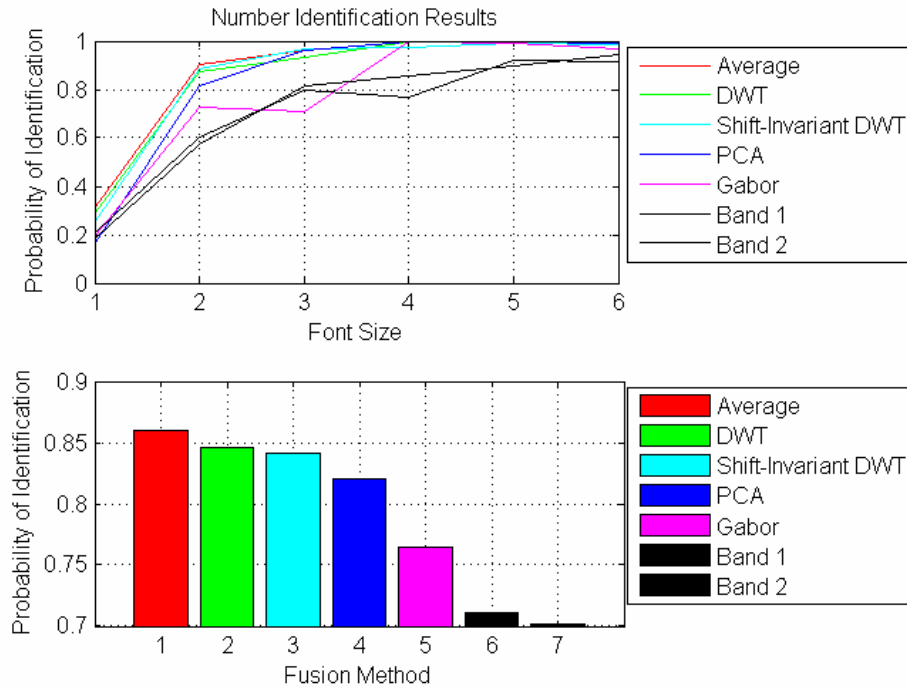

Figure 3-6, Probability of ID versus font size and probability averaged over all font sizes

The second graph shows the probability of identification for each method averaged over the six font sizes. Looking at the graphs, it is clear that fusion was beneficial in this case. Every fusion technique yielded better average performance than either of the source bands alone. It can be seen that the differences in performance on the pixel-averaged, DWT, and shift-invariant DWT images are very small. These three techniques all seem to out perform both the PCA and Gabor methods, but the precision of the test must be quantified to ensure that this measured difference is meaningful. The results in the bar graph seem to agree well with the previously measured observer preferences. In general, the fusion techniques that were more preferred by the observers also yielded better task performance in the number identification test. Figure 3-4 shows a plot of the previously measured preferences.
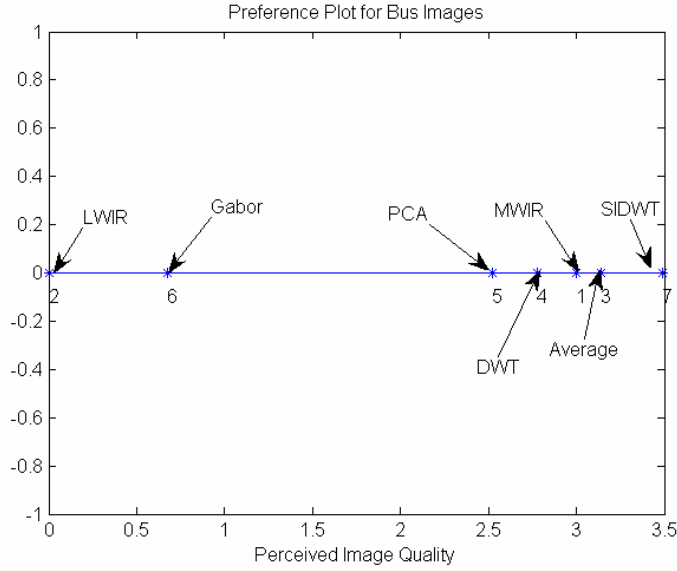
Figure 3-7, Preferences measured from a previous paired comparison test

Because the identification test results correlate well with the results of the paired comparison test, it is expected that the mutual information metric, the weighted FQI, and the edge-dependent FQI will give measurements that correlate well with the ID test results. This means that they may be useful in modeling the effects of image fusion on observer task performance.

The confidence interval helps to indicate the precision of empirical data. Below are the formulas to find the mean, variance, and confidence interval of a set of data:

$$\bar{x} = \frac{1}{n}\sum x_i$$

$$\sigma^2 = \frac{1}{n}\sum_{i=1}^{n}(x_i - \bar{x})^2$$

$$\bar{x} \pm erf^{-1}\left(\frac{ConfLvl}{2}\right)\left(\frac{\sigma}{\sqrt{n}}\right)$$

In these equations, x bar is the mean, n is the population size, x_i is a single measurement, *ConfLvl* is the desired confidence level, and σ^2 is the variance. The 95% confidence intervals were found for this set of data. The graph of identification versus font size with the confidence bars is shown next:
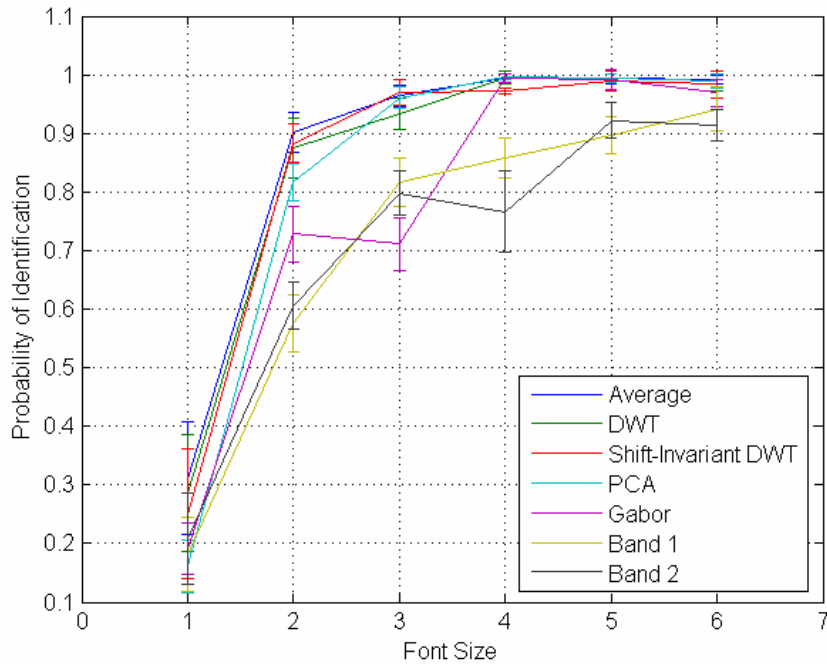
Figure 3-8, Probability of ID versus font size with 95% confidence intervals

The graph shows that this test did not measure a significant difference in performance amongst the pixel averaging, DWT, and shift-invariant DWT techniques. The confidence intervals for these three methods have a large overlap at almost every font size. The PCA and Gabor confidence bars also overlap the other techniques at font sizes 4, 5, and 6. It can be seen, though, that as the font sizes decreased and the task became more difficult that the performance yielded by the PCA and Gabor techniques generated confidence bars that no longer overlapped the bars of the other three techniques.

The probabilities of identification in this experiment give some indication of how much information was present for each combination of fusion methods and font sizes. Another question remains: if an observer does not correctly identify the stimulus, does this mean that no information was available to them or simply that not enough information was available? The response probability density functions may give us some indication of this. If no information is available from the stimulus, we would expect the guesses from the observers to either have a uniform pdf or some pdf that does not depend on the stimulus presented. The confusability matrices below use grayscale values to indicate the measured probability of an observer response in a column when presented with a stimulus in a row. It is noted that for an easy font size that the observers correctly identify the stimuli with very few errors. When the numbers are presented at the medium font size, some stimuli become confusable. Looking along row 6 shows that observers were likely to respond that the presented 6 was a 5, 8, or 3. The pdf indicated along row seven is very different, though. Some observers may have confused the 7 with a 2 or 4,

21

but there were no 5, 8, or 3 responses when a 7 was displayed at the medium font size. It seems that the response pdfs depend on the stimulus even if an incorrect response is made.
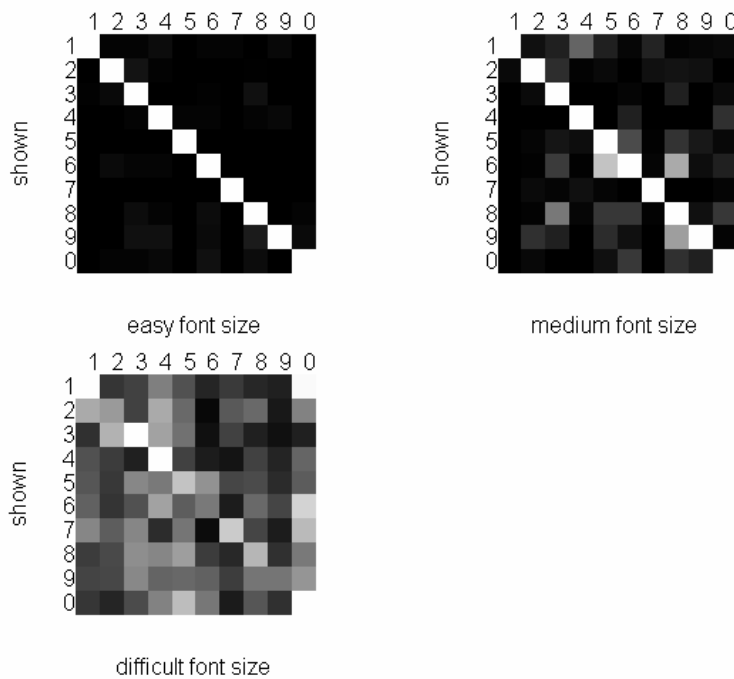

Figure 3-9, Confusability matrices for different font sizes

When sufficient information is present, identification can occur in almost all trials. As information is removed, peaks begin to form at incorrect positions of the response pdf at the locations of confusable stimuli. In effect, the observers can no longer discriminate all of the stimuli, but they can discriminate between sets of confusable stimuli. As even more information is removed these sets of confusable stimuli increase in size and decrease in number until pure guessing takes place amongst all of the stimuli. The difficult font size shows that case in which very little information was available to the observers. The guessing was much more uniform than in the medium font case, resulting in a mostly gray confusability matrix.

The next graph shows the probability distribution functions for responses to the displayed number 6 for each of the six font sizes. It can be seen that as the font size decreases that 8 quickly becomes confusable with 6. As the font becomes smaller, 3 and 0 also become significant confusers.
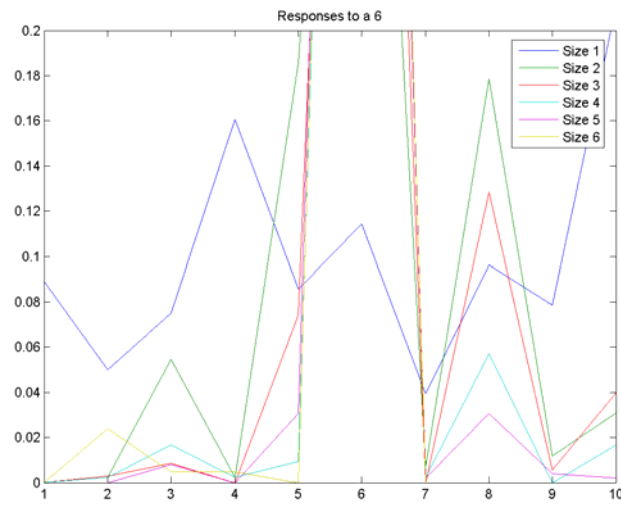
Figure 3-10, Observer response probability density functions for the displayed number 6 at different font sizes

The following chart shows conceptually how the observer's task changes as information is removed and they are forced to guess amongst sets of confusable stimuli. It should be noted that the confusabilities displayed in these results are specific to the font used and the group of fusion techniques. Using different fonts or a different means of information removal will result in different measured confusabilities.

Figure 3-11, Representation of confusability layers observed in the number identification perception test

3.1.3.3 Fusion Identification Conclusions

All of the fusion techniques tested here improved number identification performance for the noise-split source bands. The PCA and Gabor fusion techniques yielded less observer performance improvement than the DWT, pixel-averaging, or shift-invariant DWT methods. Image fusion is still not sufficientl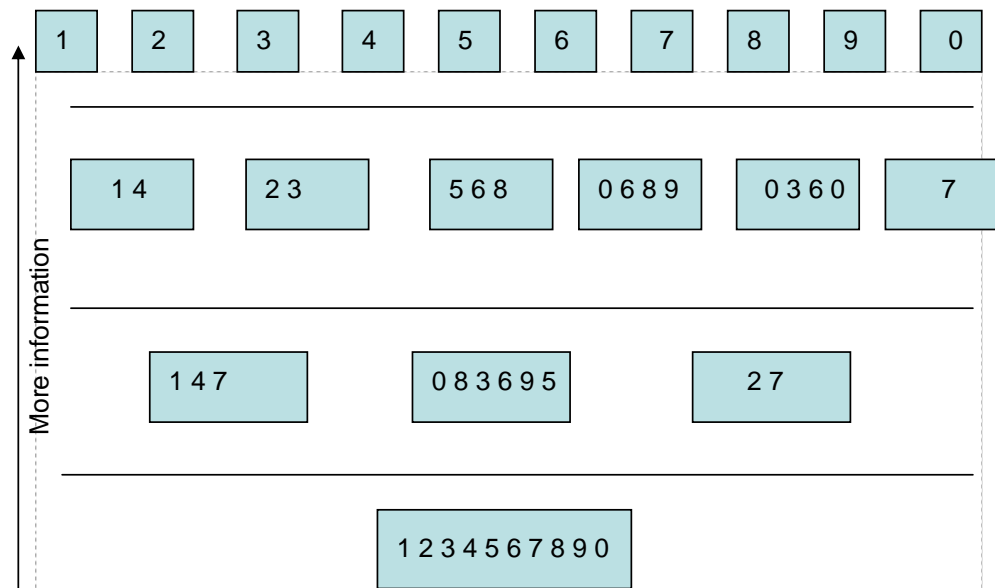y modeled for use in sensor performance prediction. A general fusion model is desirable because there are many fusion techniques and new ones are constantly developed. If the source sensors are well characterized, V_{fused} can be found for some fusion methods by finding the effective *MTF* of the system and the contrast, C_t, of the fused image. The V_{50} for the fused image set may be less than the V_{50} terms for the source bands if complimentary information is present in the two bands. The more unique and useful information present in each band, the more observer performance can be expected to improve. Quantifying the amount of unique information in source bands and its relationship to the change in task difficulty remains to be determined. Understanding this relationship will make modeling of fusion for target acquisition modeling possible.

3.1.4 Standard image fusion test set suggestions

In fulfillment of a request from NATO, a document was prepared describing characteristics of a source imagery test set for image fusion algorithms. It is meant to aid researchers developing fusion algorithms or developers selecting amongst fusion algorithms for an application.

A great number of image fusion algorithms are now available to combine data from two or more images into a single fused image. When image fusion is successful, it can provide a single image that is more informative to an observer or machine than the source images. Also, it may give context to data in different spectral bands that is not readily detected by viewing the source images individually. When image fusion is not successful, it may yield an output image of significantly lower utility than the source images.

How, then, can one be assured that useful image fusion will take place? Different fusion algorithms divide and compare the data to be fused in very different ways. Some algorithms sacrifice contrast to increase edge visibility or vice versa. Some algorithms use false coloring to associate information in the fused image with one of the source band images. Other fusion techniques are more lossy in the sense that source band association cannot be easily made by viewing the fused image. Different fusion methods amplify or attenuate noise. The effects of mis-registration vary with the fusion algorithm as well. The fusion algorithm most likely to produce useful results will depend on the application and the quality of the source imagery. This document will outline some characteristics that should be present in an image fusion test set for combining data from electro-optical sensors.

3.1.4.1 Characteristics to be tested:

A standard image set for evaluating image fusion algorithms should contain examples of each of the following cases. If perception testing is not a concern, it may be that such an image set can be drawn from imagery that has already been collected. A new data

collection would probably be necessary to obtain an image set that both contains the characteristics outlined here, and is suitable for task-based perception testing.

3.1.4.1.1 Opposing contrast in source bands

An image fusion algorithm should be able to handle bands with opposing contrast. Visible and infrared images of the same objects can often have opposing contrast. Some algorithms, such as pixel-by-pixel averaging, can produce output images with much lower target to background contrast than the source images. Figure one shows visible and MWIR images of a military vehicle. Each image shows strong contrast, but the pixel-averaged image shows very low contrast. The final image is fused using an opponent processing technique, and it retains good contrast.
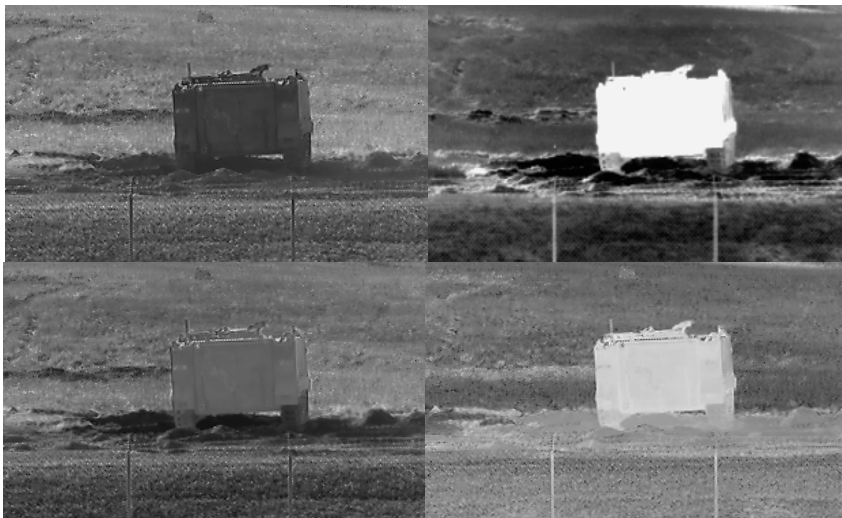
Figure 3-12, clockwise from top left: visible, MWIR, opponent processed, pixel-averaged

3.1.4.1.2 Similar source bands

Another case that must be handled gracefully by a successful fusion algorithm is very similar source bands. It is often detrimental for a fusion algorithm to remove or attenuate information that is readily available in both of the source bands. Example MWIR and LWIR images are shown in figure two. The opponent processing that worked so well for opposing contrast images eliminates much of the signal when similar source bands are combined. On the bottom and to the right is shown the discrete wavelet transform fused image, which contains much of the redundant and unique information from each source band.

Figure 3-13, clockwise from top left: MWIR, LWIR, opponent fused, DWT fused to scale 4

3.1.4.1.3 Strong Content in one band, not present in the other

Similar and opposing contrast have been addressed in the sections above, but the ability to combine unique information from two source images is what makes image fusion useful. Signatures present in only one of the source bands should also be present and not attenuated in the fused image. The top of figure 3 shows visible and MWIR images of a tank. Clearly present in the visible image, but not seen in the MWIR image, is a solar reflection from the gun barrel. In the MWIR, a hot spot is seen on the front of the hull, which is not indicated in the visible image. The shift-invariant discrete wavelet fused image clearly contains both of these signatures. The opponent processed image beside it also contains these signatures, but at considerably lower contrast.
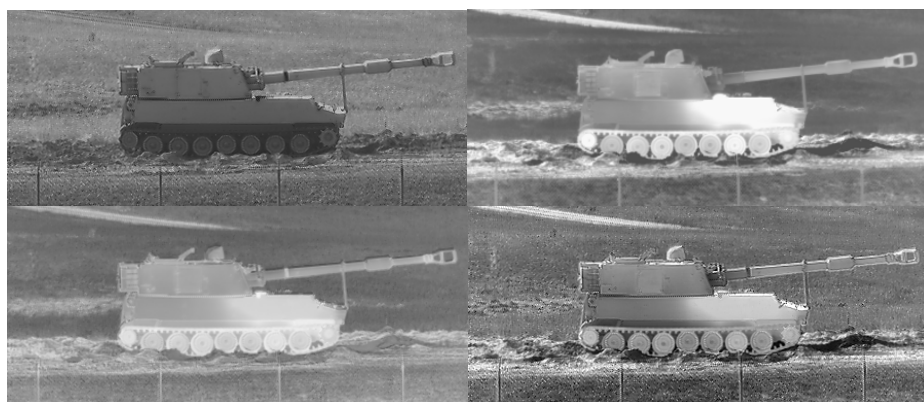

Figure 3-14, clockwise from top left: visible image, MWIR image, shift-invariant DWT fused image, opponent processing fused image

26

3.1.4.1.4. Noise in one source band

When collecting and fusing data from two sensors, it will often be the case that imagery from one sensor has a higher level of quality than imagery from the other sensor. This may be because the present imaging conditions produce more signal in one band than in the other. Also, it may be because one sensor is inherently better than the other. Whatever the case, it is possible that one or both source bands may contain noise. Spatial frequency band comparing algorithms (Laplacian pyramid, Gabor, DWT, shift-invariant DWT, etc) will tend to amplify this noise. This can result in a fused image that is less useful than the better of the two source band images. Figure 4 shows a very noisy I^2 image along with a relatively clean LWIR image. The resulting Laplacian pyramid fused image is also very noisy. The multi-scale fused image at the bottom right combines information from both of the source images while retaining less of the noise from the I^2 band.
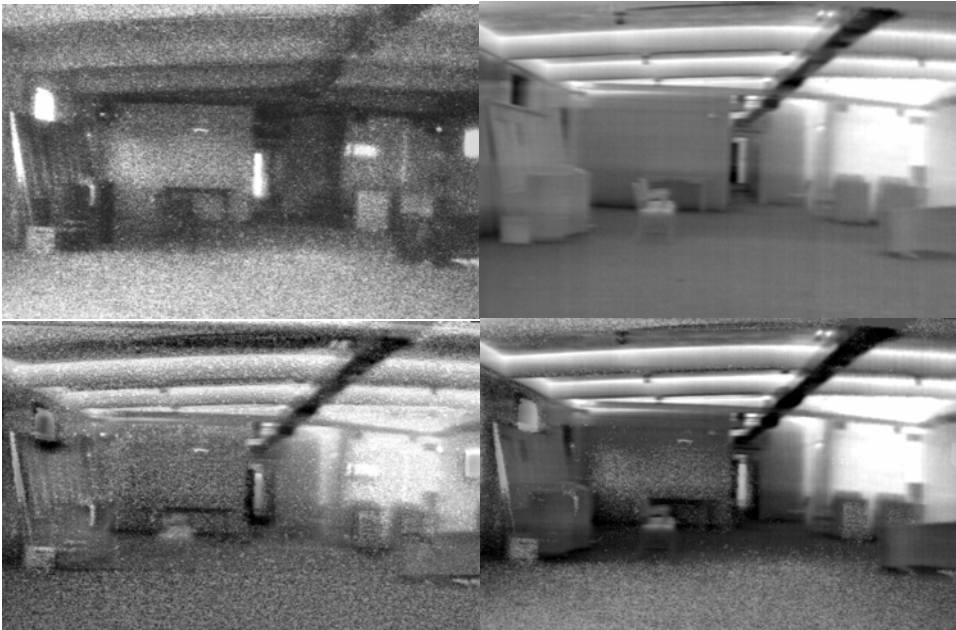
Figure 3-15, clockwise from top left: I^2 image, LWIR image, multi-scale fused image, Laplacian pyramid fused image

3.1.4.1.5 Mis-registration handling

Image registration is a significant issue in image fusion. It is ideal to design the system so that both sensors share an optical axis, have similar optics, similar detector resolution, and collect imagery simultaneously. This is often infeasible, and imagers are instead placed close to each other with somewhat similar fields of view. This introduces registration and parallax errors. In many image fusion applications, the fusion algorithm will regularly need to handle images that are somewhat mis-registered. In figure 5, two images of squares were mis-registered with each other by 2 columns and rows. They

27

were then fused. The DWT fused image on the left of figure 5 shows stronger double-edging due to mis-registration than the multiscale fused image on the right.
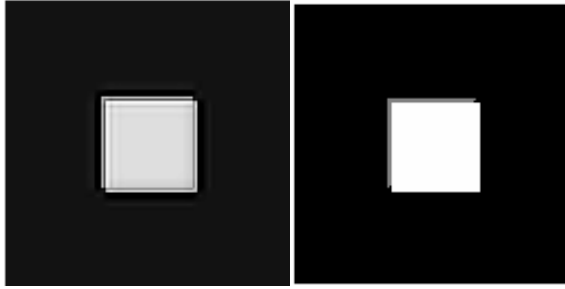
Figure 3-16, scale 2 DWT fusion on the left, multiscale fusion on the right

3.1.4.1.6 Differing spatial resolution

Images to be combined will often have different spatial resolution. Prior to fusion, the smaller of the images must be up-sampled and low-pass filtered. The result is two source band images that may have significantly different spatial frequency cutoffs. For this case, successful fusion will use the high frequency edges from the higher resolution band, but will incorporate information from both bands at the lower spatial frequencies. The opponent processing fused image in figure 6 has attenuated some of the detail easily seen in the visible source image. Also, strong signature from the hot tank tracks see in the MWIR image are not well represented. In the multiscale fused image, both the hot tank tracks form the MWIR and the fine details from the visible image are seen.

Figure 3-17, clockwise from top left: visible image, MWIR image up-sampled 10x using bicubic interpolation, multiscale fused image, opponent processing fused image

3.1.4.2 Thoughts on using a standard image fusion test set

The fused imagery produced using this source set can then be evaluated using criteria appropriate for the application. For some applications fusion quality or image quality metrics may yield sufficient information. For imagery to be presented to human observers it may be necessary to perform a perception test using the standard imagery. It also may be known for a given application that some of the above cases will not be encountered. As new fusion algorithms are developed, their strengths and weaknesses should be found by quantifying their performance on an image set containing the cases described here. It may be deemed appropriate in the future to add other important source band cases to this list as well.

3.2 Milestone Two (2007): Modify/adapt existing sensor models to account for image processing enhancements in ISR sensors.

3.2.1 Classification of multispectral images using filters derived from Independent Component Analysis

In this research we implemented an Independent Component Analysis (ICA) based data-dependent filter for multispectral texture feature extraction and applied a unique method to fuse the extracted features. Combined space spectral filters were derived from ICA basis functions of multispectral MWIR images which were acquired in a field data collection. These filters were used to extract features from multispectral MWIR images. The space spectral features were fused based on the phase relationship among basis functions of the corresponding bands. The classification performance of these filters was shown to be superior to those derived from multispectral Principal Component Analysis (PCA) basis functions and opponent plus unichrome Gabor filtering. With no-added noise in test images, the performances of the ICA-based filters, PCA-based filters, and opponent, plus unichrome Gabor techniques were similar. However the ICA-based filters reached their highest classification rate with fewer features than PCA and Gabor filters. With noisy test images, the ICA-based filters performed better than opponent, plus unichrome Gabor and multispectral PCA-based filters. Therefore, it was a demonstrated that the performance of ICA based filters is better in terms of having higher classification rates and also needing fewer features for attaining those classification rates. For higher SNR values, the performance of multispectral PCA was better than opponent, plus unichrome Gabor, but with reduced SNR opponent, plus unichrome Gabor overtook multispectral PCA in performance. The superior performance of our approach can be attributed to the following two strategies used: (1) Combined space spectral ICA based filters for multispectral feature extraction (2) feature fusion technique controlled by the phase relations among ICA basis functions which captures the statistical decorrelation process. ICA based filters provide a good balance between two popular approaches to filter design for feature extraction: one which use filters with good joint spatial and frequency resolution and the other which picks filters parameters based on the data. For our data set, the ICA basis functions not only had joint spatial and frequency resolution

29

properties similar to (not the same as) Gabor filters, they also showed slightly more complex (richer) frequency responses that were learned from the data itself. On the other hand, the PCA basis functions were also data-dependent with rich frequency responses, but they did not show good joint spatial and frequency resolution.

The research under this milestone has also been accepted for publication in the Optical Engineering Journal

3.2.2 Survey of denoising techniques for image enhancement

This section discusses denoising techniques for image enhancement available in open literature. The algorithms described can be used to process images obtained from Intelligence Surveillance Reconnaissance (ISR) imaging systems. The report provides a general overview with out attempting to address problems related specifically to ISR imagery. Interfering natural phenomena, imaging and data acquisition instruments can contribute to noise in the image displayed to the end user. The presence of noise in images can hinder the image understanding capabilities of the end user, be it humans or some form of artificial intelligence. Hence denoising of images is a very important image enhancement tool. Denoising techniques can be broadly classified in two main categories: the spatial domain denoising and transform domain denoising.

Spatial filters act as smoothing operators on the image. The noise which shows rapid spatial variations can hence be eliminated. Spatial filters can be categorized as linear and non-linear filters. Linear filters like mean filters calculate the replaces each pixel by the mean of its neighborhood, while non-linear filters such as median filters replace each pixel by the median of its neighborhood. Wiener filters are linear filters which can estimate the original signal in the presence of additive noise. Wiener filters require that the spectral characters of the original signal and the noise or their autocorrelation and the cross correlation. Wiener filter estimate of the original signal minimizes the mean square error between the original signal and the estimate.

Domain transformation involves representing an image (or any signal) as a linear or non-linear combination of basis functions. The new representation can provide insights into the characteristics of both the actual signal and noise depending on the properties of the basis functions used. Basis functions can either be data dependent (learned from the data) or can be fixed (predetermined or data independent). Data dependent transformations involve identifying both the coefficients as well as basis functions. Data dependent transformations such as Independent Component Analysis (ICA) and Principal Component Analysis (PCA) focus on finding basis functions and coefficients so as to maximize the sparseness of the representation. The sparseness is achieved by applying statistical constraints in the transform domain (independence for transformed variables in ICA and decorrelation of transformed variables in PCA). Sparse representations suggest that the actual (noise free) signal can be represented by a smaller number of basis functions than the measured signal, and the bases that can be ignored are very like the noise components. For example in PCA the eigenvectors of the data covariance matrix are the basis functions. The data is first represented in the PCA domain. During the inverse transformation process (from PCA domain back to spatial domain), eigenvectors

30

(basis functions) corresponding to small eigenvalues are not used. Thus spatial image is now reconstructed without the noise components. The one drawback of such data dependent denoising techniques is that they are computationally expensive.

When a predetermined set of basis functions is used, the transform calculates the coefficients need to scale those basis functions. The denoising capability of these transforms is strongly dependent upon the sparseness of their representation of a signal. When it is known that a transform provides sparse representation, it can be inferred that only a few of the basis functions represent the actual signal. This means that for the actual signal representation only a small number of transform coefficients are non-zero. This sparseness of the wavelet bases is what makes wavelet transform so effective in denoising. Wavelet decomposition provides a joint spatial-spatial frequency representation. The spatial frequency part of the representation is made in terms of the variable referred to as scale which is the inverse of the spatial frequency. Thresholding of wavelet coefficients to suppress certain basis functions is a common technique in wavelet denoising and is referred to as wavelet shrinkage. Hard thresholding involves setting coefficients with values less than the selected threshold to be equal to zero and leaving the large coefficients intact. In soft thresholding, the coefficients less than the threshold are set to zero. The coefficients higher than the threshold are forced towards zero with values determined by $xf(x)$, where $x =$ (coefficient – threshold) and $f(.)$ is a function for creating the required mapping. The identification of an appropriate threshold value can affect the performance of the denoising process. The Stein's unbiased risk estimator (SUREshrink) and the VISUshrink (provides best performance in terms of Mean Square Error when the data points reaches infinity) are two popular threshold selection techniques. Denoising of images can also be accomplished by using an optimal wavelet tree representation which relates to ordering of terms in the wavelet expansion. In this technique the wavelet decomposition is represented as a tree with each level representing the scale and each node representing a coefficient. A large value child coefficient (node) can be assumed to be a noise if its parent nodes are not well pronounced. Some techniques also use statistical properties of coefficients such as their probability distributions and their inter-scale and intra-scale correlations to separate signal coefficients from noise coefficients.

3.2.3 Conclusions:

This report is a survey of denoising techniques for image enhancements. In most cases, the end user of ISR images are humans involved in tactical discrimination tasks. The problem with identifying a suitable denoising technique for ISR sensors is unavailability of human image perception evaluation of the denoising techniques (specifically for ISR imagery). Hence future research should focus on human psychovisual studies to compare various denoising algorithms in terms of detection, recognition and identification performance for ISR imagery.

3.2.4 References:

M. Motwani, M. Gadiya, R. Motwani, and F. Harris, "A Survey of Image Denoising Techniques," in *Proceedings of GSPx 2004,* September 27-30, 2004, Santa Clara Convention Center, Santa Clara, CA.

D. Langrebe, *Signal theory in multisensor remote sensing*, Wiley Interscience, 2003

4.0　Milestone - Performance Modeling of Advanced Architecture Systems (Dr. Steven Griffin)

Prior performance models are physics based descriptions of the components and subsystems that form images in the non-terahertz regime. These are generally either infrared (IR) or visual optical modeling systems or electromagnetic field (EMF) based modeling systems in the millimeter wave (mmwave) or at radio frequencies (RF). Though the terahertz (THz) regime has many characteristics in common with these neighboring regions, some aspects are significantly different. After extensive research and a number of meetings, a general approach to THz modeling was established. Prior details were summarized in the three, six, nine, twelve and fifteen month reports. Details of the completion of milestone one, two and three were reported in the progress reports.

This work compliments and enhances existing Army Research Laboratory (ARL) programs by concentrating on selected issues of mutual interest. This includes corrections for deviations from the classical optical performance model descriptions. On the first year proposal cycle, three milestones received particular emphasis.

4.1　Support performance modeling of metal and plastic target reflectivity and emissivity.

Direct interaction with ARL Maryland and NVESD Virginia was used to establish the current state of the art with regard to target reflectivity and emissivity with a view towards advancing performance modeling. Modification of existing performance models was accomplished by reviewing existing ARL / NVESD based models with existing classic descriptions such as Donovan's and by the incorporation of additional empirical data. Significant differences and causative factors were used to determine performance modeling recommendations. This work supports the Army's performance modeling efforts and improves performance predictions or decisions resulting from those simulations.

To accomplish this, four actions were proposed. The third action was modified with ARL approval and coordinated with recent equipment and personnel changes. All have been completed.

Enhancement of model for reflectivity and emissivity of metals from prior ARL / NVESD modeling and classic systems is complete. Donovan's theory of metals [Donovan,1967] has proven to be very durable for the modeling of metals at high frequency and is recommended for incorporation into the radiometric description. This required the generation of a MatLab implementation of the model. Inquiries at various libraries and universities in the Washington, D.C., Knoxville, TN and Memphis, TN areas plus assorted research facilities of the army (ARL, NVESD, etc.) were incorporated. Responses from the University of Illinois and University of Massachusetts at Lowell were also utilized.

The University of Memphis is obtaining additional THz equipment from the Navy (ONR – DURIP) supportive of data collection for validation purposes but delivery has been delayed. After consultation with the ARL contract monitor, modification to the investigation reduced travel expenditures for Jefferson Lab. This revised plan was implemented to accommodate post proposal reductions in funding available. To accommodate the net effect of this validation data was obtained from third parties.

In addition, information regarding plastics modeling was provided by the Redstone Scientific Information Center (RSIC). The principle development for plastics was the inclusion of the water absorption common to most plastics. Because water has such a strong interaction at THz frequency even small amounts included in the body of plastic can overwhelm other factors - not only changing the loss tangent but also possibly producing and / or dominating frequency dependences. This occurs because the nature of most polymers creates molecular lumps of long molecular chains. Water, driven by time and temperature, can migrate along the boundaries and into these lumps producing plastics that not only contain significant water percentages by weight but whose percentage is a strong function of hydrometric history. Some plastics have actually been designed to eliminate this effect. An example of this is cross-linked, fused polystyrene, which is used by the electronics industry at high frequencies specifically because it excludes water.

This effect should not be under estimated. Some nylons contain 30% or more water by weight - depending on its' history. The rate of water uptake and release is a strong function of surface to volume ratios and, as a result, particularly pronounced for fabric fibers. Denier, stress, and hydrometric history impact the water weight percentage in cloth. This created an overlap with allied THz efforts under independent sponsorship. Efforts have been made to coordinate and leverage with those programs.

Complete documentation of technical results is contained under separate cover. Below is a summary of some pertinent details.

4.1.1 Reflectivity and emissivity of metals

Reflectivity, emissivity, and absorption are intimately related quantities. Radiometric system modeling provides some standard representations which are utilized here.

Starting with a given complex index of refraction yields:

$$\Gamma_\perp^b = \frac{1 - \dfrac{\eta_1}{\eta_2}}{1 + \dfrac{\eta_1}{\eta_2}} = \frac{1 - \sqrt{\varepsilon}}{1 + \sqrt{\varepsilon}} = \frac{1 - n_r + n_i\, j}{1 + n_r + n_i\, j} \Rightarrow \left|\Gamma_\perp^b\right|^2 = \Gamma_\perp^b \cdot \Gamma_\perp^{b*} = \frac{(1 - n_r)^2 + n_i^2}{(1 + n_r)^2 + n_i^2}$$

$$\Gamma_\parallel^b = \frac{-1 + \dfrac{1}{\sqrt{\varepsilon}}}{1 + \dfrac{1}{\sqrt{\varepsilon}}} = \frac{1 - \sqrt{\varepsilon}}{1 + \sqrt{\varepsilon}} = \Gamma_\perp^b \Rightarrow \textit{Same result}$$

Following the standard radiometric treatment which assumes an infinitely thick thermal body with zero transmission yields:

$$\varepsilon\,(emissivity) = 1 - \frac{(1 - n_r)^2 + n_i^2}{(1 + n_r)^2 + n_i^2} = \frac{2}{(n_r + 1) + \dfrac{n_i^2}{n_r + 1}}$$

MatLab based simulations can be made of the complex index of refraction, reflections and emissivity for metals and plastics versus frequency across a broad band. As an example, consider the broad-band description of the copper complex index in Figure 4-1A. In this figure, common regions are labeled: radio frequency and microwave (RF), millimeter and sub-millimeter wave (MM-wave), terahertz (THz), long wave infrared (LLIR), medium wave infrared (MWIR), visible wavelengths (Vis), and X-ray (X-ray). In the THz region of the figure, both the real and imaginary components of the complex index of refraction begin to deviate from a polynomial description and separate from each other. This is due to effects associated with the plasma frequency and the departure from the Boltzmann non-relaxation assumption. Neither effect is normally included in modeling metals in the millimeter and sub-millimeter region. They must, however be included in the THz description.

A similar description can be constructed for copper reflectivity and is presented in Figure 4-1B. Validation of the results was accomplished by comparison of modeling prediction with actual data from a variety of sources. Such phenomenological data is scarce for the THz region and tends to be concentrated at the lower frequencies. [Bolivar,2003] Fortunately, due to atmospheric window issues, this is the region of most interest for current applications. In particular, available data is at or near 650 GHz and is plotted in figure 4-2A. Multiple sources yield the data represented by the "X". Notice the extremely fine scale of the vertical axis. Values have been determined to three significant places where subtle theoretical corrections have been applied to actual readings. The error bar associated with the "X" is approximately three times its' size on this figure's scale. As can be seen, the model's predictions agrees within the error-bar of the mean (X) of the empirical data available as of date. Similar curves can be generated for other metals.

A similar comparison between modeling predictions of copper emissivity and the empirical data available for the THz produces Figure 4-2B. The same comments made previously still apply to this case. Additional metals and plastics may also be modeled.

35

Complex Index of Refraction
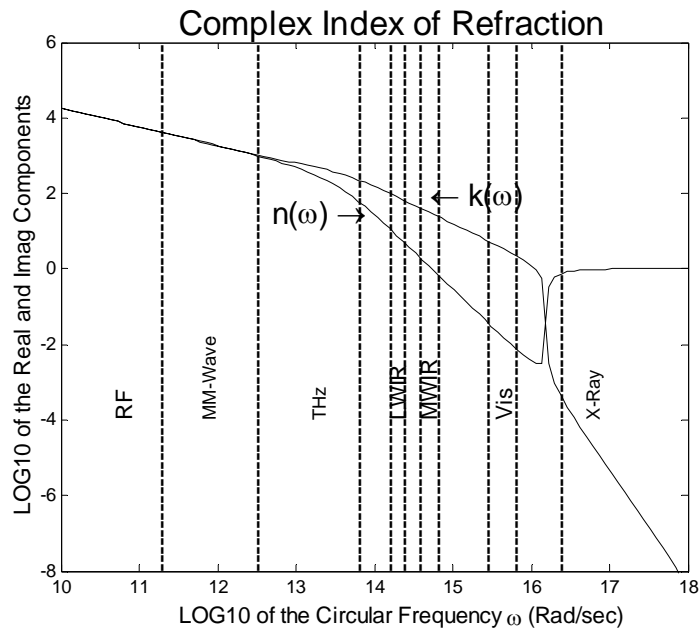
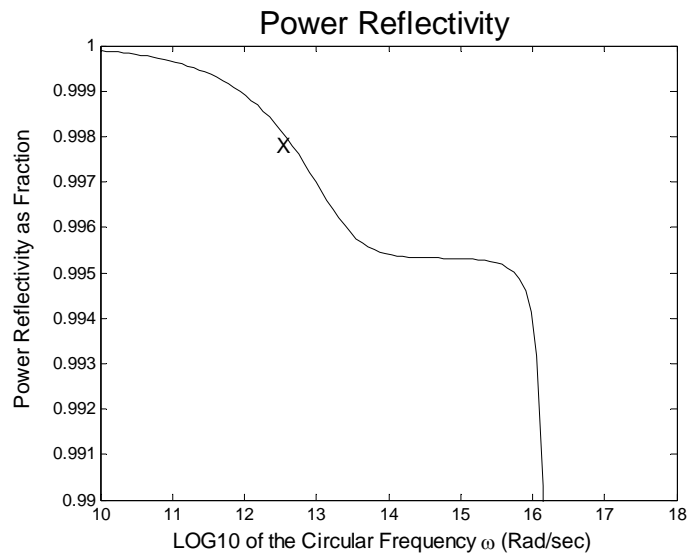(A) Real (n) and imaginary (k) components of copper complex index of refraction
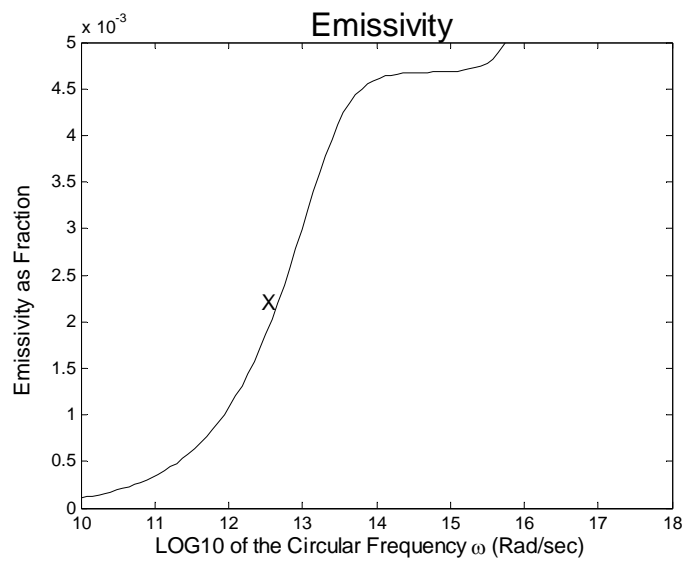
Power Reflectivity
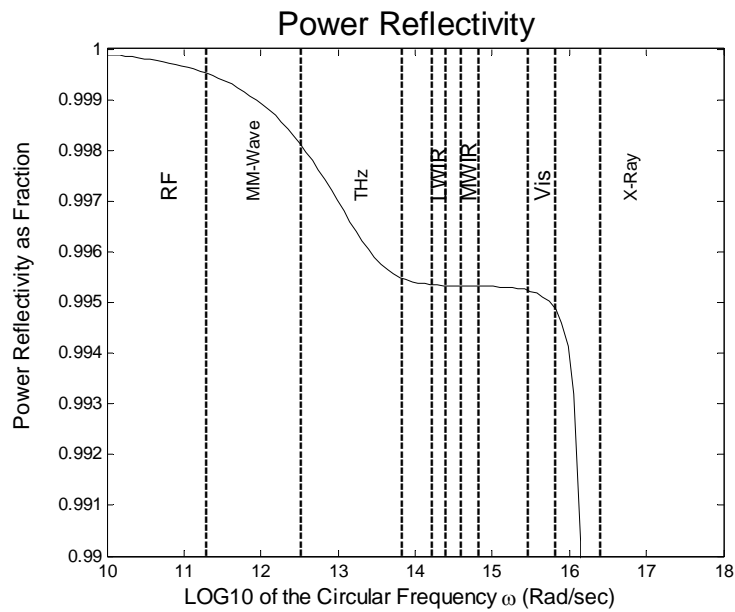
(B) Copper power reflectivity across a broad band

Figure 4-1 Intermediate Computation of Metal Behavior

(A) Power reflectivity for copper with available data over-plotted

(B) Modeling prediction of copper emissivity versus available data

Figure 4-2   Reflectivity and Emissivity of Copper

4.1.2 Reflectivity and emissivity of plastics

At lower frequencies, plastics are generally effective dielectrics with relatively low losses. As the THz regime is approached, a number of additional factors become significant. Being complex organic compounds, various carbon chain resonances and side chain molecular absorption modes can become factors. However, to the first order these interactions tend to be over whelmed by a practical consideration. Plastics typically incorporate a significant mass of water in their internal structure [Simonds,1949]. Chemical molar analysis indicates the water density is consistent with a liquid state. This water is in equilibrium with the environmental sources. The water migrates along macromolecular boundaries into the body of the plastic. Most plastic's macromolecules are not linear but rather resemble a ball of string. Environmental water may penetrate not only the body of the plastic material but also penetrates the folds and creases of the macromolecule. Normally, inclusion of water into a solid matrix would dramatically alter the water's electrical properties. For plastics however, the covalent nature of most plastics and the extremely polar nature of the water molecule limit that effect. The nature of the water inclusion is surface absorption along the intra- and intermolecular interfaces. A process so pronounced, that some common plastics under some circumstances can be 10's of percent water by mass. To control this variable, electrical standard testing procedures prescribe a standard humidity / temperature treatment prior to the determination of dielectric constant, etc. [Brown,2000]. The time constant for the water uptake and devolution varies from minutes to days depending on the particulars of material and environment. The standard electrical test procedure is intended to produce equilibrium prior to the determination of electrical properties. Because of the long time constants involved in the water absorption process, practical plastics exhibit hysteresis with their current state determined by environmental history as well as material properties.

At THz frequencies, water tends to dominate the electrical properties intrinsic to the plastic. Thus the actual field behavior of plastics under THz illumination is a function of all the previously named parameters. A few plastics avoid this water dominated behavior [Vasile,2000]. These tend to be cross-linked plastics, where side chain linkages between adjacent macromolecules impede water absorption. A classic example of this is cross-linked polystyrene which is a low loss, transparent material from DC through THz up to some near IR hydrocarbon absorption lines. Past these lines, it regains its optical clarity until electronic transition lines are encountered in the near UV. As such, it makes an excellent material for THz optics. It is, however, a rare exception. Most plastics contain significant quantities of water which dominate the absorption characteristics and affect the total index of refraction. Water tends to be distributed at a scale which is small compared to the wavelength associated with the THz region. The electromagnetic field cannot see the fine details but rather sees the water's loss at the appropriate mole fraction and an index intermediate between water and plastic. The index is not greatly modified because the typical plastic and water index are not terribly different to begin with and the mole fraction of water is typically a few percent.

Taking this into account, a simple complex-index-based model treats the plastic's losses (imaginary component) as trivial and the index (real component) is prorated between the plastic and water values. The plastic's effective loss is simply a molar prorated version of the water loss. Details of the incorporation and structure of the model parallel that for metals above. Crucial to this is the assumed molar water content of the plastic. Since this parameter cannot be determined in an application-meaningful way, it is left as an input and will probably be set to a typical value. Because THz imaging depends on relative (not absolute) contrast, this is not a major modeling limitation. The results are simple equations using $n_r = 1.6$ and $n_i = 0.6$ as typical values.

$$N = \left(\mathrm{Re}(N_p) \left(\frac{1 - FW}{1 - FWS} \right) + 1.6 \left(\frac{FW - FWS}{1 - FWS} \right) \right) - 0.6\, FW\; j$$

Where N is the complex index,
FW is the molar fraction of water,
FWS is the molar fraction of water at standard conditions, and
N_p is the complex index of refraction for the plastic under standard conditions.

4.1.3 Conclusions regarding metals and plastics

Metals and plastics can be modeled effectively in the THz frequency regime. Metal modeling requires release from the Boltzmann non-relaxation assumption and inclusion of plasma frequency effects differentiating it from the assumptions typically made at sub-millimeter frequencies and below. Plastics are dominated by water behavior to the point that hydrological history and water material properties over whelm the intrinsic behavior of plastic within the THz band. The models compare favorably with the available empirical data.
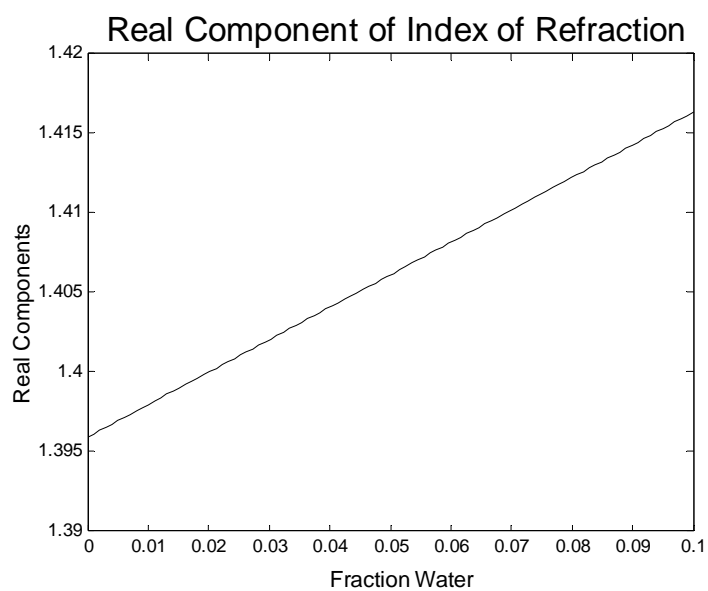
(A) Real component of Index of Refraction
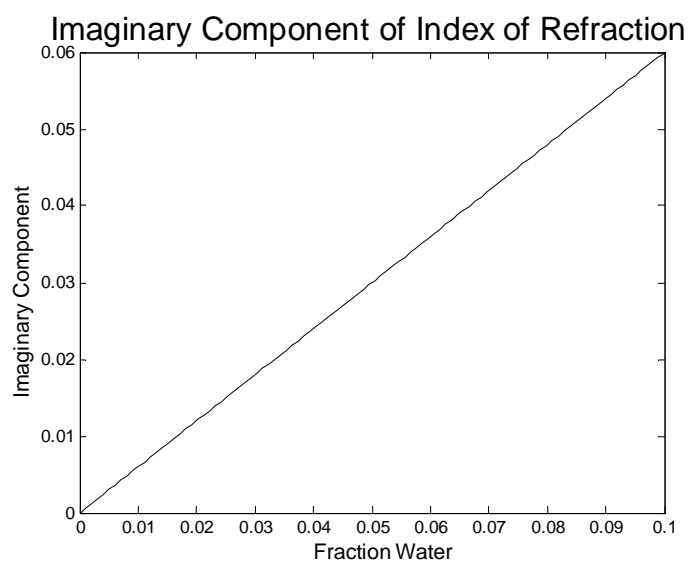
(B) Imaginary Component of Index of Refraction

Figure 4-3 Complex Index for water dominated plastic

4.2 Support performance modeling of water and human target reflectivity and emissivity.

Modification of existing performance models was accomplished by reviewing existing ARL / NVESD based models with previously assembled existing classic descriptions. Limited empirical validation was developed at the University of Memphis as compatable with the delayed delivery of the ONR DURIP equipment. Significant differences and causative factors were used to determine performance modeling recommendations. This work should enhance the Army's performance modeling efforts and improve any performance predictions or decisions resulting from those simulations.

To accomplish this, four actions were proposed. The third action was modified with ARL approval and coordinated with recent equipment and personnel changes.

Enhancement of model for reflectivity and emissivity of water, ice, and snow from prior ARL / NVESD modeling and classic systems such as Ray is complete. Porting of MatLab code to the new University of Memphis High performance Cluster (HPC) has been delayed as the software is just now becoming available. Inquiries at the University of Memphis, Vanderbilt and University of Tennessee (Knoxville) libraries have produced considerable phenomenological detail for incorporation of the model for water. Reduction in travel funds has eliminated Jefferson Laboratory involvement as previously cited.

The incorporation of human tissue into the reflectivity and emissivity models based on prior biologic measurements is complete. The University of Tennessee Medical Library (Memphis) has been consulted. Some additional information was obtained from Vanderbilt. Incorporation of this into MatLab emphasized the dominate role of water. The outer skin layers are relatively transparent to THz energy. A fact utilized to develop a number of biological sensors for the upper and lower skin layers. Since the interior body layers are essentially a matrix containing predominately water and the water interactions are so strong, the best first order model is a body of water situation a few millimeters below the skin surface. Originally human skin validation was to be undertaken using approximately one square inch sample of living tissue as a THz target Given the delays in the receipt of the ONR DURIP equipment, the dominate nature of water in the tissue and the minor impact of the body matrix on the first order results, it was decided to forgo the live tissue sample.

4.2.1 Reflectivity and emissivity of water, ice and snow

As the second year unfolded it became increasingly obvious that the domination of THz spectra by the various states of water rendered more detailed analysis mute. Specifically anything that could contain water – particularly if the water percentage varied depending on history – would have its' characteristics over whelmed by the included water. Water is such a strong absorber in the THz regime that the contribution due to the matrix that holds the water is trivial. As such, thorough characterization of water was essential, not only in its' own right but because it tends to dominate the behavior of many materials such as plastics, biological tissues including human tissues, etc. Metal stands out in THz

images partly because it naturally excludes water. Thus, a relative contrast is generated against a soggy background.

In the THz regime the assumptions that work for far Infrared and the microwave are in transition. This occurs for water, ice, and snow in a manner analogous to that cited in section 4.1 for metals. Thus the limiting case normally used to describe water in the microwave and far infrared regions is not adequate for the THz. The fundamental physical mechanisms are in transition from one limit to another and all have to be included for an accurate description. The electrical conductivity dominated behavior, small dielectric losses and impurity issues that dominate the low frequencies give way to the classic Debye relaxation description in the microwave band. In the far infrared, molecular absorption lines dominate the Debye description. In the THz, the Debye description is significantly affected by the tails of the higher frequency absorption lines and neither can be ignored. In Figure 4-4 is a summary plot of a computer model for the real (n) and imaginary (k) components of the complex index of refraction for water at 25°C.
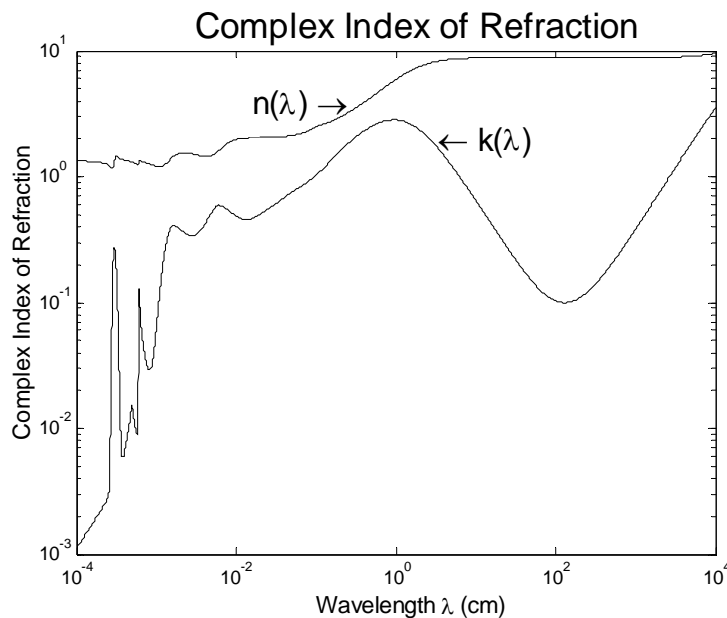
Figure 4-4   Complex index of refraction of water at 25°C

The figure is highly compressed; however, the model is capable of expanding any chosen range a fine scale. THz frequencies correspond to approximately 0.1 cm wavelengths. By referring to Figure 4-4, it can be seen that the total index components, both real and imaginary, begin to deviate from the classic Debye description in the THz band. This is the result of the impacts of the tails of the resonant lines at higher frequencies and should not be neglected. The complex index was chosen to represent the emissivity information

because it lends itself to application across a broad range of frequencies. The complex index of refraction can be converted to reflectivity and emissivity by standard techniques.

$$R = \frac{(-1+n)^2 + k^2}{(1+n)^2 + k^2} \quad E = 1 - R \quad Assumes \quad T = 0$$

Where R-Reflectvity, E-Emissivity, T-Transmission

Applying this gives Figure 4-5 – again for liquid water at 25°C. It should be noted that the characteristics of all the states of water are functions of temperature. Different temperatures of ice, for instance, demonstrate different emissivities. This is a characteristics sometimes utilized for remote sensing. Such behavior may result in differential contrasting of different temperature water in THz images due to variations in power reflectivity as seen in Figure 4-5A

THz again falls at the transition point where the emissivity and reflectivity is changing rapidly with respect to frequency and temperature. For space limitation reasons, the temperature figures are not included but are published under separate cover. Similar behavior can be noted with respect to ice. Once again, the temperature of the ice has a significant impact on the complex index of refraction and as a consequence the reflectivity and emissivity.

One of the impacts of the strong dependence of emissivity on frequency pertains to the swept frequency systems. A common motivation for sweeping frequency is to modify artifacts caused by phase interference associated with imaging using narrow frequency bandwidths. Most current THz sources for active imaging are naturally narrow in band width – sometimes made more so by atmospheric transmission characteristics. Because the wavelength at THz frequencies is on the order of 0.1 millimeters, details such beard stubble can produce dramatic image effects. These narrow bandwidth, (~monochromatic) temporally coherent effects can be reduced by sweeping the frequency at rate fast compared to the system integration time. Unfortunately, this will make the reflectivity and emissivity also sweep through values. The impact of this for water dominated materials such as beard stubble is not know to the author and is a topic of potential future study.

Power Reflectivity
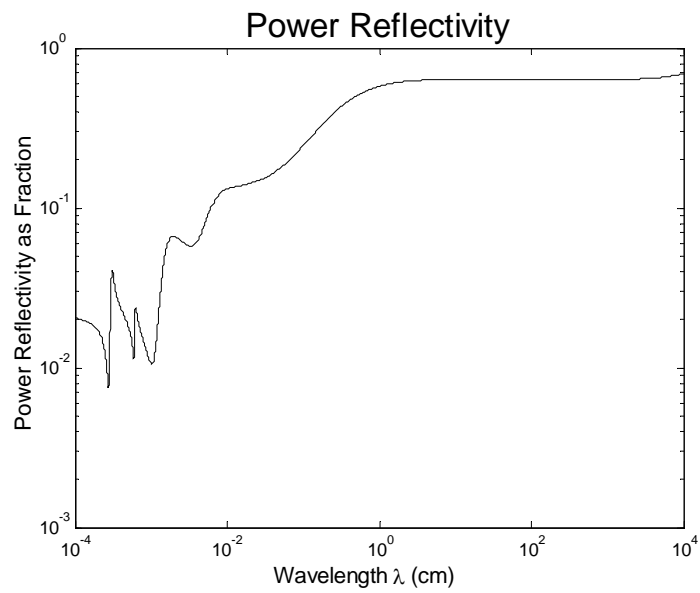
(A) Reflectivity of water at 25°C
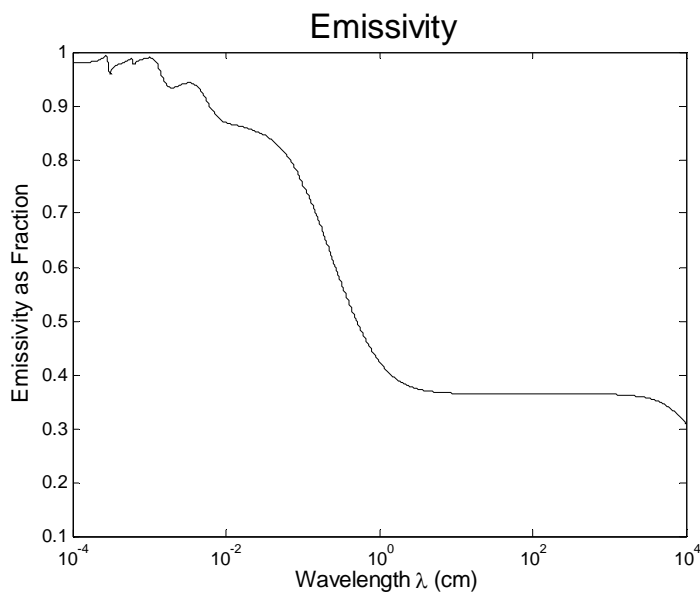
Emissivity

(B) Emissivity of water at 25°C

Figure 4-5   Reflectivity and Emissivity of Water at 25°C

44

Similar behavior can be noted with respect to ice. Once again the temperature of the ice has a significant impact on the complex index of refraction. In Figure 4-6, the complex index of refraction for ice at 0°C is plotted versus wavelength.   In this case the real portion of the index is relatively stable because of the extremely weak effect of Debye relaxation on this solid.   Only a few, very slight, resonance effects are seen in the infrared. Similarly temperature has little effect except in the neighborhood of the 'n(λ)' label.   Variations in temperature cause the shoulder in "n" point to by the arrow to translate in frequency.

In the case of the imaginary component 'k' (losses), the opposite extreme holds.   The value changes rapidly for both frequency and temperature variations.   The THz band is near the minimum of the curve and the corresponding values for the complex index can easily by an order of magnitude or two.
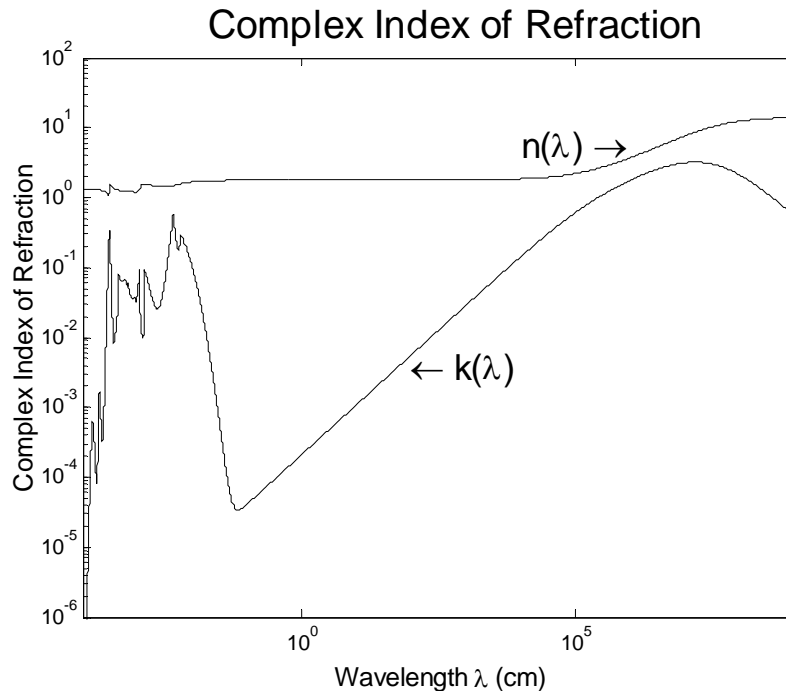
Figure 4-6   Complex index of refraction of ice at 0°C

The corresponding reflectivity and emissivity curves are shown in Figure 4-7.   Once again the reflectivity and emisisvity curves are just beginning to leave a flat region as you enter the THz band from lower frequencies.   This is due to the impact of the tails of infrared resonance lines on the lowetr frequency behavior with the same implications cited before.

Details of snow are similar and omitted for brevity.

Power Reflectivity
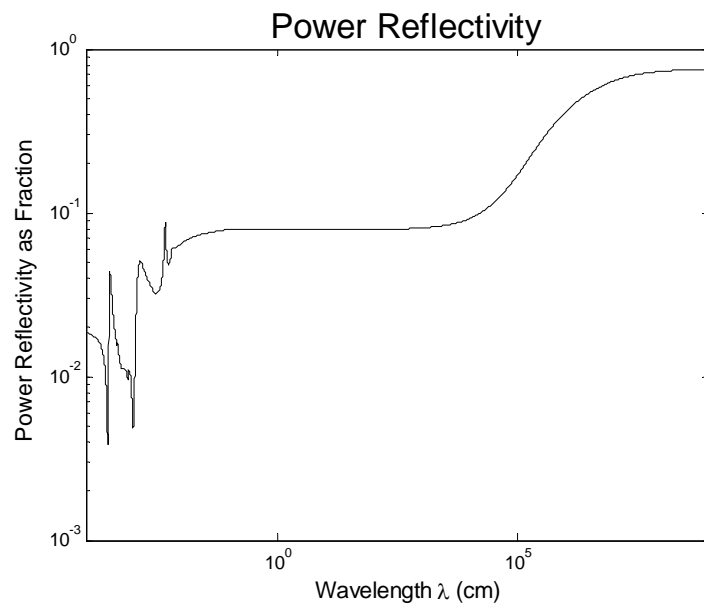
(A) Reflectivity of Ice at 0°C
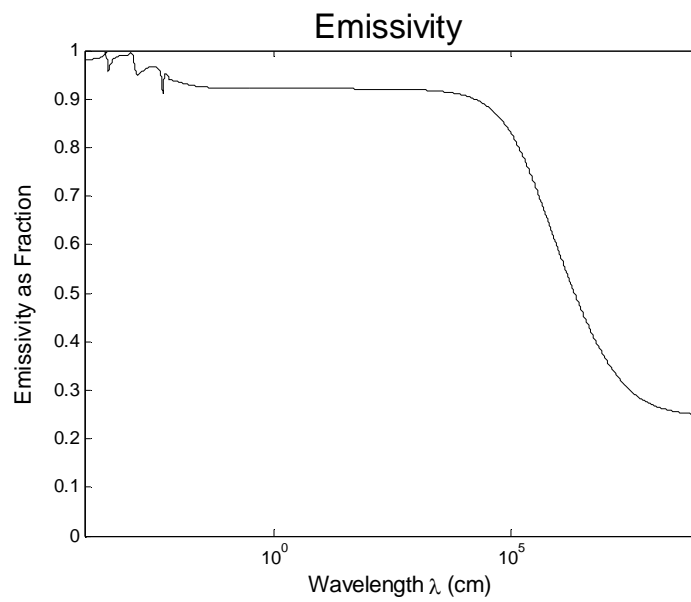
Emissivity

(B) Emissivity of Ice at 0°C

Figure 4-7   Reflectivity and Emissivity of ice at 0°C

4.2.2 Incorporation of human tissues

Water behavior dominates the behavior of human tissue. The matrix effect of the tissue structure is second order in impact. Biological studies utilize these second order effects for diagnostic purposes. These techniques work because the upper layers of body tissue are fairly transparent to THz radiation and the low photon energy at THz frequencies presents little ionizing radiation hazards. Because the upper tissue layers are fairly dry, the THz radiation penetrates through the upper layers. Once the THz radiation reaches the lower wet region, it is rapidly attenuated. The net result is a weak, second order signal from the dry upper tissue layers superimposed on a moderate "first surface" reflection from the deeper water layer. The transmitted signal is rapidly attenuated in the wet region. As is typical for the THz regime, emission is nil. The net result from a diagnostic standpoint is a weak signal correlated with the upper layer tissue structure against a background of THz reflection noise. The resulting SNR is low but yields helpful information regarding the upper tissues after enough image processing.

For the perspective of THz imaging, the second order affects of the upper tissue layers is not significant. To the first order the system may be modeled as a water barrier supported by a tissue matrix. The matrix effects of the tissue are trivial. Thus leaves just the water molded into compound 3-D curves. Generally the curvature occurs over many wavelengths (the exception being hair) so that classic models regarding impact of a plane wave on an air to water interface may be used. The details of the water behavior are incorporated into the previous section.

Given the delays in the receipt of the ONR DURIP equipment, the dominate nature of water in the tissue and the minor impact of the body matrix on the first order results, it was decided to forgo the live tissue sample at this time.

4.2.3 Jefferson Laboratory validation

Subsequent to the original proposal for the Center for Advanced Sensor – Year 2, the funding available was cut by a significant percentage. This was under taken at congressional request. This in turn necessitated the cutting of some expenses associated with this project. After this situation became known, the University of Memphis was notified of the receipt of an ONR based DURIP for $188,602.00 in THz related equipment. As a result it was decided – in consultation with the ARL contract monitor – to terminate this activity to rebalance the budget. Unfortunately the ONR equipment was greatly delayed.   Independent validation was obtained from other sources including collaborators and through the use of borrowed time on some loaned Army THz equipment. Though the additional data generated was limited, it combined with historical data allowed the completion of this portion of the contract. It is anticipated that the ONR equipment will be received soon and additional new data generated at that time.

4.2.4 Conclusions regarding water and tissue

It was determined that the water dominates the behavior of human tissue. Utilizing classic plane wave based reflection, absorption and transmission coefficients was recommended for the modeling of human tissue. The upper layers contribute little to the description that justifies their incorporation. They should be treated as transparent

followed by a water surface a few millimeters below the skin. The modeling of water depends on its' state – liquid, ice, snow. Models describing each were implemented. Ice and snow are of primary interest for scene backgrounds. The water model is important for a variety of applications where the water characteristics dominate its' supporting matrix. In the interest of trading brevity against completeness, it was decided that human tissue was best modeled as a matrix containing water. The water starts a few millimeters below the skin surface and exhibits standard behavior at the ambient temperature. The second order matrix effects of the tissue are slight but measurable and are best left to biological applications.

4.3 Develop Techniques to Enhance THz Target Performance in Imaging Applications through unique procedures for improved contrast, noise reduction, chemical signatures, etc.

This research advances the development of processing techniques that take advantage of unique target properties to improve THz imaging system performance. As such – this portion of the project was implemented after the completion of milestones one and two. This allowed the incorporation of target results into recommendations regarding the THz image processing. Of principle consideration here is the interaction of the eye CTF response with target characteristics related to noise and resolution. Emphasis was placed on techniques designated as most promising by ARL and NVESD.

To accomplish this, three specific actions were developed:

4.3.1 The processing techniques that leverage eye CTF response to improve THz imaging system contrast were investigated.

A number of processing techniques, that leverage the CTF of the eye to improve THz imaging response, were considered. Of these, the behavior of clutter due to water distributions in objects such as fabrics, was emphasized. In the process a new interpretation for clutter in spatial systems was developed. It was applicable to TIFT1B modeling and has been incorporated into proposal work towards TIFT2. To understand this result, consider first Figure 4-8. This is a plot of the Contrast Transfer Function (CTF) of the human eye. This establishes the minimum eye detection versus spatial frequency. The vertical axis is scaled in contrast values where a value of one indicates that twice the background average luminescence (signal average plus noise) equals the peak to peak value of the signal. At a CTF value of one all the average value is equal to the signal. As will be seen in a moment, this is important in the description of THz clutter by $1/f$ noise.

In addition to the eye CTF there is also an eye MTF. This establishes the gain associated with the eye. Eye MTF is a function of many parameters such as average luminescence. A example response curve is shown in Figure 4-9 below.

In the previous section (4.2) the predominance of water in determining behaviors at THz frequencies was established. In addition to having a very strong effect, it also is

ubiquitous - not only in the atmosphere but also in many "solid" materials such as plastics, cloth, etc. Thus the imaging behavior of these materials is dominated by the presence of water and the hydrological history of the material that determines its' water content. One of the distinguishing characteristics of metals is that they effectively exclude water. Thus THz images may be thought of as metal on water background imaging. This provides contrast not only for the determination of high metallic content objects but provides relative contrasting of the water containing materials. Because the water content of a given object is a function of its' history, absolute contrast is not an effective marker. However, for imaging applications it is the relative contrast that maters. In fact the eye generally responds to relative values – not absolute. Thus even similar materials that have undergone a different hydrological history may be imaged against each other.

Within this context, the residual none-equilibria of water concentrations in materials represent a potential spatial noise that may be interpreted as clutter. Typical material time constants that describe the absorption and transport of water may be on the order of hours or days. As such, many materials never really reach equilibrium with their surroundings. This may be an advantage for relative contrasting in images but also means that a single object rarely achieves water uniformity. The residual "clumping" of water concentrations will produce similar clumps in THz reflectivity, absorption and transmission that may be a significant source low frequency spatial structure.

Considering Figures 4-8 and 4-9, it can be seen how sensitive the eye is to low spatial frequency noise (clumps). Though there is much discussion regarding the exact definition of clutter, there is general agreement it is a low spatial frequency effect. For the purposes here, clutter can be divided into fixed pattern noise (irrespective of source), 1/f noise, the interaction of these within the non-linear characteristics of an imaging system, and other unwanted signals. Again the intention here is not so much to solve the debate as to narrow the discussion to terms that are relevant here. Fixed pattern noise are spatially fixed, noise pixels due to poorly performing elements in focal plane arrays, specular glints in a fixed field of view, etc. Spatial flicker (1/f) noise is the ubiquitous results of minor non-linearity present in all physical phenomena that has the unfortunate property of being invariant under linear superposition. This means that post detection, image processing whether analog or digital tends to reduce image noise but has no effect on the 1/f noise leaving it as a primary noise component. This is because most post detection processing is the repeated application of techniques based on linear superposition which does not affect 1/f noise. Classic non-linear techniques such as lock-in-amp chopping help but residual 1/f behavior in phase still produce annoying phase-lock drift. The ultimate treatment of 1/f noise remains an area of significant research.

From Figures 4-8 and 4-9, the spatial frequency region from a few milli-cycles/ milli-radian to approximately one cycle/milli-radian is identified as the principle range of interest for 1/f noise analysis. Within this range the eye has both significant gain and insensitivity to other noises to interpret the 1/f spectrum as image clumps. Such unwanted, non-descript objects are a major distracter that a viewer would typically call clutter. Behavior consistent with this has been seen in the few available THz images and

needs to be characterized with regards its' impact on potential THz imaging. Before proceeding too far in this direction, the cause of the 1/f noise for THz applications of immediate interest needs to considered. This is developed in section 4.3.2.
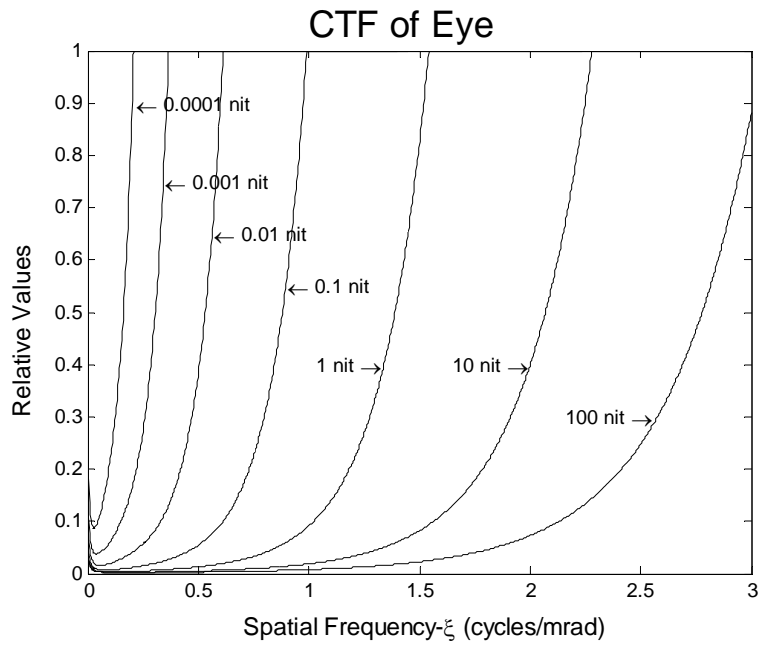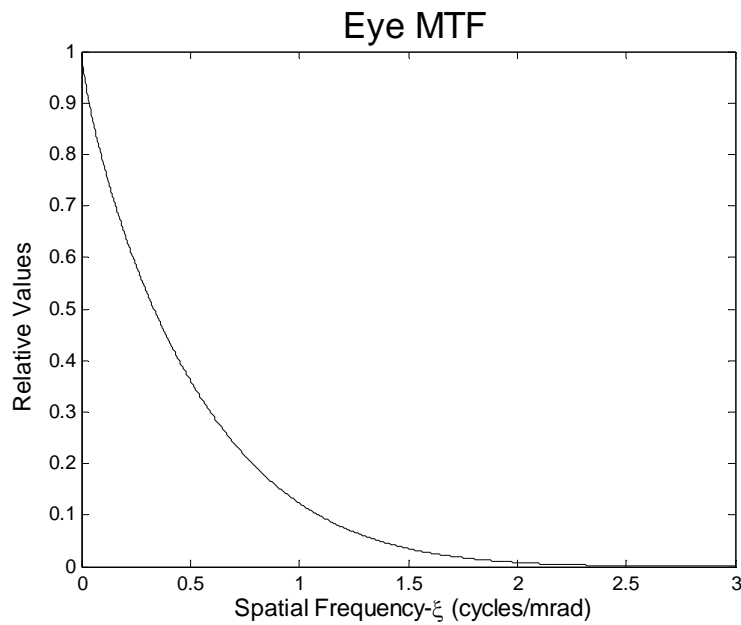

Figure 4-8 Eye CTF

Figure 4-9 Eye MTF

4.3.2 The development of processing techniques to improve THz imaging system response with regards to temporal and spatial noise performance.

As an example of processing techniques to improve THz imaging response to temporal and spatial noise, the development of clutter in moist fabrics was considered. Assuming the use of heterodyne detection techniques, temporal noise was modeled by traditional techniques such as system noise temperature and found to be trivial for this application. Traditional spatial noise processing techniques reduce the spatial frequency base noise to acceptable levels but leave a difficult spatial noise residue usually called clutter. Modeling this as a 1/f or flicker noise is demonstrated to be useful and provides insight to potential new techniques for treatment. It is more than coincidence that both clutter and spatial 1/f noise are ubiquitous. It has been shown that they stem from fundamental physical requirements. In addition they both cannot be removed by conventional processing that is expressible as additions and multiplications. To be a little less abstract and hopefully less esoteric, the special case of moist fabrics was considered. The results are more general than this, which was chosen for illustration purposes - making the issue a little less murky.

For fabric used in clothing there is significant transport of water along and through the material. The fabric water content is the result of an equilibria between various sources such as human perspiration, atmospheric relative humidity, spills, etc. and sinks to the atmosphere or other, dryer objects. The fabric acts as a conveyer to transport water from high concentration to low and ultimately dissipates it to the air. Fabrics which do not do

51

this are judged to be "uncomfortable" and are simply not worn. The processes involved in this transport of water result in a second order "clumping" of water concentrations. After processing through the eye MTF and CTF this results in a 1/f spatial noise behavior that is interpreted as clutter in THz images. To get a feel for this consider figure 4-10.

Water Transport along Fabric
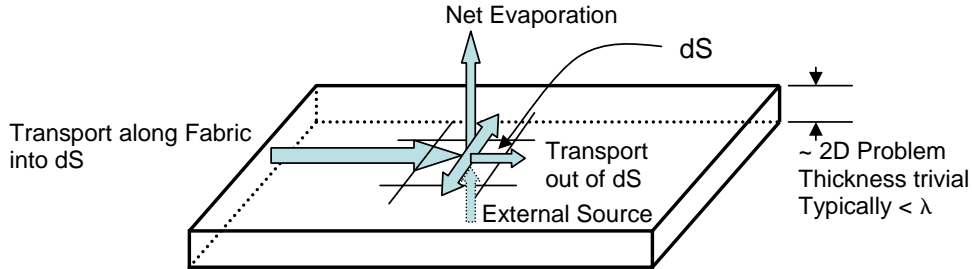
Figure 4-10 Water Equilibrium in Fabric

In this figure a small swatch of clothing fabric is represented. Generally the fabric thickness is small compared to the wavelengths of interest in the THz regime. As a result the problem reduces to a two dimensional description. In the figure the water transport is described for a small, differentiable, surface element - dS. Into this surface element you have the net external sources – perspiration, etc. and losses to external sinks, such as evaporation. In addition there is transport of the water along the fabric both into and out of the differential element. To understand this from a physics stand point the problem can be reduced to a one dimensional analogue.

In 1D

$$K\left(\frac{W(x-dx)-W(x)}{dx}\right) = K\left(\frac{W(x)-W(x+dx)}{dx}\right) + C\ W(x)$$

Where the range of 2 *dx is indicative of a Laplacian*

Or more formally it can be described in three dimensions as:

$$0 = -\frac{\partial W(x,y,t)}{\partial t} = \overline{\nabla} \bullet \left(-\nabla\left(K\ W(x,y,t)\right)\right) + C\ W(x,y,t)$$

52

Which becomes:

$$\nabla^2 W(x,\, y) = \gamma\, W(x,\, y)$$

$$Where\ \overline{\nabla} \bullet \left(\nabla W \right) \equiv \nabla^2 W \quad and \quad \gamma \equiv \frac{C}{K}$$

Now, the resulting equation $\nabla^2 W(x,\, y) = \gamma\ W(x,\, y)$, called the Helmholtz equation, is generic description of water transport in a fabric. The normal solution technique for this equation is separation of variables into a convenient coordinate system. Special cases of this equation include a homogeneous form (γ=0) sometimes called the spatial component of the diffusion, heat or telegrapher's equation. Equations of this form describe centro-symmetric physical phenomena – phenomena where there is a restorative "force" to an equilibrium. This is a math way of saying that the water flows from the surrounding regions of high concentration to fill regions of low concentration – be it slowly.

There exist mathematical proofs that show that centro-symmetric phenomena are of necessity energy non-linear and homogenous. A physical phenomena described by the Helmholtz equation is energy non-linear and homogenous. It is known that a chaotic system exhibiting nonlinearity plus homogeneity will generate 1/f (flicker) noise. At low signal strength (noise levels) the system is dominated by chaotic behavior giving rise to noise in the spatial distribution of water exhibiting a 1/f power spectral distribution. The spatial appearance of such a noise distribution is spatially distributed, weak strength, "lumps and clumps" superimposed over the principle water distribution

Because of the nature of 1/f noise, subsequent processing of the image cannot remove it. This noise is invariant under the operations of addition and multiplication. In fact subsequent processing to remove spatial noise tends to emphasize it as the general background noise falls. This is particularly true for extremely weak signals. Since almost all post detection, processing algorithms obey linear superposition, 1/f noise generated clutter is ubiquitous in images. Be aware that this does not apply to clutter as unwanted signal information – only to the subclass generated by 1/f noise.

In figure 4-11 is the magnitude of the spectrum of 1/f noise plotted versus the spatial frequencies in cycles / milliradian. It should be noted that the vertical scale in this figure is milli foot-Lamberts as a consequence of the spectral density nature of the function.

Milli Foot-Lamberts = Foot-Lamberts / (cycles/milliradian)

The actual luminescence represented by this figure is 100 Foot-Lamberts – a high but not unreasonable value. This noise is subsequently processed by the eye MTF and CTF giving a slightly different shape documented in Figure 4-12. The eye's rising insensitivity at very low spatial frequencies documented in Figure 4-8 has the mathematically convenient impact of concealing the singularity at zero. Other wise it has

53

little impact at low frequencies. However, the shape of the curve at mid and high spatial frequencies is changed by the cumulative impact of eye MTF and CTF. The resulting curve is rich in low frequency components and with the inclusion of the proper phase relationship produces spatial clumps (clutter) in the spatial domain. Details of this are too involved for this document and are reproduced under separate cover.
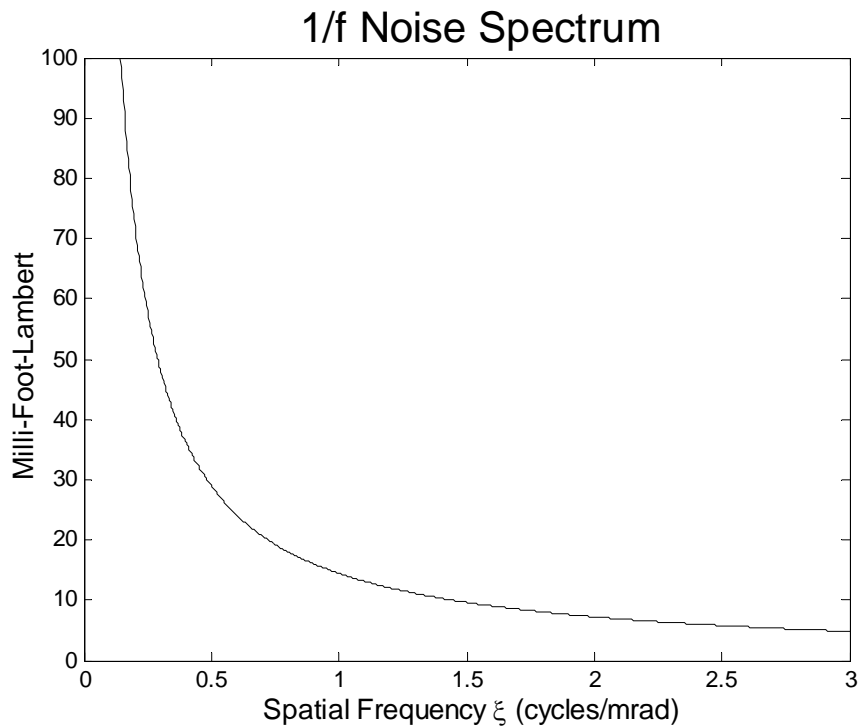
1/f Noise Spectrum

Figure 4-11 1/f Noise Spectrum

Spectrum with Eye Response
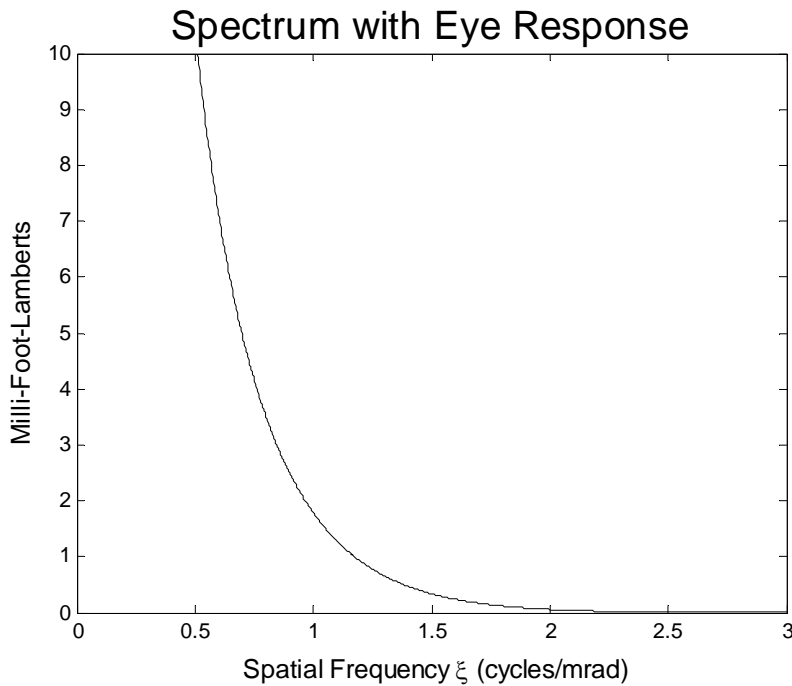
Figure 4-12 1/f Noise Trimmed and Attentuated by Eye Response

4.3.3 The development of processing techniques to improve THz imaging system response with regards to unique chemical signatures of preferred target material was modeled.

Compressive sensing techniques were applied to chemical signatures. The use of high energy materials at a university is complicated. Therefore alternative chemical signatures were considered to demonstrate the potential of the application of this technology. Generic spectroscopy was also avoided as the results of the data overload associated with combining detailed spectrums at every point in a two dimensional image. Such large scale data fusion is the emphasis of other research activities and is not considered here. The emphasis here was the collection of selective temporal frequency data on a two dimensional image. The intent was to produce chemical signature identification without collecting complete spectrum at each point and attempting to integrate to the image.

The result of the consideration of numerous competing techniques [Wang,2002] was the selection of single frequency detectors distributed at seven specific locations across the visible band. The actual approach is a modified version of one developed by the compressive   sensing   community   [Baraniuk,2007,Unpublished][Baron,unpublished] [Brown,2000][Candes,2006]Donoho,2006][Gastpar,2003][Vetterli,2002] to reduce the number of detectors required to sense a given signal. In this case, it is envisioned that

only selected frequency information is required for the pixel locations contained in a two dimensional image. From this an effective chemical signature sort can be accomplished without resorting to the collection of computer clogging volumes of spectroscopic data. As a demonstration, consider the seven line (Bandwidth~1.5Å) filtered detectors represented in Figure 4-13. Though originally not random, the placement of these frequency sample points can be described by a Poisson statistical density with a "p" of 0.023 and a k=7. The resulting placement is described by a random variable and is sufficiently un-correlated to meet the requirements for compressive sensing.

As a test of this sensing modalities ability, this instrument was used to identify seven elements from a complex organics mixture containing macromolecules of biological interest. A double-blind series of experiments were undertaken to validate this sensors detection results against standard techniques such as GFAA (Graphite Furnace Atomic Absorption). The result was the determination of the seven elements of interest in the presence of extensive spectral noise from the organic macromolecules. Details of this work have been document in other publications and will not be repeated here. Of significance here is the demonstration of the effectiveness of the application of the compression sensing techniques to the determination of specific materials in the presence of significant spectral noise with out resorting to heroic data fusion efforts.

Thus the application of compressive sensing techniques to the identification of the chemical signatures of materials of interest designates only a few frequencies of interest that must be collected in a two dimensional image. This along with the subsequent post processing [Tropp,2003,2005]should allow a more effective material ID.
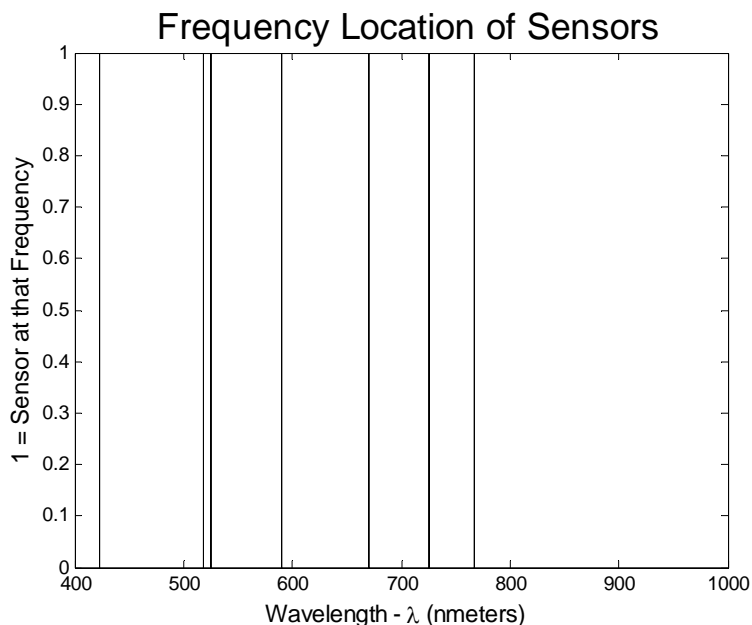

Figure 4-13 Poisson Distribution of Compressive Frequency Sensors

4.3.4 Conclusion

Publications and proposals in addition to those cited for year one are in process as a result of this contract. Follow-on research has been suggested by these results. Other sponsors have expressed interest in funding additional work. New interactions with a number of military sites and universities have been developed. Dr. Griffin would like to thank the sponsor for this opportunity.

Modeling of metals was affected by modification of the Boltzmann relaxation assumption and other effects to accommodate the transitional nature of the THz regime.

Modeling of plastics was affected by recognition of the dominate role of water in the plastic behavior, use of the modified water model and use of empirical water uptake data such as measured time constants.

Water was modeled utilizing extensively corrected variations on Debye's theory and absorption lines. Ice and snow were similarly modeled.

Human tissue was modeled by recognition of the dominant effect of the included water and ignoring the second order tissue structure effects.

Techniques to enhance THz target performance in imaging applications through unique procedures gave a number of promising results. In particular, a re-interpretation of clutter as it relates to THz imaging and water distribution suggests a relationship to spatial 1/f noise. A review of fundamental physical behaviors suggests a second order, noise-like water distribution described by the Helmholtz equation. Application of this to say people, suggests the convenient coordinates for separating the Helmholtz equation is Elliptical-Cylindrical coordinates. However, given the restricted field-of-view of THz imaging systems, it does not make sense to model the water distribution but to add ad hoc a spatial 1/f noise of the proper strength.

Finally, the application of compressive sensing techniques to spectral identification of materials in an image is promising.

Technical details of the results are published as itemized in section 4.4.

4.3.5 Future work

Performance modeling of FPA issues such as detector pitch, sensitive area, noise performance including post year one developments. Performance modeling of subsequent electronic processing will be considered.

Develop performance model for simulated images in the THz range including system resolution, system uniformity, environmental propagation,

Develop and revise performance model utilizing human studies on simulated images for comparison and validation.

Publications and additional proposals have been made and received as a result of this contract. Follow-on research has been suggested by these results. New interactions with ARL at White Sands, NVESD at Ft. Belvoir, RTTC at Redstone and ONR have been developed. Dr. Griffin would like to thank the sponsor for this opportunity.

4.4 Publications

4.4.1 Accepted/Published

E.L. Jacobs and S.T. Griffin, "Modeling and Characterization of Cloth at Sub-millimeter Wavelengths", Proceedings of SPIE Vol. 6549-03 Terahertz for Military and Security Applications V, April 2007.

S.R. Murrill, R.L. Espinola, C.C. Franck, F.C. De Lucia, D.T. Petkie, E.L. Jacobs, S.T. Griffin, and C.E. Halford, "Advanced Terahertz Imaging System Performance Model", Proceedings of SPIE Vol. 6549-01 Terahertz for Military and Security Applications V, April 2007.

C.C. Franck, R.L. Espinola, S.T. Griffin, E.L. Jacobs, S.R. Murrill, D. Lee, D.H. Tofsted, S. O'Brien, C.E. Halford, and J.P. Reynolds, "Terahertz Standoff Imaging Testbed Design and Performance for Concealed Weapon and Device Identification Model Development", Proceedings of SPIE Vol. 6549-07 Terahertz for Military and Security Applications V, April 2007.

S. T. Griffin, E. L. Jacobs, S. R. Murrill, "Reflectivity and Emissivity Modeling for Metals and Plastics at THz Frequencies", Proceedings of SPIE Vol. 6549-14 Terahertz for Military and Security Applications V, April 2007.

4.4.2 Planned

S.R. Murrill, B. Redman, R.L. Espinola, C.C. Franck, D.T. Petkie, F.C. De Lucia, E.L. Jacobs, S.T. Griffin, C.E. Halford, and J. Reynolds, "Advanced Terahertz Imaging System Performance Model for Concealed Weapon Identification", *Journal of Applied Optics*, under review, 2007.

S.R. Murrill, E.L. Jacobs, S.K. Moyer, C.E. Halford, S.T. Griffin, F.C. De Lucia, D.T. Petkie, and C.C. Franck, "Terahertz Imaging System Performance Model for Concealed Weapon Identification", *Journal of Applied Optics, under review, 2007.*

S.T. Griffin, E.L. Jacobs, S.R. Murrill, "Compressive Sensing Applied to Homeland Security", *IEEE Sensor Application Symposium*, under review, 2008.

S.T. Griffin, E.L. Jacobs, and S.R. Murrill, "Modeling Clutter Generated by Fabric at THz Frequencies", *SPIE Optical Engineering*, in preparation, 2008.

Griffin, S.T., "Incorporation of Antenna Non-Lambertian Angular Dependence into Optical Radiometric Models", *IEEE Transactions on MTT*, in preparation, 2008.

S.T. Griffin, C.E. Halford, and S.R. Murrill, "Modifications to Radiometric Performance Modeling for the THz", *SPIE Optical Engineering*, in preparation, 2008.

4.5 References

Total bibliography exceeds 300 entries and is available upon request.

R.G. Baraniuk, "Compressive Sensing", IEEE Signal Processing Magazine", vol. 24, pp.118-124, July 2007.

R.G. Baraniuk, M. Davenport, R. DeVore, and M. Wakin, "The Johnson-Lindenstrauss lemma meets compressed sensing", unpublished manuscript.

D. Baron, M. B. Wakin, M.F. Durate, S. Sarvotham, and R.G. Baraniuk, "Distributed compressed sensing", unpublished manuscript.

P. Bolivar, M. Brucherseifer, J. Rivas, R. Gonzalo, I. Ederra, A. Reynolds, M. Holker, and P. de Maagt, "Measurement of the Dielectric Constant and Loss Tangent of High Dielectric-Constant Materials at Terahertz Frequencies," *IEEE Trans. MTT*, 51, pp. 1062-1066, 2003.

R.P. Brown, *Handbook of Plastic Test Methods*, John Wiley and Sons, NewYork, 1988.
C. Vasile, *Handbook of Polyolefins*, Marcel Decker, New York, 2000.

E. J. Candes, J. Romberg, and T. Tao, "Robust uncertainty principles: exact signal reconstruction from highly incomplete frequency information", *IEEE Transactions on Information Theory*, vol.52, pp. 489-509, February 2006.

D.L. Donoho, "Compressed sensing", *IEEE Transaction on Information Theory*, vol. 52, pp.1289-1306, April 2006.

B. Donovan, *Elementary Theory of Metals*, pp. 215-255, Pergamon Press, Oxford, 1967.

M. Gastpar, B. Rimoldi, and M. Vetterli, "To code, or not to code: lossy source-channel communication revisited", *IEEE Transactions on Information Theory*, vol. 49, pp. 1147-1158, May 2003.

H.R. Simonds, A.J. Weith, and M.H. Bigelow, *Handbook of Plastics*, D. Van Nostrand Co., New York, 1949.

A. Tropp, A.C. Gilbert, and M. J. Strauss, "Simultaneous sparse approximation via greedy pusuit", *Proceedings IEEE International Conference on Acoustic Speech and Signal Processing*, pp. 721-724, 2005.

J.A. Tropp, A.C. Gilbert, S. Muthukrishnan, and M.J.Strauss, "Improved sparse approximation over quasiincoherent dictionaries", *Proceedings of 2003 International Conference on Image Processing*, pp.37-40, 2003.

C. Vasile, *Handbook of Polyolefins*, Marcel Decker, New York, 2000.

M. Vetterli, P. Marziliano, and T. Blu, "Sampling signals with finite rate of innovation", *IEEE Transaction on Signal Processing*, vol. 50, pp. 1417-1428, June 2002.

Y. Wang, J. Ostermann, and Y.Q. Zhang, *Video Processing and Communications*, Upper Saddle River, NJ: Prentice Hall, 2002, pp. 217-561.

5.0 Display Characterization and Digital Signal Processing Development (Dr. Aaron Robinson)

This report summarizes the advances made during the time period extending June 1, 2006 to May 31, 2007. It describes the research efforts undertaken in support of the stated milestones and the Center for Advanced Sensors (CAS) added focus on Intelligence, Surveillance and Reconnaissance (ISR) sensors.

> **Comment [t1]:** Carl, are these dates correct? TEW

5.1 Display Characterization

The characterization of one of the Barco LCD monitors at the Center for Advanced Sensors was completed during this quarter. The LCD characterization parameters were obtained using the MATLAB program and image set provided by Jeff Olson at the Army's Night Vision Electronic Sensor Directorate (NVESD). The same program and imagery were used to characterize the CAS's Barco CRT monitors. The results are recorded in Tables 5-1and 5-2.

Recall that for CRT monitors, the output luminance for a given input grayscale value can be determined with the following equation:

$$L_{out} = L_{min} + A \left(\frac{grayscale_{input}}{grayscale_{max}} \right)^{\gamma} \tag{5-1}$$

The MATLAB program and imagery were applied to obtain the values in Equation 5-1 for the LCD monitor characterization. Table 5-1 gives the best-fit values obtained for the five measured characterization parameters for one of the LCDs.

LUMINANCE EQUATION INPUT PARAMETERS					OUTPUT
A	V0	Gamma	L0	tau	RMS Error
28.21390693	130.066838	3.4744934	0.35658092	-0.0357121	0.0986244

Table 5-1 Barco LCD Monitor Characterization Parameters

Table 5-2 gives the best fit values obtained for the five measured characterization parameters for one of the Barco CRT's. This data was included in the report from the previous quarter. It is reproduced here to aid in comparison.

LUMINANCE EQUATION INPUT PARAMETERS					OUTPUT
A	V0	Gamma	L0	Tau	RMS Error
28.01597886	130.0741935	2.390327003	0.140059429	0.379037758	0.132559958

Table 5-2 Barco CRT Monitor Characterization Parameters

As expected, the luminance behaviors of the LCD and CRT monitors were distinctly different from exhibited by the well studied CRT monitors. This can be attributed to a number of factors. These factors include the differences in point spread functions for both monitors, the fact that brightness and contrast cannot be individually controlled on an LCD and the effects of the narrowed dynamic range of the LCD. These behaviors are reflected in Tables 5-1 and 5-2. Note that the minimum luminance values (L0) for LCDs is higher than that of the CRTs. The gamma and tau parameter values are also significantly different. The above issues would seem to imply that human performance characteristics on CRT monitors would be different than on LCD monitors. In order to effectively quantify those differences in ISR tasks and to further aid in the LCD characterizations, some perception experiments were planned.

5.2 Display Characterization Perception Experiment Development

Due to concerns of obtaining real world imagery representative of current ISR tasks, alternative perception experiment plans were developed based on character and shape identification. These applications were chosen because they closely resemble the ISR task of identifying a specific object in a cluttered scene. This is similar to the security and surveillance tasks of identifying a specific face in a crowd, identifying a specific car on a highway or determining if a person has a particular type of weapon.

This section describes the forced-choice experiments developed using characters and simple shapes. The subjects are shown one object from a known set and must identify that object. All of the images are computer-generated and therefore the need for a physical data collection is eliminated. A probability of correct ID (PID) distribution results from varying blur, object size, and noise.

In the event that real imagery can be obtained, new perception experiments will be designed to determine their effects.

5.2.1 Character Experiment

There were two character sets selected for use in the experiment. The sets are 2-3-5-E and 6-9-a-P. The characters are based on the Rochester Institute of Technology (RIT) character set; the RIT characters are equally recognizable at the limits of perception. The characters used here are thinner than the RIT characters to make the letters harder to identify when blurred. Contrast of the unblurred characters is 0.2.

61

Figure 5-1 illustrates character presentation to test subjects. One randomly selected character from the set 2-3-5-E is presented on the left, and one of the characters 6-9-a-P is presented on the right. The subject selects the appropriate button on the left to match the left character and the appropriate button on the right to match the right character. Clicking on the "next" button brings up the next two characters. The set 2,3,5,E is always presented on the left and the set 6,9,a,P on the right. A total of 96 character pairs are presented to each subject. Eight character pairs are presented at each of four ranges and three noise levels. Presentation of range, noise, and character are random.

Figure 5-1   Figure illustrates character presentation during subject testing. The subject sees one character from each set. The subject selects the appropriate button beneath the character.

Range (km)	Blur (see Eq. 17)	Noise (modulation)
1	20	0
2	15	0
3	11.7	0
4	10	0
1	10	0.025
2	10	0.025
3	8.3	0.025
4	7.5	0.025
1	10	0.05
2	7.5	0.05
3	6.7	0.05
4	7.5	0.05

Table 5-3 Blur and noise applied at each range in character experiment.

Range (km)	Noise modulation	Color display	Mono. display
1	0	0.98	0.97
2	0	0.42	0.83
3	0	0.12	0.47
4	0	0.03	0.42
1	0.025	1	1
2	0.025	0.69	0.69
3	0.025	0.5	0.5
4	0.025	0.14	0.14
1	0.05	1	1
2	0.05	0.75	0.75
3	0.05	0.11	0.11
4	0.05	0.08	0.08

Table 5-4 Measured PID for character experiment

5.2.2 Shape Experiment

The shapes presented in this experiment include a circle, a rotated-square with rounded edges, a hexagon, and an octagon. The hexagon and octagon have rotated and non-rotated versions. Each shape has an area of $24,450 \pm 50$ meters. The intrinsic contrast is 0.08.

Figure 5-2 illustrates the perception experiment interface used to accomplish the shape presentation. Just as in the character experiment, each presentation requires the subject to make two, independent discriminations. For the shape on the left, the subject sees two options at the bottom of the display; the subject also sees two options for the shape on the right. The subject clicks on the appropriate shape left and right and then clicks on the "next" button to bring up another set of shapes.
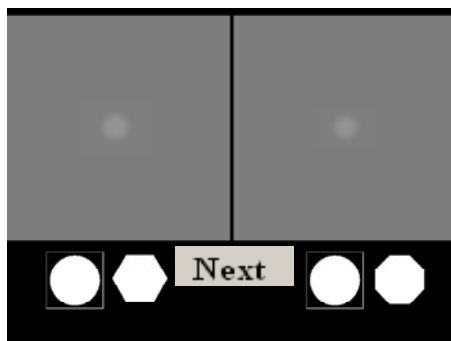

Figure 5-2: Shows the interface used to present the square, hexagon, octagon, and circle used in shape experiment

The experiment consists of 100 circle-hexagon and 100 circle-octagon discriminations with rotated and non-rotated shapes in equal number. There are 200 hexagon-octagon discriminations with all combinations of rotated and non-rotated shapes in equal number. There are 50 discriminations of rotated-square versus rotated-hexagon. The discriminations are divided equally among five ranges. Discriminations at each range include 20 circle-hexagons, 20 circle-octagons, 40 hexagon-octagons, and 10 rotated-square versus rotated-hexagon.

Range (km)	Blur 1 (see Eq. 17)	Blur 2 (see Eq. 17)
2	10	40
2.5	12.5	50
3	15	60
3.5	18.5	73.8
4	20	80

Table 5-5 Range and blur combinations for shape experiment.

Range (km)	Circle Octagon	Circle Hexagon	Octagon Hexagon	Square Hexagon
2	0.48	0.84	0.83	1
2.5	0.1	0.76	0.59	0.93
3	0.16	0.32	0.29	0.93
3.5	0.16	0.16	0.12	0.8
4	0.1	0.22	0.0	0.53

Table 5-6 Measured PID for shape experiment.

Circle-hexagon
◇ Data − − Model 1 —— Model 2

Figure 5-3 The figure shows PID (ordinate) and DRI model metric (abscissa) for discriminating circle and octagon. The diamonds are data and lines model predictions. The dashed line shows prediction using Ω50 giving best least-squares fit. The solid line shows prediction using a smaller

Figure 5-4 The figure shows PID (ordinate) and DRI model metric (abscissa) for discriminating circle and hexagon. The diamonds are data and lines model predictions. The dashed line shows prediction using Ω50 giving best least-squares fit. The solid line shows prediction using a smaller Ω50.
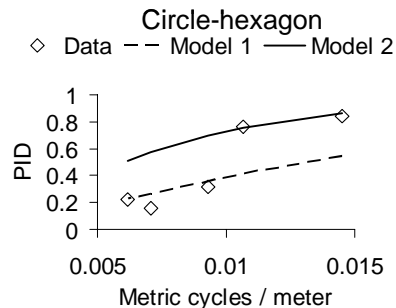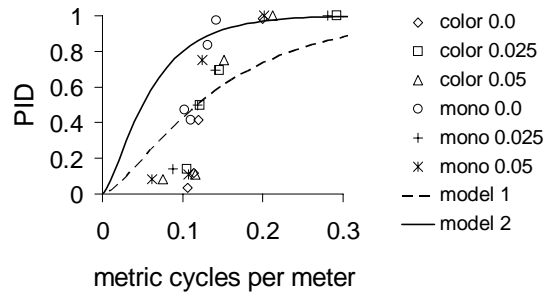

Figure 5-5 The figure shows PID (ordinate) and DRI model metric (abscissa) for discriminating circle and hexagon. The diamonds are data and lines model predictions. The dashed line shows prediction using Ω50 giving best least-squares fit. The solid line shows prediction using a smaller Ω50.
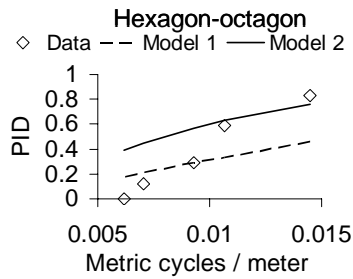
Figure 5-6 The figure shows PID (ordinate) and DRI model metric (abscissa) for discriminating hexagon and octagon. The diamonds are data and lines model predictions. The dashed line shows prediction using Ω50 giving best least-squares fit. The solid line shows prediction using a smaller Ω50.
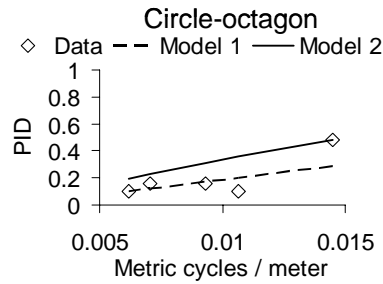
65
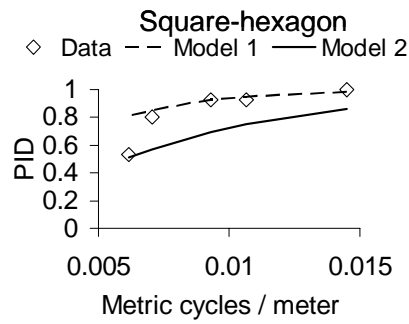
Figure 5-7 The figure shows PID (ordinate) and DRI model metric (abscissa) for discriminating square and hexagon. The diamonds are data and lines model predictions. The dashed line shows prediction using $\Omega 50$ giving best least-squares fit. The solid line shows prediction using a smaller $\Omega 50$.
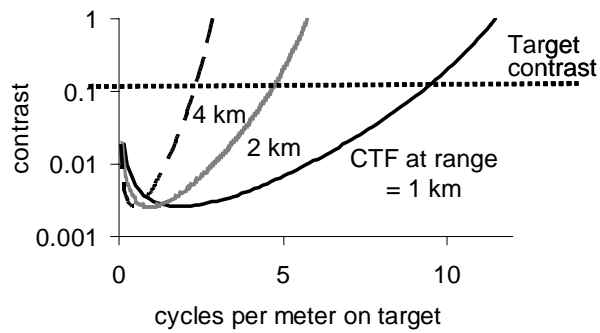

Figure 5-8 This figure illustrates the relationship between target-set contrast and CTF of the eye for the DRI model. Spatial frequency is in cycles per meter on target, not cycles per milliradian at the imager. Because the target set contains discrimination cues of all sizes, something is visible at all ranges. Probability of ID depends on imager resolution.

66
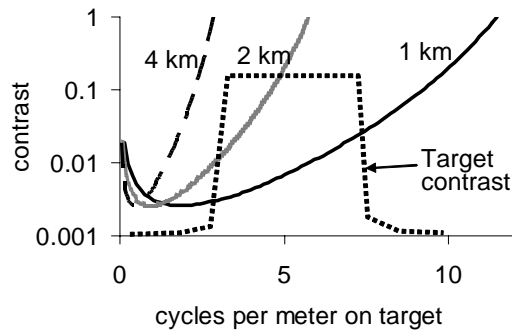
Figure 5-9 This figure illustrates that, for a specific target or a set of like targets, discrimination cues have a specific frequency spectrum. The imager must be able to resolve the specific cues. At some range, the available cues become blurred, and probability of ID drops to zero.
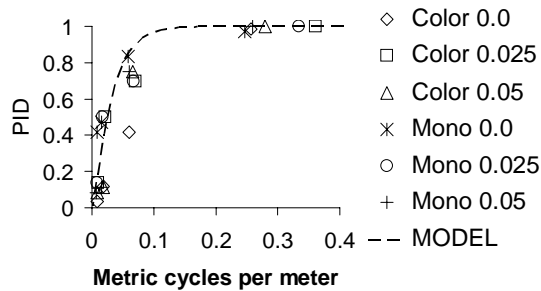
Figure 5-10 Figure shows PID (ordinate) versus metric using character FFT (abscissa). Data is shown for both color and monochromatic (mono) displays. The dashed curve is prediction using $\Omega50$ based on least-squares fit.
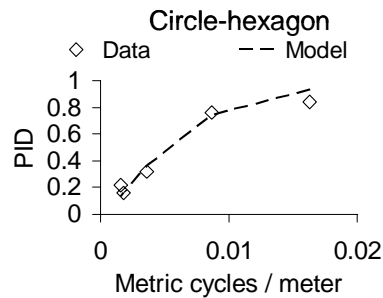
Figure 5-11 The figure shows PID (ordinate) and metric using FFT of circle (abscissa) for discriminating circle and hexagon. The diamonds are data. The dashed line shows prediction using $\Omega50$ giving best least-squares fit.
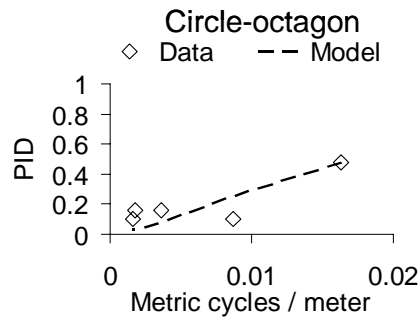
Figure 5-12 The figure shows PID (ordinate) and metric using FFT of circle (abscissa) for discriminating circle and octagon. The diamonds are data. The dashed line shows prediction using Ω50 giving best least-squares fit.
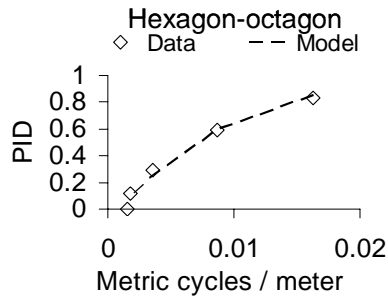
Figure 5-13 The figure shows PID (ordinate) and metric using FFT of hexagon (abscissa) for discriminating hexagon and octagon. The diamonds are data. The dashed line shows prediction using Ω50 giving best least-squares fit.
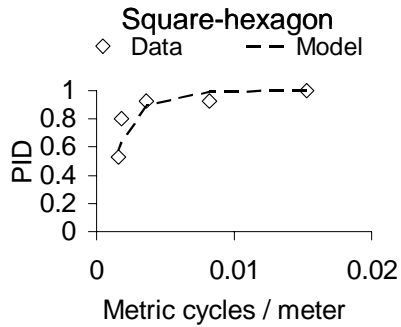
Figure 5-14 The figure shows PID (ordinate) and metric using FFT of square (abscissa) for discriminating square and hexagon. The diamonds are data. The dashed line shows prediction using Ω50 giving best least-squares fit.
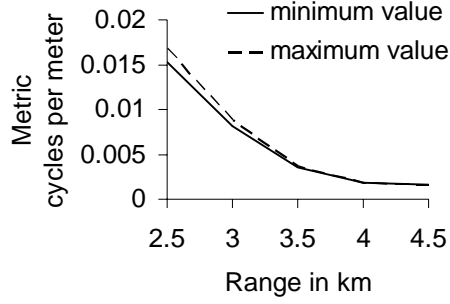
Figure 5-15 The FFT of circle, square, hexagon, or octagon is used to predict metric values. The figure shows the minimum and maximum metric values at each range.

5.2.3 Model Modifications to Predict Specific Object PID

Substituting the spatial frequency content of discrimination cues for C_{TGT} is impractical for many reasons. One major problem is defining which spatial attributes are important discrimination cues. Another problem is that small changes in scale due to range or orientation have little effect on target identification but have a significant effect on frequency spectrum.

A clue on how to proceed is taken from the DRI model itself. C_{TGT} is target-set contrast, not the contrast of discrimination cues. The assumption is that C_{TGT} reflects cue strength. Fortunately, understanding and quantifying discrimination cues is not necessary; an experimentally determined $\Omega 50$ quantifies task difficulty in the model.

The spatial frequency content of discrimination cues is bounded by the frequency content of the target itself; this constraint is introduced for C_{TGT}. For specific-object identification, $C_{TGT}(\xi, \eta, R_{ng})$ is the Fourier transform of the object in cycles per milliradian when the target is at range R_{ng}. Analyses in this paper use MATLAB Fast Fourier Transforms (FFT). Ω is now calculated using Equation 5-2, but the TTPF is still given by Equations 5-3 and 5-4.

$$\Omega = \left[\iint \delta \frac{FFT(\xi, \eta, R_{ng})}{\left[CTF_{sys}(\xi)\, CTF_{sys}(\eta) \right]^{1/2}} \frac{d\xi\, d\eta}{R_{ng}^2} \right]^{1/2} \tag{5-2}$$

$$\mathcal{PID} = \frac{\left(\Omega/\Omega 50 \right)^E}{1 + \left(\Omega/\Omega 50 \right)^E} \tag{5-3}$$

69

$$E = 1.51 + 0.24 \frac{\Omega}{\Omega 50} \qquad\qquad (5\text{-}4)$$

Figure 5-10 compares Equation 5-2 predictions to data from the character experiment. The character 6 FFT is used; the TTPF given by Equations 5-3 and 5-4 does not change. The PSQ is 0.96 with a $\Omega 50$ value of 0.025. Using the FFT of any character 2, 3, 5, E, 6, 9, a, or P yields the same results within four significant digits.

Figures 5-11 through 5-14 compare predictions from Equation 5-2 to data from the shape experiment. The FFT of circle, circle, octagon, and square are used for Figures 5-11 through 5-14, respectively. The $\Omega 50$ are 0.017, 0.005, 0.007, and 0.001 for Figures 5-11 through 5-14, respectively. For the shape experiment, predicted and experimental probabilities are highly correlated; the PSQ is 0.96.

The FFT of any experiment shape is used to predict performance. Metric values are calculated at each range using the FFT of circle, hexagon, octagon, and square. Figure 5-16 shows the minimum and maximum Ω values at each range. Metric variation is very small. If the objects are similar, use the FFT of any object in the group. If the objects are different, then the FFT of the object-of-interest is used.

5.2.4 Conclusions

Many military tasks involve locating and identifying specific objects. Traditional target acquisition models predict the average probability of identifying a set of diverse objects; these models predict hardware image quality using a set of targets as a quality standard. The DRI models do not predict specific-object identification.

The character and shape experiments described here illustrate the problem using DRI models to predict specific-object identification. DRI model predictions correlate poorly to experimental data. This is because the objects-of-interest are of certain size rather than of various sizes. The DRI model assumption that C_{TGT} is uniform at all spatial frequencies is incorrect for specific-object identification.

Introducing the Fourier transform of the object-of-interest into the DRI model corrects model predictions. Modified model predictions are highly correlated to experimental data.

Further, the necessary changes to predict specific-object identification are minor. Currently, radiometric imagery of the target set is collected in the field. The imagery is segmented to separate the target from local background. The value of C_{TGT} is calculated from the segmented imagery. To implement specific-target logic, superimpose the segmented target image on the average background level and take an FFT. The FFT is then used in the model in lieu of C_{TGT}.

One aspect of the model is more demanding than DRI model implementation. Much thought and user involvement is needed in choosing a confuser set to establish $\Omega 50$. The difficulty of finding and identifying an object depends on how much it looks like random articles in the scene. User involvement is required to establish target-of-interest; user involvement is also required to establish realistic clutter.

5.3 Perception Test for comparing the performance of LCD and CRT monitors

Liquid crystal display monitors and cathode-ray tube monitors use vastly different technologies. With their much smaller size and lower power consumption, LCD monitors are taking the place of CRT's in many applications. Many differences are known to exist in the performance resulting from the two different technologies. The LCD has a more rectangular point spread function, while the CRT produces a Gaussian spot. CRT's can function well at many different screen resolutions, while the LCD is limited by its discrete pixel size. CRT's are often capable of lower minimum luminances (darker blacks) than LCD's. The gammas of LCD's and CRT's are known to be different. The liquid crystal pixels of the LCD and the luminous phosphors of the CRT are both limited by different time-dependent transients. The contrast of an LCD can depend on the angle of observation, while the angle of observation has little effect on the contrast of imagery on a CRT. With so many differences present, a comparison of observer performance using LCD and CRT monitors should be made.

The University of Memphis has obtained a Barco Coronis LCD grayscale monitor and a Barco MGD521M CRT grayscale monitor for use in perception experiments. Both monitors have equal pixel densities (approximately 100 pixels per inch). Both monitors also have a 10 bit grayscale resolution. The monitors have different color temperatures, but this cannot be adjusted. They also have different gammas. Each monitor was adjusted to have the same minimum luminance (1.2 cd/m^2) and the same middle gray level luminance (25 cd/m^2).

Five observers participated in a number identification perception experiment. Observers were shown low contrast numbers between 0 and 9 on a mid gray level background. Five different font levels were used between 6 point and 14 point. No blur or noise was added. This was done so that the limiting MTF of the systems would be the monitor MTF. Observers were instructed to keep their heads about 18 inches from the screen (even with the edge of the desk), but they were not physically restrained. Each observer performed 200 trials on both the LCD and CRT monitors.

71

After completing the experiment, observers were asked which on which monitor the task was more easily performed. All agreed that the task was slightly easier on the LCD monitor. The results confirm this. The graph below shows the average probability of correct number identification as a function of the font size. Before the curves start to saturate a 6 to 8 percent difference in performance is measured between the curves.
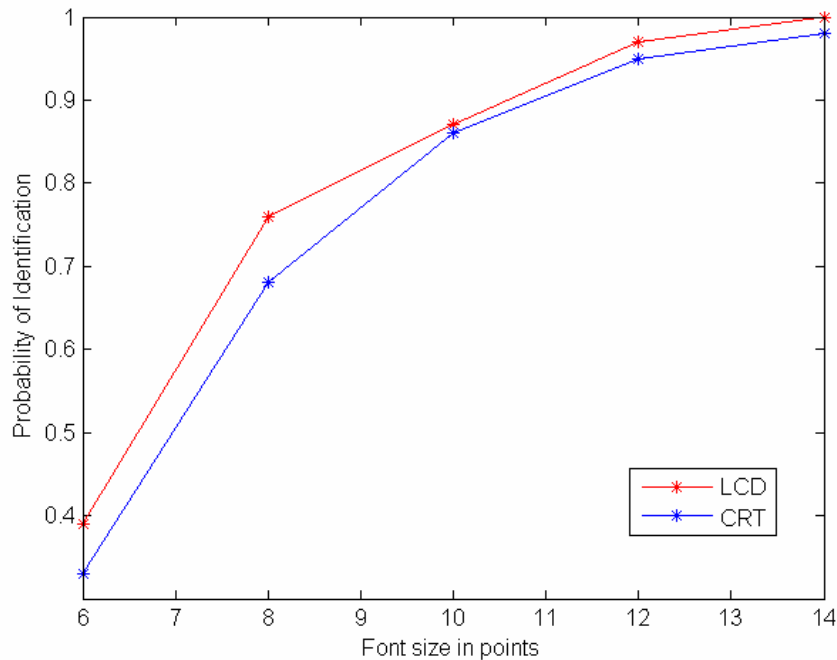
Figure 5-17 Perception test results

As can be seen in the graph, a modest improvement in performance is produced when the LCD is used. It should be noted that this test measures the effect of the different monitor MTF's on performance, but it does not measure the effects of some other differences between CRT's and LCD's. Static imagery was used, so none of the time related factors were measured. Also, the numbers had a single grayscale level against a middle grayscale level background, so monitor gamma did not have a significant effect. A perception test using diverse targets with flat grayscale histograms would be more appropriate to test the performance change due to gamma differences.

5.4 Intelligent Surveillance and Response Support

This section details the progress made in support of the Center for Advanced Sensors increased focus on Intelligence Surveillance and Reconnaissance. Specifically, the initial efforts to quantify the temporal and spatial resolution requirements for tracking human targets from low-to-mid altitude imagers began in the previous quarter of this year. The perception experiments and data analysis were completed during the time period covered by this quarterly report. The details of the research development and the results are summarized in the following sections

5.4.1 Simulated Target Detail

It was determined that simulation provided the most efficient and cost effective method of obtaining tracking scenarios that isolated the parameters under study. Therefore, the Army's Night Vision and Electronic Sensor Directorate's (NVESD) EOSim urban terrain simulation tool was used to generate all imagery. With the use of EOSim, the target's speed, starting point, destination, path and contrast were under the control of the researchers. Control was also provided over the imager's altitude, down-look angle, field of view, path and trajectory. The researchers were also able to control the ground sample distance represented in the imagery, the amount of clutter placed in the scene, the number of possible targets and the obscurants.

For the purposes of this research it was required that the system's resolution be sufficiently limited so that only a few display pixels represent the target. This prevented target identification and constrained the focus of the research to the tracking issue. Videos were then produced that showed the simulated target moving throughout the site on a frame by frame basis. Each video frame was a 640 x 480 pixel LWIR still image with white hot polarity. An example of the imagery is shown in Figure 5-18.
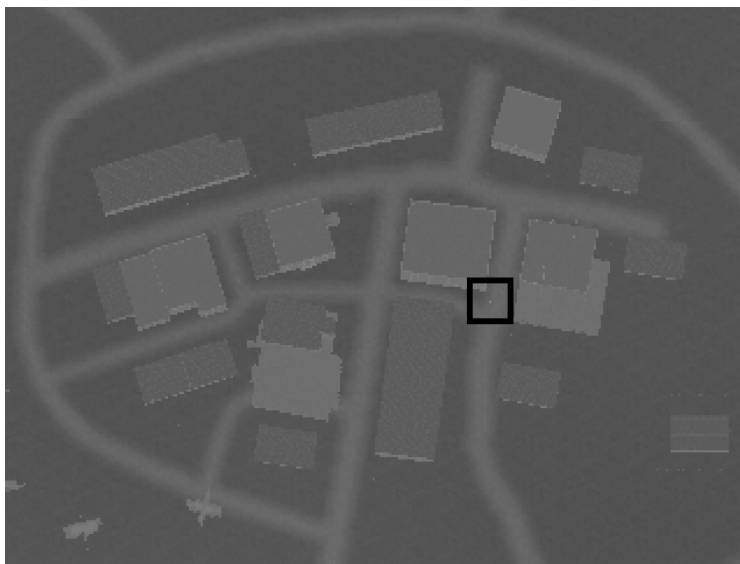
5.4.2 Perception Experiments

For the purposes of this research, the term tracking is used to refer to the act of following a target from a starting point to a destination. Success will be defined as correctly identifying the final destination of a specified target. A good example of a representative task could come from the non-real-time analysis of persistent surveillance video where it may be desirable to determine the starting point of a target in close proximity to some event of interest. Thus, the analyst would search the surveillance data in reverse and carefully take note of the targets position until the starting point is determined.

The target, its starting point, destination, target path and a unique set of operating conditions combine to create a distinct scenario. The blanket term "operating conditions" is used to represent the combination of a number of different variables. These variables include the contrast of the target, the target speed, the number of similar looking objects in the scene (or clutter), the band of the imager (LWIR, SWIR, Visible) etc. It was determined that 30 distinct scenarios were required to sufficiently represent the tracking task with respect to the variables under study.

5.4.3 Scenario Development

Extensive consideration of the problem led to the conclusion that anything beyond a trivial scenario (one target and little to no clutter) would make it difficult to extract useful and traceable cause and effect relationships. This was crucial to the initial development of this line of research and the subsequent follow on stages. Therefore, only one target at a time was tracked in these initial experiments, confusers were effectively removed, and clutter was provided by the environment itself i.e. roads.

Representative operating conditions were determined after consultation with NVESD personnel. The conditions chosen are as follows. The average marching speed of a soldier was estimated at approximately 1.5 m/s. The imager altitude was 2250 meters above the simulated environment. The number of possible destination buildings was set at 15 by the simulation site.

To prevent the introduction of multiple frame rates per scenario in each experiment, target movement was restricted to those sections of the site that were completely visible to the camera up until entrance into the destination building. The target would enter one destination building only. Upon entrance into that building, the target would not re-exit.

The set of ground sample distances tested were as follows: .5m, 1m, 2m and 4m. The corresponding frame rates tested were 8 fps, 4 fps, 1 fps, .25 fps, and .125 fps. The combined effect of these two variables on human performance was determined by completion of the following experimental matrix

Resolution	8 fps	4 fps	2.0 fps	1fps	.5 fps
4m	X	X	X	X	X
2.0 m	X	X	X	X	X
1 m	X	X	X	X	X
.5m	X	X	X	X	X

Table 5-7 Human Tracking Performance Experimental Matrix

Each cell in the experimental matrix represents a temporal and spatial resolution combination. There were 10 distinct scenarios assigned to each combination. The experiments were segmented according to spatial resolution or ground sample distance. Therefore, each row in the matrix represents a separate experiment.

5.4.4 Results and Conclusions

Intuitively, it was expected that there would be a direct correlation between smaller ground sample distances, higher frame rates and increased tracking performance. On the most basic level, the speed of the target directly influences the possible travel distance (or uncertainty) between frames and larger ground sample distances result in reduced imager capability in indicating the presence of the single human target. The collected data is shown in Table 5-8.

Corrected PCDD

Resolution	Frame Rate 8 fps	4 fps	1 fps	.25 fps	.125 fps
4 meter	0	0	0	0	0
2 meter	0.1	0.408	0.323	0.085	0.015
1 meter	0.985	1	0.985	0.754	0.538
.5 meter	0.977	0.992	0.977	0.838	0.508

Table 5-8 Table showing the corrected probability of tracking a target to the destination.

Table 5-8 shows the resultant probability that occurs when the Correct Destination Determination Ratio (CDDR) is corrected to remove the effects of guessing. This result will be defined as the *track probability*. It is calculated as follows:

$$\text{Corrected Track Probability} = \frac{\text{CDDR} - \text{P(guess)}}{1 - \text{P(guess)}} \qquad (5\text{-}5)$$

Where P(guess) is defined as the probability of guessing the correct destination purely by chance. For this research P(guess) = 1/15 to account for all destination buildings in the simulation site.

The Correct Destination Determination Ratio (CDDR) is calculated by

$$CDDR = \frac{\#\text{ of correct answers per combination}}{\#\text{ of scenarios per combination}} \qquad (5\text{-}6)$$

From the experimental results represented in Tables 5-4 through 5-7, we can conclude that the 4 meter and 2 meter ground sample distance are inappropriate for tracking humans under the conditions tested. The experimental results indicate that a 50 percent

corrected track probability is not reached for any combination of these ground sample distances and any frame rate under consideration.

A huge increase in tracking performance is evident as the imager resolution is increased from 2 meters to 1 meter. Specifically, track probabilities of greater than 50% were achieved for all frame rates tested. This is in direct contrast to the 2 meter results where 50% probability was not achieved. An approximate accuracy of 75% was realized at .25 fps and the result approach unity for frame rates of 1 fps and above. Similar results are observed in the .5 meter experiment. Thus, according to the data collected it can be concluded that 1 meter imager ground sample distance is sufficient for tracking a moving human target.

The development of the imager frame rate requirement was not as straightforward as that of the spatial resolution. This is due to the fact that temporal resolution system specification is an inherent function of target path and the characteristics of the terrain. Therefore, steps were taken to ensure that the *effects* of both were considered in this research and for future resolution developments. To accomplish this, an intermediate variable called the *track distance* was be used to encapsulate these characteristics. Specifically, it was used to indicate the uncertainty distance (maximum possible distance traveled between frames) that results in a 50% probability of a correct track.

The track distance for the simulation site was determined from examination of the collected data. From inspection of the data, the track probability drops to approximately 50% when the frame rate is decreased to .125 frames per second (1 frame every 8 seconds) for both the .5 and 1 meter resolutions. Note that the data from these resolutions were chosen because they both satisfy the tracking criteria established for the imager's spatial resolution. Thus, the *track distance* can be determined to be approximately 12 meters/frame. That track distance can now be used to calculate the frame rate required to maintain 50% tracking probabilities for other target velocities according to the following equation.

$$fps_{req} = \frac{V_r}{\text{track distance}} \qquad (5\text{-}7)$$

The results of these experiments have been written in journal format and submitted to the Journal of Optical Engineering.

5.5 References

1. Johnson, J., (1958), "Analysis of imaging forming systems," *Proceedings of the Image Intensifier Symposium,* October 6-7, 1958, AD220-160, U.S. Army Engineer Research and Development Lab, Fort Belvoir, VA, 249-273.

2. Howe, James (1993), "Electro-Optical Imaging System Performance Prediction," In Electro-Optical Systems Design, Analysis, and Testing, (Dudzik Ed.), The IR & EO systems Handbook, Vol 4, pg. 92, ERIM IIAC, Ann Arbor, MI and SPIE, Bellingham, WA.

3. Vollmerhausen, Richard H., Eddie Jacobs, and Ronald Driggers (2004), "New metric for predicting target acquisition performance, "OE, Vol.43, No.11, pp 2806-2818, November 2004.

4. Vollmerhausen, Richard H., Eddie Jacobs, Jon Hixson, and Mel Friedman, "The Targeting Task Performance (TTP) Metric; A New Model for Predicting Target Acquisition Performance," Tech Report AMSEL-NV-TR-230, NVESD, US Army CERDEC, Fort Belvoir, VA, March 2005.S

5. Vollmerhausen, Richard H., Eddie Jacobs, and Ronald Driggers (2003), "New metric for predicting target acquisition performance," Proc. SPIE Vol. 5076, *Infrared Imaging Systems: Design, Analysis, Modeling, and Testing XIV,* Gerald C. Holst; Ed.

6. Vollmerhausen, Richard H.; Driggers, Ronald G.; Tomkinson, Michelle, "Improved image quality metric for predicting tactical vehicle identification," *Proc. SPIE Vol. 4030,* p. 60-69*, Infrared Imaging Systems: Design, Analysis, Modeling, and Testing XI,* Gerald C. Holst; Ed. 07/2000.

7. O'Connor, John D., Patrick O'Shea, John E. Palmer, and Dawne M. Deaver, "Standard target sets for field sensor performance measurements," Proc. SPIE 6207, 62070U, 2006.

8. Moyer, Steve K., Eric Flug, Timothy C. Edwards, Keith A. Krapels, and John Scarbrough, "Identification of handheld objects for electro-optical/FLIR applications," Proc. SPIE 5407, pg 116, 2004.

9. Barten, P.G.J., (1999), *Contrast Sensitivity of the Human Eye and its Effects on Image Quality,* SPIE Press, Bellingham, WA.

10. Biberman, Lucien (Ed.), *Electro-Optical Imaging: System Performance and Modeling*, Chapter 12, SPIE Press, Bellingham, WA. and ONTAR Corp, N. Andover, MA, 2000.

11. Campbell, F.W., and J. G. Robson, "The Application of Fourier Analysis to the Visibility of Gratings," Journal of Physiology, 197, pp551-566, 1968.

12. Majaj, Najib J., Denis G. Pelli, Peri Kurshan, and Melanie Palomares, "The role of spatial frequency channels in letter identification," Vision Research, 42, pp 1165-1184, 2002.

13. Watson, A. B. & Pelli, D. G. (1983) QUEST: a Bayesian adaptive psychometric method. *Percept Psychophys, 33 (2),* 113-20.

14. *Instructions for the Use of the RIT Alphanumeric Resolution Test Object*, Graphic Arts Research Center, Institute of Technology, Rochester, N.Y., 1980.

15. R.H. Vollmerhausen, E.L. Jacobs, R.G. Driggers, "New Metric for Predicting Target Acquisition Performance*", Optical Engineering*, Vol. 33, Issue 11, pp. 2806-2818, Nov.. 2004

16. M. Self, D. Dixon, "Acquisition Level Definition and Observables for Human Targets, Urban Operations, and the Global War on Terrorism", Technical Report No: AMSRD-CER-NV-TR-235, March 2005

17. J.C. Leachtenauer, R.G. Driggers. *Surveillance and Reconnaissance Imaging Systems: Modeling and Performance Prediction*, Artech House Inc, Norwood MA, 2001

18. B.L. O'Kane, G.L. Page, "Predicting Detection of a Moving Target", Proceedings of Army Science Conference, Orlando FL, Dec 2002

19. O'Kane, B,L., Page, G.L. "Angular Distance Across the Eye as a Figure of Merit for detecting Moving Targets", Night Vision and Electronic Sensors Directorate Presentation

20. J.C. Leachtenaur, "The General Image Quality Equation", *Applied Optics,* November 1997, pp. 8322-8328

6.0 Performance Modeling of Sensors to Reduce Infrared Signatures

Period Covered 1 June 2006 to 31 May 2007 by Dr. Edward H. Perry

As intelligence, surveillance, and reconnaissance (ISR) systems take on large and larger roles in the field, it becomes more and more imperative to minimize the ability to detect American assets in combat zones. These assets include ground vehicles, aircraft, and various ground-based ISR imaging systems. Since all vehicles, aircraft, and ISR systems are powered, they generate heat and consequently present a potentially detectable thermal energy signature. Because the devices operate at temperatures close to that of the ambient environment, their thermal signatures lie almost completely in the infrared (IR) portion of the electromagnetic spectrum. By reducing the temperature and/or the IR emissivity of exposed surfaces, thermal signatures can be significantly reduced.

6.1 Methods to Reduce the Infrared Signature of Ground-Based Combat Assets Using Passive Methods.

6.1.1. Overview

This project's goal is to examine various methods for reducing the IR signatures of exposed surfaces employed on military assets to minimize the detection and recognition of these assets by infrared imaging systems. Methods to be addressed include those that lower the IR emissivity of the surfaces and those that lower the surface temperatures.

6.1.2. Activities to date

The work presented herein provides the foundation for development and testing of passive methods which aim to reduce the infrared signatures of various military assets. During the past year materials with a low IR emissivity were explored. One material, a low-emissivity tape available in the brown, green, and tan colors employed by the military for camouflage, was explored in detail. The tape, manufactured by OptiCorp, Inc., integrates a highly reflecting, low emissivity coating with a visual pigmentation layer such that the resulting material exhibits low emissivity in the infrared, while maintaining visual and near infrared reflectance characteristics consistent with conventional camouflage materials.

6.1.2.1 Experimental Measurements

A simple and reliable method was developed to measure the emissivity of surfaces. An experimental apparatus to implement this method was designed, constructed and validated. The experimental apparatus is comprised of four major components: an infrared thermometer (IRT), a heated plate assembly, a temperature controller, and thermocouple readout device as shown in Figure 6-1.

The heated plate assembly consists of a flexible silicone rubber heater, a one inch thick aluminum plate, and a test plate all in series. The assembly is held together with high temperature thermal conductive paste. Not only does the paste hold the plates and the heater together, it also helps maintain a uniform temperature.

79

The temperature of the plate was measured with nine thermocouples attached to the plate in a 3 x 3 grid pattern. This setup verified that the temperature across the plate was uniform and steady. The temperature was controlled with a thermocouple on the plate connected to the temperature controller. Once the desired temperature on the surface of the plate was reached, the heater cycled on/off to maintain the specified temperature input.
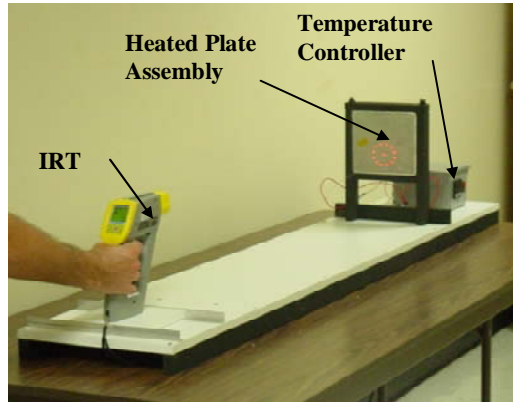
Fig. 6-1. Depiction of experimental procedure used to measure emissivity.

By adjusting the emissivity setting on the IRT until the latter indicated the same temperature as the thermocouple array, the emissivity of the heated surface was determined. Excellent agreement was found between measured values and those reported in the literature for a number of surfaces.

To measure the effectiveness of using low-emissivity surfaces, the experimental apparatus described above was employed. A 15 cm square aluminum plate was first painted with flat-black paint. Then a "woodland" camouflage pattern was generated using the low-emissivity tape discussed earlier for the brown, green, and tan colors. This plate is shown in Figure 6-2.

Thermocouples were attached to the plate in regions representing each of the four colors. The plate was heated to 300 K, 325K, and 350 K, and LWIR images were obtained using a FLIR Systems ThermoVision® A40M infrared camera.

Two of the images obtained are shown in Figure 6-3 for plate temperatures of 325 K and 350 K. Only the black-painted areas, which appear white in the image, produce much luminance. The green, brown, and tan areas all display low luminance levels as would be expected for such low-emissivity surfaces.

Clearly the thermal signature of an asset covered with such an IR camouflage

Figure 6-2 Aluminum plate with woodland camouflage pattern formed with flat black paint and low-emissivity tape.

pattern would be much lower than the signature of the same asset painted with standard high-emissivity paint.
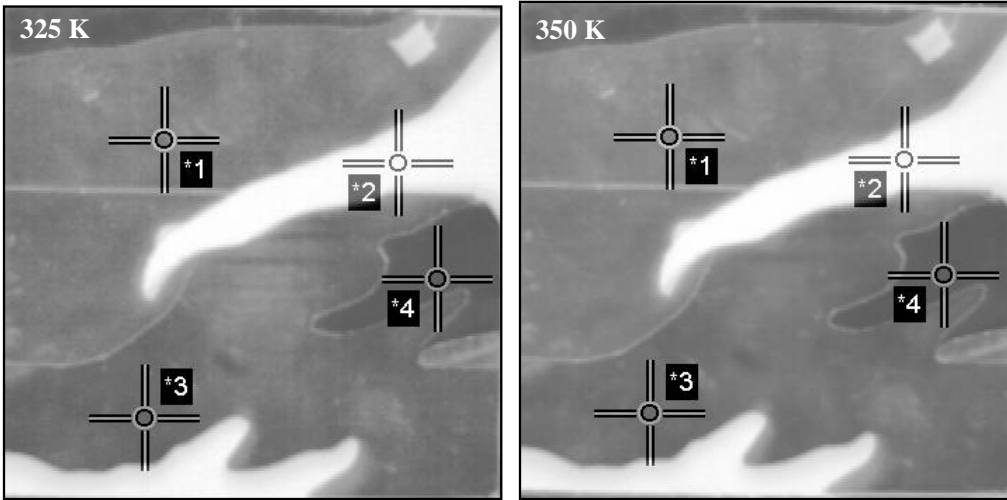
Figure 6-3 Thermal images (LWIR) of test plate at 325 K and 350K. Low-emissivity tape was used to cover all areas except the black (appearing as white in the images).

6.2 Modeling the Effectiveness of Signature-Reduction Applications in the Infrared

6.2.1. Overview

Mathematical models were developed for the following two strategies that can be employed to reduce thermal signatures:

   1) employ surfaces with low IR emissivities
   2) employed extended surfaces to reduce surface temperatures

The ultimate objective is to demonstrate the effectiveness of various signature-reduction techniques by synthesizing thermal images of assets employing these techniques alongside images of the same asset without thermal signature-reduction.

6.2.2. Activity to Date

From the well known Planck distribution law (Incropera & DeWitt, 1996) the rate at which a unit area of a perfectly black surface emits radiant energy per unit wavelength (spectral emissive power) is given by

$$E_{\lambda,b} = \frac{C_1}{\lambda^5 (e^{C_2/\lambda T} - 1)}$$

[6.1]

where $C_1 = 3.74 \times 10^8$ W·μm^4/m^2 and $C_2 = 1.44 \times 10^4$ μm·K. For a non-black surface, the emissive power at a given wavelength is given by a similar expression

[6-2]

$$E_{\lambda} = \frac{\varepsilon_{\lambda} C_1}{\lambda^5 (e^{C_2/\lambda T} - 1)}$$

81

where ε_λ is the "spectral hemispherical emissivity" of the surface. The emissivity is a measure of a surface's ability to emit thermal radiation compared to the ideal emitter, which is a blackbody. Thus, $0 \le \varepsilon_\lambda \le 1$ for all surfaces, and for most surfaces the emissivity varies with wavelength. In Fig 6-4 the emitted radiant energy for a blackbody at 300 K is shown along with that and for a non-black surface at 325 K with a "selective" emissivity given by

$\quad\quad \varepsilon_\lambda = 1$ for $\lambda < 3\ \mu$ and
$\quad\quad \varepsilon_\lambda = 0.685$ for $\lambda \ge 3\ \mu$.

Clearly, the spectral characteristics of the two surfaces are very similar. The total energy in the 8-12 μ wavelength range (LWIR) is within 1% for the two surfaces. Thus, this "selective" non-black surface at 325 K would appear very similar to a "black" background at 300K in an MWIR or an LWIR imaging system.
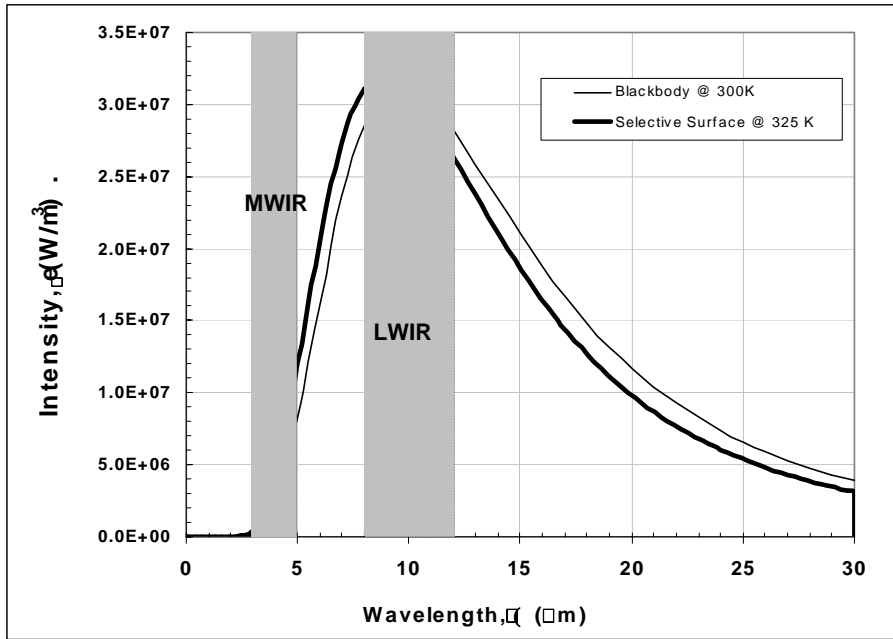
Fig 6-4 Comparison of the radiant energy emitted by a black surface at 300K and a selective surface ($\varepsilon_\lambda = 0.685$ for $\lambda > 3\mu m$) at 325 K.

A simple way to reduce the temperature of a surface is to use extended surfaces, or fins, attached to the surface as shown in Fig. 6-5. This can be demonstrated easily by considering the following relation, which describes the heat transfer $\dot{Q}$ from a surface to its surroundings by both convection and radiation:

$$\dot{Q} = A_s \left\{ h(T_s - T_a) + \sigma \varepsilon_s (T_s^4 - T_a^4) \right\} \quad\quad\quad \text{[6-3]}$$

where A_s is the surface area, T_s the surface temperature, T_a the ambient temperature, h the convective heat transfer coefficient, σ the Stefan-Boltzmann constant, and ε_s the IR emissivity of the surface.
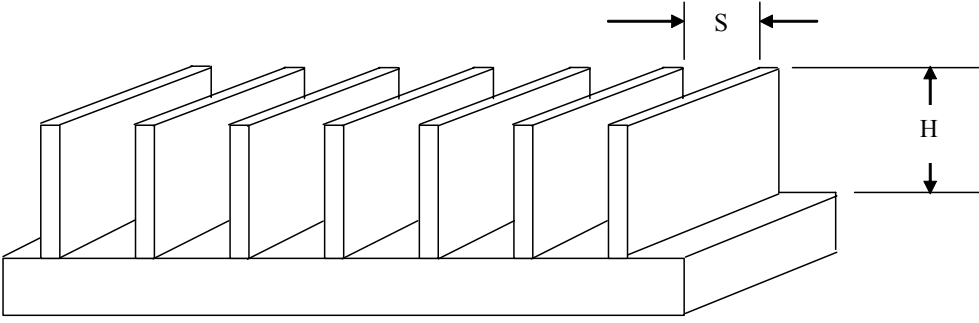
Figure 6-5 A 7-fin array with fin height H and fin spacing S

Often Eq. 6-3 is written simply as

$$\dot{Q} = A_s\, \tilde{h}\, (T_s - T_a) \qquad\qquad [6\text{-}4]$$

where $\tilde{h}$ is the "overall" heat transfer coefficient (convective and radiative) defined as

$$\tilde{h} \equiv h + \frac{\sigma \varepsilon_s (T_s^4 - T_a^4)}{T_s - T_a} = h + \sigma \varepsilon_s (T_s^2 + T_a^2)(T_s + T_a) \qquad\qquad [6\text{-}5]$$

Rearranging Eq. 6-4, we find

$$T_s = T_a + \frac{\dot{Q}}{\tilde{h}\, A_s} \qquad\qquad [6\text{-}6]$$

Clearly, for a given heat transfer rate $\dot{Q}$, the temperature of the finned surface decreases with increasing surface area, provided the heat transfer coefficient remains unchanged. However, Rao et al. [2006] have shown that this coefficient depends on a number of parameters, including the fin spacing S and fin height H:

$$\tilde{h} = 0.102 \frac{S}{k_f} Ra^{0.36} \left(\frac{S}{H}\right)^{0.4} \left(\frac{1+\varepsilon_1}{1+N_R}\right)^{0.1} N^{-0.04} \qquad\qquad [6\text{-}7]$$

where k_f is the thermal conductivity of the air, ε_1 the IR emissivity of the fin, and N the number of fins. N_R accounts for radiative heat loss from the fins, and Ra is the Rayleigh number associated with the natural convection from the fins. These two non-dimensional parameters are defined as

83

$$N_R = \frac{\sigma T_{air}^4}{k_f \, (T_{fin} - T_{air})} \frac{1}{Gr^{1/4}} \qquad\qquad Ra = \frac{g \, \beta \, (T_{fin} - T_{air}) \, S^3}{v_w \, \alpha_w}$$

where σ is the Stefan-Boltzmann coefficient, g the gravitational acceleration, β the thermal expansion coefficient of the air, v_f the viscosity coefficient of the air, α_w the thermal diffusivity of the air at the fin temperature, and Gr is the Grashof number defined as $Gr = Ra \; \alpha_w / v_f$.

From Eq. 6-7 it is readily apparent that the heat transfer coefficient decreases with decreasing fin spacing and with increasing fin height. This occurs because the thermal boundary layers on adjacent fins, which increase in thickness along the vertical dimension of the fin, overlap at small fin spacings and large fin heights, resulting in interference between the two fins.

Analyses were performed for arrays of rectangular fins attached to a heated 15 cm square horizontal surface that must transfer 10.7 W (444 W/m^2) to an environment at 300 K. It was assumed that both the plate and fins were nearly thermally black (i.e. $\varepsilon_\lambda = 0.90$). Fin heights of 25, 38, 51, and 76 mm were considered along with fin spacings ranging from 1mm to 27 mm.

Figure 6-6 shows the results obtained for steel fins (k = 57 W/m-K). First, it is readily apparent that the average temperature of the finned array is considerably less than the temperature required by the plate alone (350 K) to transfer the same amount of heat from the plate. Also, an optimum is observed at around 25 fins, corresponding to a fin spacing of about 3 mm. This occurs because of the interference between adjacent fins discussed above. Above about 25 fins the gains obtained by larger surface areas are offset by reductions in the heat transfer coefficient.
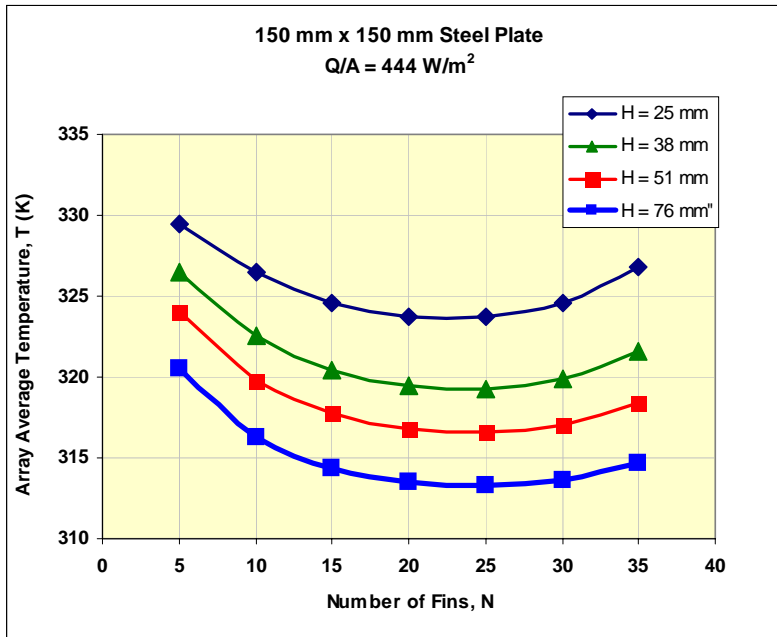
Figure 6-6 Fin Array Average Temperature as a function of the Number of Fins Attached

From a thermal signature reduction perspective, temperatures are vitally important since the emittance of a surface varies as the fourth power of the surface temperature. Figure 6-7 shows a simulated LWIR image of an array employing steel fins. Black represents a temperature of 300 K and white a temperature of 350 K. The thermal signature presented by this array is clearly lower than it would be for the plate alone.
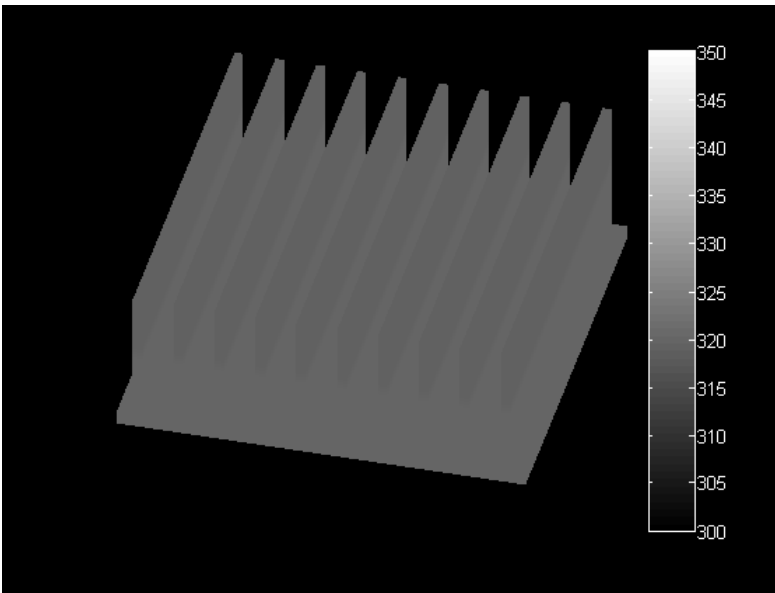
Figure 6-7   Simulated LWIR image of a 10-fin array employing 51-mm high fins. Mean temperature of the array is 320 K

6.2.3 References

Incropera, F.P &DeWitt, D.P. (1996), *Fundamentals of Heat and Mass Transfer, Fourth Ed.*, John Wiley & Sons, New York.

Rao, V., Naidu, S. V., Rao, B., & Sharma, K. V. (2006). Heat transfer from a horizontal fin array by natural convection and radiation—A conjugate analysis. *International Journal of Heat and Mass Transfer*, 49, 3379–3391.

6.3   Performance Modeling of Persistent ISR Imaging Systems in Adverse Environments

6.3.1. Overview

This research centers on modeling the performance of persistent ISR imaging systems in adverse environments such as those present in secure enclosures in the hot desert where temperatures in excess of 120 ^oF can be expected and those present for air-borne imaging systems at altitudes of 25,000 to 50,000 feet, where temperatures ranging from -30 ^oF to -70 ^oF are normal.

6.3.2 Activities to Date

In a hot, dry desert environment the relative humidity of the ambient air is quite low, typically below 10% in the afternoon. The temperature of the air can be reduced considerably by spraying water into the air, the principle behind "swamp coolers." This process, known as adiabatic saturation or evaporative cooling, can reduce the air temperature by 15-25 Kelvins (30 - 40 ^oF), thus making the air much more suitable for cooling temperature-sensitive electronic equipment. Theoretically, an evaporative cooler can bring the air temperature down to the "wet-bulb" temperature of the air.

A typical evaporative cooler is shown in Fig. 6-8. Hot, dry outdoor air is drawn through pads which are saturated with water. Water evaporates from the pads and humidifies the air. The heat required for the evaporation is drawn from the incoming air, causing it to cool. The air exiting the unit can be used to cool electronic equipment.

The efficiency ε of an evaporative cooling system is defined as:

$$\varepsilon \equiv \frac{T_{DB,in} - T_{DB,out}}{T_{DB,in} - T_{WB,in}} \qquad\qquad [6\text{-}8]$$

where T_{DB} is the "dry-bulb" temperature of the air and T_{WB} is the "wet-bulb" temperature. The wet-bulb temperature is the lowest possible temperature that can be reached by an evaporative cooling unit. Evaporative cooling units typically exhibit efficiencies on the order of 85%. Rearranging Eq. 6-8, we find that the temperature $T_{DB,out}$ of the air leaving an evaporative cooler is:

$$[6\text{-}9]$$

$$T_{DB,out} = T_{DB,in} - \varepsilon(T_{DB,in} - T_{WB,in})$$
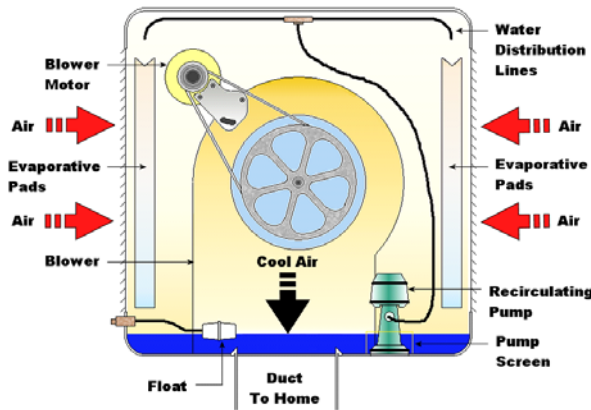
Figure 6-8   Typical configuration of an evaporative cooler

Figure 6-9 shows the exiting dry-bulb temperature as a function of the relative humidity of the incoming air, which is assumed to be at a temperature of 317 K (110 F). For 10% incoming relative humidity, a leaving temperature of 297 K (75 F) is predicted for a cooler with an efficiency of 85%, a drop of 20 Kelvins (35 °F).

Although evaporative cooling units do require a supply of water, a scare commodity in most desert environments, the water requirements are modest. For example, 1 kg of water can cool 90 kg of air (approximately 80 cubic meters) by 20 Kelvins, the equivalent of 1.6 million Joules. Thus, an evaporative cooling unit dissipating 500 W of heat from an electronics system in a 317 K environment (110 F) would require approximately one liter of water per hour while allowing the equipment to operate at a temperature that is 20 Kelvins cooler.
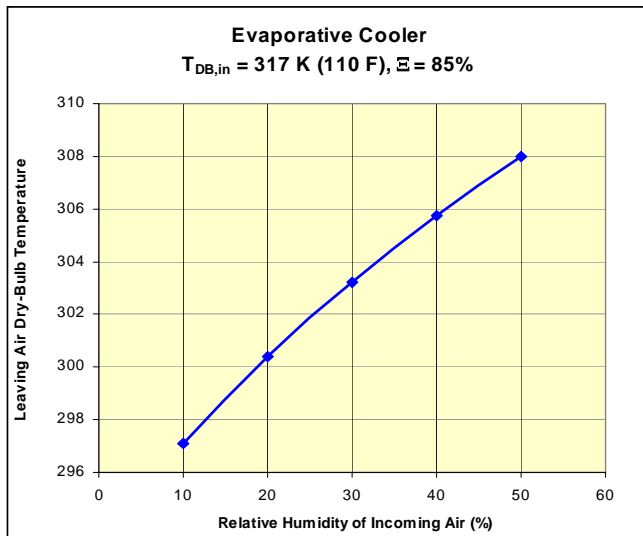
Figure 6-9 Cooling performance of an 85% efficient evaporative cooling system operating at various inlet humidity levels

7.0 Final Report for Center for Advanced Sensors - Vanderbilt University

Period Covered, 1 April 2005 to 31 Oct. 2007, US Army Contract W911NF-05-2-0019, By Profs. J. L. Davidson, A. B. Bonds, W. P. Kang

7.1 Administrative

The Vanderbilt Program in support of the Center for Advanced Sensors was completed on schedule and spend plan. Figure 7.1-1 below summarizes the projects engaged by Vanderbilt in support of the CAS program. As the funding level was reduced for the Vanderbilt subtask in Year 2, the task re: "Bio-Optic Sensor Electrode Development" took a diminished role and certain other tasks were reduced. The discussion and figures that follow are results for the program portion of the Vanderbilt tasks. Some of this information was presented in previous interim reports and is collected here for this report. As Year 2 came to a close and the Vanderbilt funds were terminated, this is the final report.

Center for Advanced Sensors

Davidson/Bonds   Vanderbilt University

> **Bio-Optics of Vision**

> **Bio-Optic Sensor Electrode Development**

> **IR Display Development**

Figure 7.1 - 1 Summary of projects engaged by Vanderbilt in support of the CAS program

7.2 Bio-Optics of Vision – Professor A.B. Bonds

7.2.1 Overview

Positioning of Vanderbilt's biological vision initiative to ARL-NV goals

Our work is directed at identifying mechanisms used by the brain for object segregation. A principal symbiosis appears to be in the area of *search*. Strategies used by the brain in segmenting salient visual structures from background clutter may prove useful in improving classification across large numbers of images. These strategies may also be

applied to enhance human performance in direct recognition tasks. The importance of testing these results via integration with modeling is noted.

7.2.2 Objective

Research natural (living organism) visual sensory representation as performed by neural assemblies, recording isolated neural activity across a network of cells. Determine the coding of visual signals by cell populations and achieve a working view of the neural code to achieve superior electronic approaches to rapid AI night vision image signal processing. Our fundamental hypothesis is that global structure is synthesized in the brain by the dynamic formation of cellular assemblies identified by firing that is synchronous on a msec scale, the Binding By Synchrony (BBS) model. Testing and analyses are directed toward validation of this hypothesis. The first section (7.2.3.1-7.2.3.5) analyzes the general characteristics of firing synchrony and the second section (7.2.3.6-7.2.3.9) explores the relationship between synchrony and contour detection. These topics engage multiple disciplines, including (1) visual neuroscience, (2) imaging, processing and detection, (3) automated decision making/classification and (4) statistical analysis.

7.2.3 Results

7.2.3.1 Frequency of occurrence of synchronous groups

The importance of cellular assemblies defined by synchrony in the process of object cognition is dependent on how often such assemblies arise in the process of normal vision. A high frequency of occurrence would suggest that the mechanism is fundamental to brain function. We presented 4500 natural images, including 250 images, each rotated at 18 angles (20° to 360°, in 20° increments). Each image subtended 20° x 20° and was jittered, star fashion, at 60 Hz for 0.5 sec. The images were displayed in a random order followed by 0.5 s of mean luminance. The entire sequence was shown 10 times (in different random orders) and pictures were scaled to have the same global contrast. Fifty groups each of 2-8 cells were selected at random for analysis, with some preference for groups covering large areas in space. Group responses were quantified, averaged across all 10 trials, weighted by their scores, and summed to produce a composite of the average response. We have found that any arbitrary group of 8 cells or less will reliably synchronize to some of the 4500 images (Figure 7.2-1), and some groups of 9-10 cells will repeatedly synchronize to a few (e.g., 5/4500) particularly complex images. While the fraction of stimuli that drive an assembly drops as assembly size grows, this is a natural consequence of increased selectivity of the higher order assemblies to more complex visual features (see below). The number of potential assemblies grows geometrically with assembly size, markedly increasing the likelihood that any image will trigger the formation of at least one, and more probably several, assemblies.
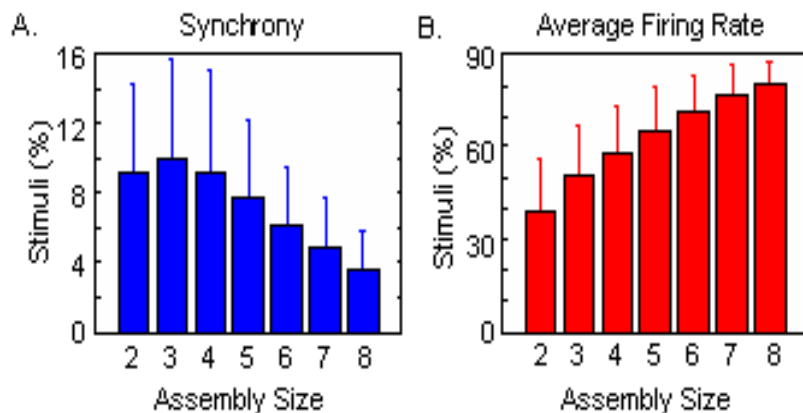
Figure 7.2 - 1 Average fraction of 4500 stimuli that produce responses greater than 1.96(stdev) above chance as a function of assembly size for synchrony (A) and firing rate (B).

7.2.3.2 Selectivity of cellular assemblies.

In a pilot experiment, we measured the kurtosis and population and lifetime sparseness of synchrony and firing rate response distributions of a set of cells viewing a natural image sequence for the purpose of establishing the degree of selectivity of particular assemblies. Three hundred fifty (350) assemblies were chosen randomly for analysis with 50 assemblies per size group (2-8 cells). Fig 7.2-2 plots the synchrony (or firing rate) normalized to a maximum of 1 against the probability of that value of synchrony (or firing rate) across all natural image presentations. The results show that synchrony response distributions were highly leptokurtic (selective with only a few images generating high responses in the right tail of the distribution) and kurtosis increased nearly exponentially with group size. This means that for successively larger assemblies, there were fewer and fewer images that generated large responses. On the other hand, the kurtosis for average firing rate response distributions decreased slightly across assembly size. This suggests that increasing the assembly size enhances the ability of synchronous assemblies to discriminate among the natural image sequence while it hinders the selectivity for a firing rate code, which becomes highly redundant and confounding. *Note that the assembly in the image with the largest synchrony response from Figure 7.2-2 tends to lie on a single complex contour, suggesting that cellular assemblies are important in the process of contour integration. This finding is explored further in 7.2.3.7*

Population and lifetime sparseness were computed using the Rolls & Tovee (7.4-31) measure as modified by Willmore & Tolhurst (7.4-45). For a single assembly size (Figure 7.2-3), synchrony responses are much sparser than firing rate responses and this difference increases when assembly size grows. This means that for our stimulus set, assemblies of 2-8 cells exhibited high population sparseness, where only a small number of groups out of 50 (per assembly size) responded strongly to a single image, and high lifetime sparseness, where each assembly only responded strongly to a few images out of the set of all images (4500). Firing rate responses became less sparse as each new

member contributed more images to the response set. The firing rate results are expected to change when requiring assembly members to fire above a threshold, but preliminary analyses show that they will still be significantly less sparse than synchrony responses. Overall this suggests that image structure is fundamentally coded by the identity of the particular members of the synchronous assemblies rather than the relative activities across the population as a whole. A more detailed investigation of sparse coding deriving from these pilot observations is found in 7.2.3.9.
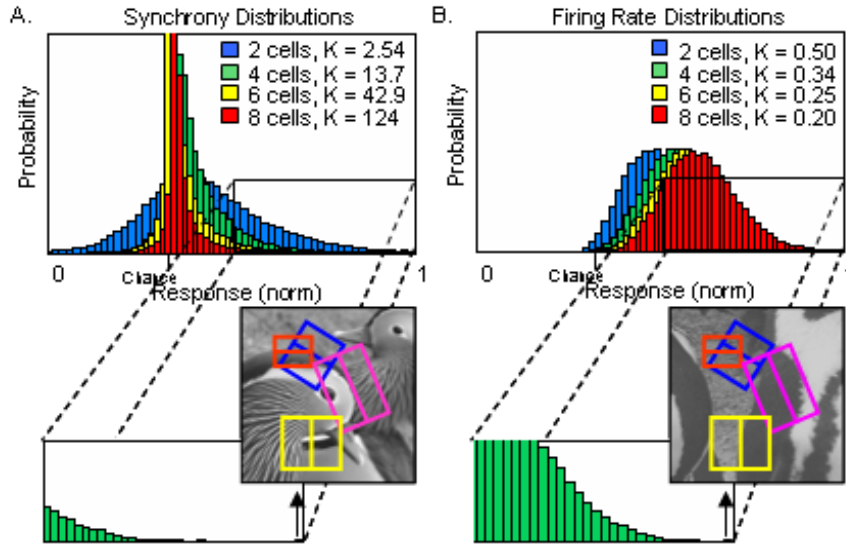
Figure 7.2 - 2 (A) Sample synchrony and (B) average firing rate response distributions for assemblies of 2, 4, 6, and 8 cells. The kurtosis of the synchrony distributions increases nearly exponentially with assembly size (the red and yellow bars extend beyond this figure, which was cropped to show the range of responses). The green bars show the detailed distribution of the highest responses for a group of four cells, and the insets show the images with the largest synchrony and firing rate for the same assembly of 4 neurons.
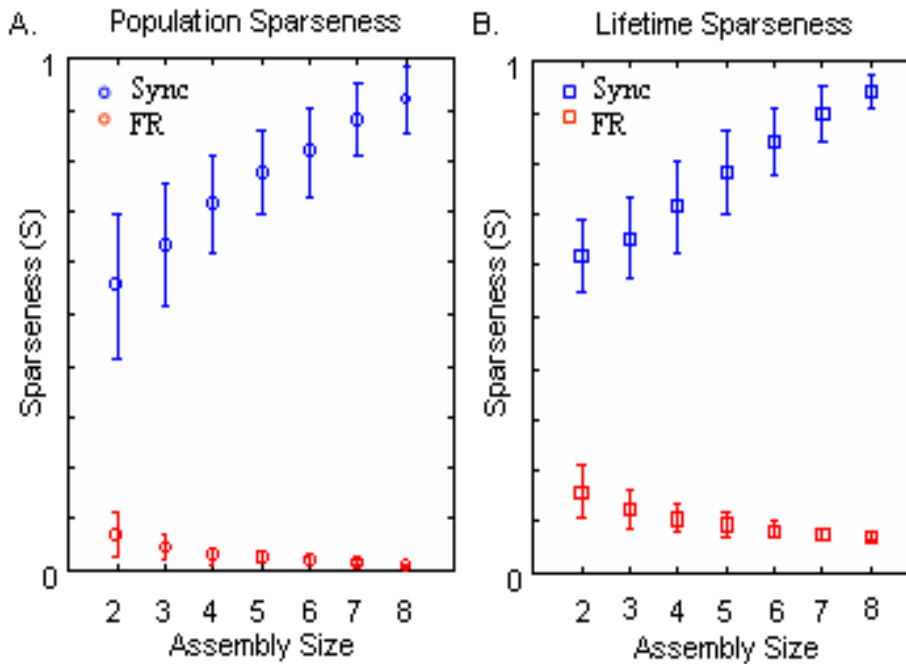
Figure 7.2 - 3 (A) Population sparseness as a function of assembly size. Population sparseness describes the response distribution of many assemblies to one image. (B) Lifetime sparseness as a function of assembly size. Lifetime sparseness describes the response distribution of one assembly to many images.

7.2.3.3 Reliability of cross-correlation measures

In the course of presenting our results and publishing, we have confronted a good deal of concern regarding the primary method by which we quantify neural interactions (the Joint Post-Stimulus Time Histogram (JPSTH) of Aertsen, et al, 1989, 7.4-2). There is considerable debate on the problem of quantifying synchrony because of many influences on firing patterns. Our conclusions depend on reliable estimates of stimulus-dependent changes in the correlation magnitude, and we must prove that these changes represent true changes in effective connectivity. There are two main issues: (1) How changes in average firing rate are normalized and (2) How nonstationary firing patterns are interpreted.

Normalization. The basic criticism of the JPSTH method of Aertsen et al (1989, 7.4-2) is that it was calibrated empirically at lower firing rates. For the positive correlations that we study interaction is well-approximated by the normalized correlation coefficient until the probability of a spike per bin (ρ) exceeds about 0.3 (Ito & Tsuji (2000), 7.4-22), their Fig 4). We record from a large group, so any given stimulus is suboptimal for most cells and firing rates are lower than found with stimuli artificially tailored to single units. Across a sample of 111 cells, fewer than 1% of total spikes had a ρ >0.3 (see Methods for details), suggesting that for nearly all of our data the strategy for firing rate normalization

94

is not misleading. There are three common methods for normalization: (1) The JPSTH uses the geometric mean of the autocorrelations. (2) Bair et al (2001), (7.4-5), and Kohn & Smith (2005), (7.4-24), combine the shift predictor method and the geometric mean of the firing rates. (3) The NCC (Neural Correlation Coefficient: Abeles (1982), (7.4-1); Eggermont (1992), (7.4-12); Hirabayashi & Miyashita (2005), (7.4-19) uses the shift predictor and the geometric mean of the autocorrelations. All are conceptually similar and result in nearly identical quantities and behavior under a diverse range of conditions (static and dynamic stimuli; anesthetized and awake animals; cat and monkey; A1, V1, MT, and IT). Normalization based on the product of the firing rates is generally less effective (Bair et al. 2001, 7.4-5). Fig.7.2-4 shows the relative consistency of the three
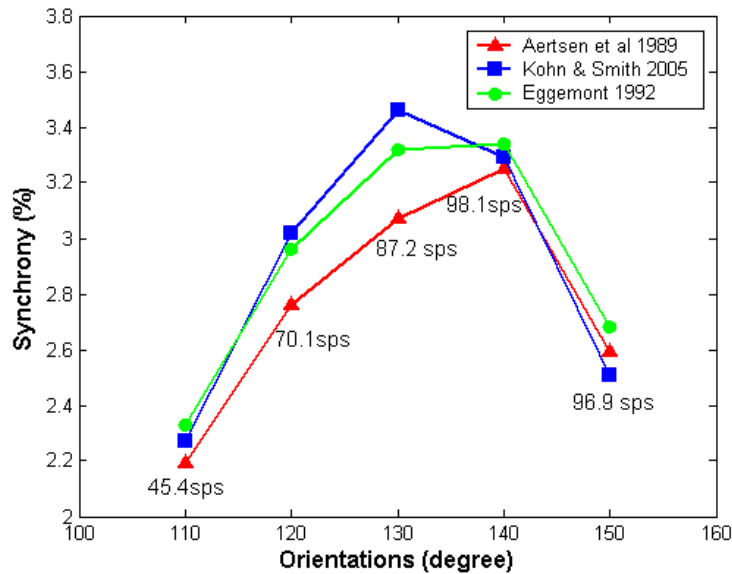
methods across

Figure 7.2 - 4 Three normalization methods. All show loss of synchrony at 150º despite high firing rate.

summed firing rates modulated by varying stimulus orientation. The JPSTH is the most conservative estimate and the datum at 150º indicates independence from firing rate. Both type analysis (Samonds et al 2003, 7.4-32) and gravitational clustering (Samonds et al 2004, 7.4-33), which quantify synchrony in wholly different ways, yield similar patterns of stimulus dependence of cooperation between pairs. Ito & Tsuji (2000), (7.4-22), demonstrate that any approach to normalization can be flawed without considering the underlying models of spike generation, but stress that there is no approach that is universally applicable due to different firing models in different cells, or even within a given cell under different conditions. Within this context they conclude that Aertsen's JPSTH model is useful as a generalized approach to analyzing experimental data.

Nonstationary firing patterns. Temporally non-uniform influences on firing rate can lead to spurious peaks in the cross-correlogram that do not necessarily contribute to the cooperative encoding of information. There is no definitive solution to this problem, but

95

consideration of the width of the correlogram peaks lends confidence to the analysis. Covariation of both latency and excitability yields peaks that do not directly reflect instantaneous spike timing covariation (i.e., functional cooperation) between neuron pairs (Brody 1999a,b; 7.4-9,10). However, latency or excitability covariation generate peaks that are on a broader time scale (similar to PSTH peaks) than those from spike timing covariation (Brody 1999b, 7.4-10). Brody cites examples of correlogram peaks that are "clearly not caused by excitability covariations" in Ts'o et al (1986), (7.4-39), which shows peaks of a width not exceeding 10 msec, similar to all of the peaks that we report (e.g., Samonds et al 2006, 7.4-34). As an example of the selectivity of our analysis, in a study involving grating stimuli, which generate synchrony only between cell pairs with similar orientations, the JPSTH identified only 79 of 784 possible pairs (10%) as showing significant synchrony (Samonds et al 2004, 7.4-33). With a more comprehensive set of stimuli designed to generate synchrony in both collinear and cocircular pairs, we identified significant synchrony in 188/631 co-responsive pairs (Samonds et al. 2006, 7.4-34), but this still constituted only 30% of the total. In matches between circular stimuli and receptive field configurations, only 2/307 pairs (0.7%) showed significant synchrony where there was no clear relationship between the stimulus and the receptive fields (i.e., false positives). We are confident that with our systematic application of a comprehensive set of stimuli, restriction of analyses to correlation peaks of 10 msec or less and comparisons of stimulus patterns with receptive field maps, we have neither over- or under-estimated informative synchrony to any significant degree (see 7.2.3.5).

7.2.3.4 Correlation between JPSTH and Coherence Analyses

Synchronized neural responses, which often are accompanied by oscillations in the gamma frequency band, exist extensively in visual cortex and are proposed as supporting the perception of visual structure. Neural synchrony and oscillation are normally studied with cross-correlation analysis and coherence analysis respectively, which measure the association between neural activity in the time and frequency domains. We studied responses from cat visual cortex to explore the relationship between synchrony and coherency. With a Cyberkinetics 10x10 microelectrode array, we recorded 66 complex cells from areas 17 and 18 in two paralyzed and anesthetized cats. Drifting sinewave gratings (SF = 0.5 cycle/°, TF = 2Hz, Contrast = 50%) were used as visual stimuli. We identified 694 pairs that showed significant synchrony using the JPSTH representation of correlation. We also studied frequency dependence in these synchronized pairs with multi-taper coherence analysis (Chronux 1.0). The multi-taper method computes the averaged spectral estimates by applying several orthogonal windowing functions (i.e. Slepian functions). Thus, the multi-taper method provides a coherence estimate with reduced bias and variance compared to direct spectrum estimation with single windowing procedure. Among all cell pairs that exhibited significant synchrony, we found that 98.4% data samples showed coherence values higher than the 95% confidence interval at certain frequency band(s) (Figure 7.2-5[A & B]).

A   B
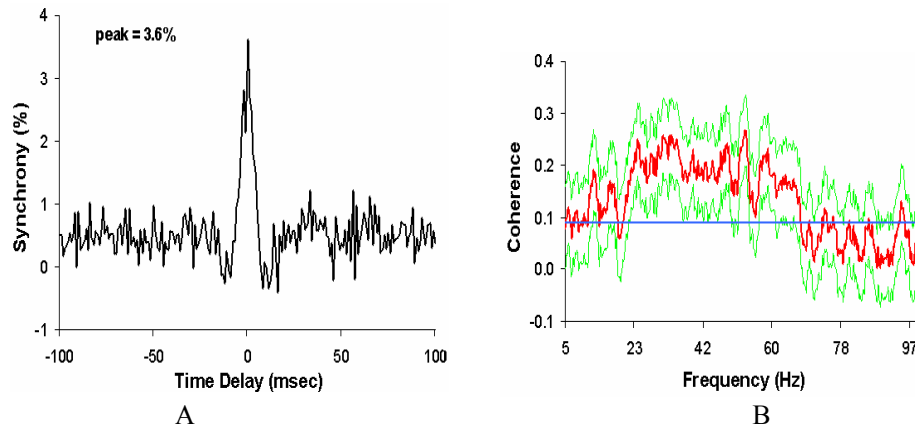
Figure 7.2 - 5 (A) Cross-correlation analysis with JPSTH method shows that a pair of cells exhibited strong synchrony in their firings. (B) Coherence analysis on the same cell pair with multi-taper method shows that the frequency dependence between the two spike trains mainly exists in a frequency band of 25-65 Hz.

To explore the relationships between JPSTH and coherence analyses, we conducted regression analyses between the results from these two methods. We integrated the area underneath the central peak in the cross-correlogram (CCH) and the area between the estimated coherence (red trace in Figure 7.2-5B) and the theoretical 95% confident limit (blue line in Figure 1B). Linear regression analysis (Figure 7.2-6) reveals strong correlation between neural synchrony and the

Figure 7.2 - 6 Scatter plot of integrated synchrony and integrated coherence.

corresponding coherence ($R^2 = 0.63$), which validates the normalization implemented in the JPSTH. Our results suggest that cross-correlation analysis and coherence analysis are internally related, though these two methods study neural connectivity from wholly different perspectives.

97

7.2.3.5 Temporal Structure and Neural Correlation

The fine temporal structure in neural spikes cooperates with the average response rate of visual neurons to provide visual information, though these two variables have different roles in coding specific properties. We recorded 66 complex cells from areas 17 and 18 in two paralyzed and anesthetized cats under the stimulation of drifting sinewave gratings (SF = 0.5 cycle/°, TF = 2Hz, Contrast = 50%). A total of 694 pairs showed significant synchrony quantified by cross-correlation histogram (CCH) derived by JPSTH method. The frequency dependence of these synchronized pairs was further quantified with multi-taper coherence analysis. We applied a spike jittering method with different time distributions (±5ms, ±10ms, and ±2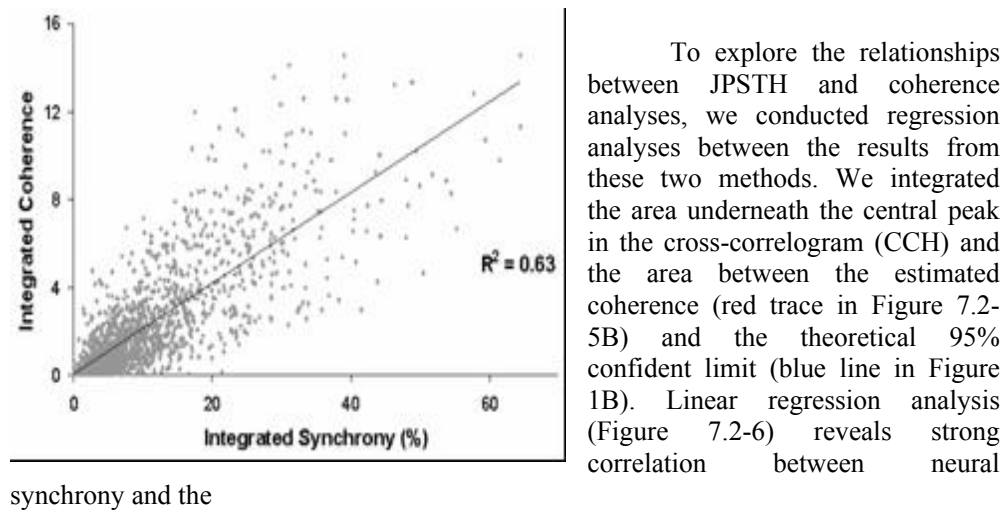0ms) to perturb the timing accuracy in the spike trains at different levels to see how synchrony and coherence depend on fine structure. We found that neural synchrony systematically dropped with the increase of jitter time. Figure 7.2-7 shows an example of synchrony modulation with spike jittering. Synchrony dramatically decreased after spikes were jittered within a ±10ms or ±5ms time range. Coherence analysis on the same pair of cells shows that the frequency dependence also decreased with the increase of the spike jittering range. We found that strong coherence between the unjittered spike trains mainly existed in the gamma band (40 – 70 Hz) with the highest coherence value (coherence = 0.26) located at 52 Hz (Figure 7.2-8A). After the spikes of both cells were randomly jittered across a ±5ms range, coherence strength (red area between the coherence curve and 95% confidence interval) dropped dramatically (Figure 7.2-8B). When the two spike trains were jittered across broader time ranges (±10ms and ±20ms), the frequency dependence between these two cells were almost completely destroyed (Figure 7.2-8C&D).

The reduction of temporal and frequency dependence after spike jittering in the above example also applies to our entire population. We averaged the synchrony and coherence data for all synchronized pairs we identified. The average synchrony is highest before spike trains were jittered. The central peak of the averaged CCH before spike jittering has an amplitude of 1.16%. After the spikes were jittered randomly with increased time ranges (±5 ms, ±10 ms, and ±20 ms), synchrony gradually reduced to 0.82%, 0.66%, 0.56% respectively with statistical significance (paired student's t-test, $p < 10-10$). Meanwhile, the width of the central peak on the averaged CCHs also increased when the spikes were jittered across a broader time range, indicating a disruption of the temporal relationship between cells. We also found that the average coherence spectrum for the original spike trains has its greatest power in the low frequency band and the second peak in the coherence curve is found around 45 Hz (Figure 7.2-9A). The power in the coherence spectrum gradually decreased with the increase of the spike jittering range. When spikes were jittered in the ±5ms range, the second coherence peak disappeared, and when spikes were jittered in the ±10 or ±20ms range, the coherence trace in the gamma range flattened.

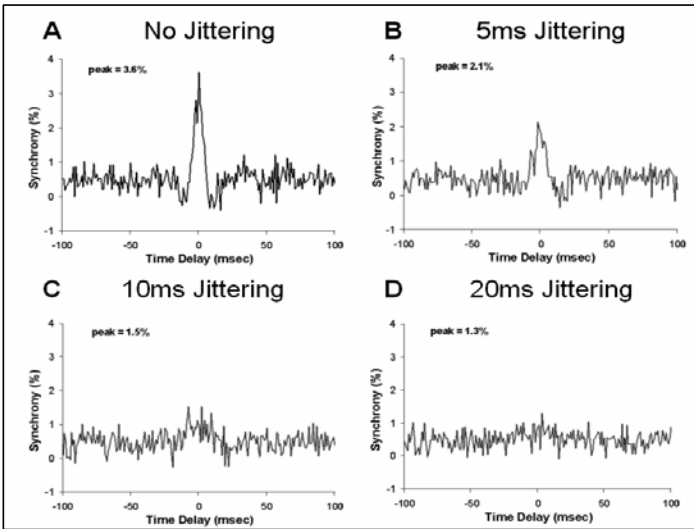**Figure 7.2 - 7 A pair of cells with similar orientation preferences shows synchronized firing with stimulation of moving sinwave gratings. Synchrony systematically reduced after spike timings in the original spike train were jittering in increasing time range.**
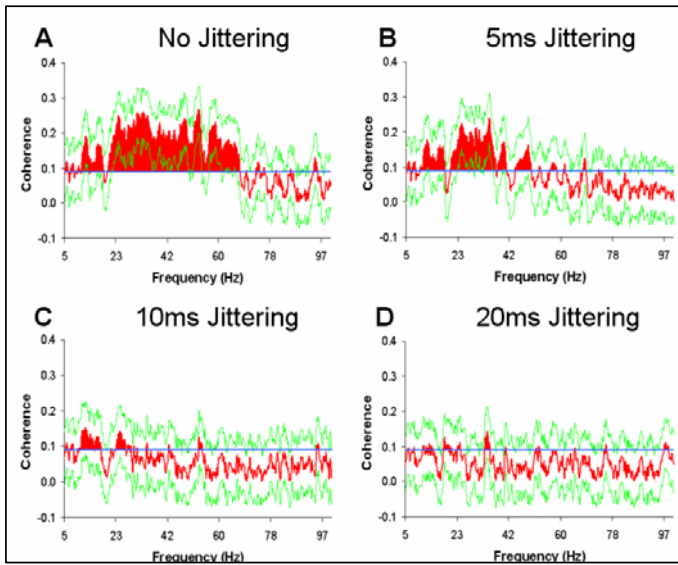

Figure 7.2 - 8 Coherence analysis shows that the frequency dependence between cells also reduces after spike timings were jittered in increasing time ranges.
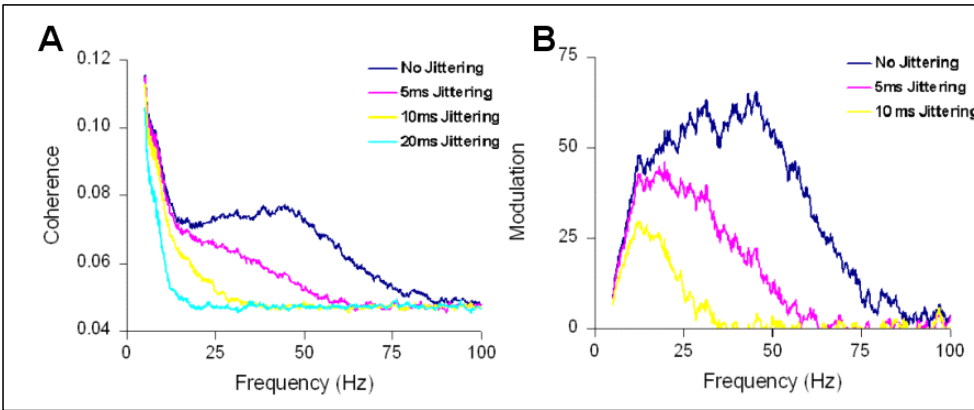
Figure 7.2 - 9 Population averaged spectrum shows that coherence dropped after spikes were jittered while the gamma coherence exhibited greatest loss compared to that of other frequency bands.

To explore how much frequency dependence is embedded in the fine temporal structure, we derived coherence modulation ($\Delta m(f)=[C(f)-C_{bl}(f)]/\ C_{bl}(f)$x100%) of different timing accuracies with respect to the "baseline" coherence (i.e., coherence expected in the absence of fine coordination), which is defined by the average coherence for spike trains jittered in the ±20ms range. We integrated the areas below the modulation curves with different jittering ranges (no jittering, ±5 ms jittering, or ±10 ms jittering), and compared the modulation loss among alpha (5 – 15 Hz), beta (15 – 40 Hz), and gamma bands. In the alpha band, the integrated area was reduced by 9% or 34% respectively after ±5 ms or ±10 ms jittering. In the beta band, reduction was 35% or 81% respectively after ±5 ms or ±10 ms jittering. In the gamma band, however, the reduction was 81% or 97% after ±5 ms or ±10 ms jittering. Our results suggest that the fine temporal structure in neural spike trains is critical in maintaining the frequency dependence between neurons, and that the frequency band that is most sensitive to the integrity of the temporal structures in the neural spike trains is the gamma band. Since the global statistics (average firing rate, interspike intervals) of the spike train are on average preserved by jittering, we conclude that the synchrony and spectral correlations result from active processes and not artifact.

7.2.3.6 Neural Cooperation is Dependent on Spatial Coherence

Synchronization of neural responses is a stimulus-dependent phenomenon. Neural synchrony can be reduced by spatial disorganization or discontinuity in stimuli, but there has been no systematic study of how synchrony depends on coherent contours, as opposed to general spatial coherence (i.e. motion as a unit). We studied the response (synchrony and coherence) modulation in 197 cell pairs corresponding to the perturbation of spatial coherence in the visual stimuli. The unperturbed stimulus was drifting sinewave gratings (SF = 0.5 cycle/°, TF = 2Hz, Contrast = 50%). The spatial coherence in the stimulus was systematically perturbed by randomly swapping pixel areas (0.13 × 0.13 degree^2) in the stimulus (Figure 7.2-10A). We found that the average synchrony and coherence systematically dropped with a decrease of spatial coherence (increase of swapped pixels), while the gamma band (40-70 Hz) coherence displayed faster reduction

100

than either raw synchrony or that in the alpha (5-15 Hz) and beta (15-30 Hz) bands (Figure 7.2-10 B&C). The gamma oscillation thus appears to be the most sensitive indicator of image coherence.
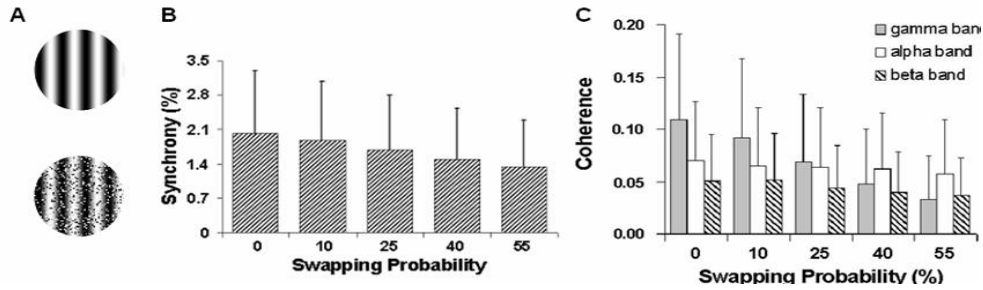
Figure 7.2 - 10 (A) Top: Sinewave gratings with coherent structure; Bottom: A perturbed stimulus with 40% pixels being swapped randomly. (B) The average synchrony dropped with a higher percentage of swapped pixels. (C) Gamma coherence decreased faster than alpha and beta coherence as the spatial coherence is perturbed.

To explore the evolution of neural cooperation, we studied the temporal development of neural synchrony and coherence by deriving 2-dimensional CCHs and coherence plots using a 500ms moving window with 50ms step resolution (Figure 7.2-11 A&B). The average synchrony reaches a maximum at nearly the beginning of the stimulus (50ms after stimulus onset), but the gamma coherence reaches the maximum much later (700ms after stimulus onset).
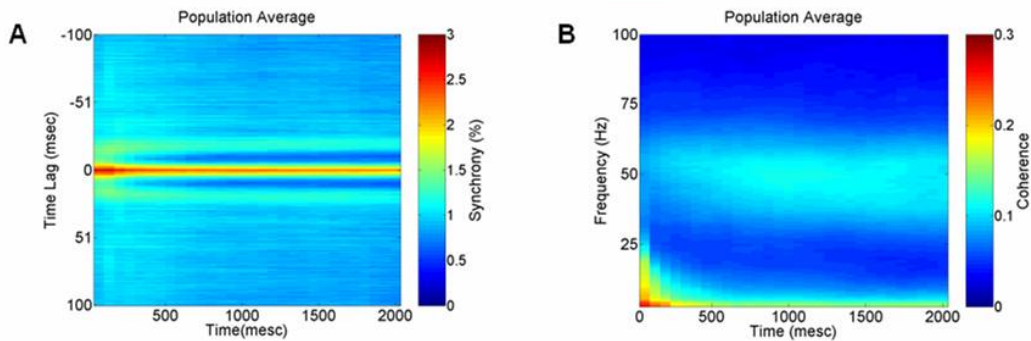
Figure 7.2 - 11 (A) Population averaged 2-d CCH (B) Population averaged 2-d coherence plot

Our results suggest that the spike timing synchronization is induced nearly instantaneously by the coherent structure in the visual stimuli while frequency-dependent synchronization develops more slowly, presumably through network interactions. Gamma synchrony would appear to signify a cooperative representation of image detail that cannot be achieved through the more basic spike synchronization of cell pairs.

101

7.2.3.7 Contour Quantification and Analysis

Synchrony has been studied among pairs of neurons with artificial stimuli (gratings, rings), but its behavior among larger assemblies in the context of natural vision remains unknown. One challenge in analyzing responses to natural stimuli lies in linking responses to a specific stimulus attribute. We have recently found that synchrony may encode contours represented by artificial ring stimuli (Samonds et al 2006, 7.4-34) and wanted to know if this finding extrapolates to complex contours in natural images. As a preliminary test, we derived a new measure for detecting and quantifying cooperative firing within neural assemblies of arbitrary size and used this measure to describe how synchrony changes with different structural modifications of the same natural image. We found that degradation of image structure (contours) by noise or low-pass filtering was represented more strongly by synchrony than by average firing rate in large assemblies.

To investigate the role of synchrony as a contour-encoding mechanism in natural vision, we examined the particular spatial structure that might provide the ideal stimulus for an assembly. In a method adapted from Smyth et al (2003), (7.4-38), and Weliky et al (2003), (7.4-44), we presented a natural image sequence and identified images that elicited a synchronized response in a given group. Orientation and spatial frequency components filtered by the measured selectivity and spatial localization of each cell in the assembly were extracted from each image, summed together and weighted by the magnitude of the response. The resulting composite synthesized a stimulus attribute seen in each picture or combined different structural features to create a new attribute that was ideal for the group.

As a preliminary finding (Figure 7.2-12), we have applied the analysis to an assembly of 4 cells. Orientation and spatial frequency components spatially matching the preferences of the cells were extracted from the ten images with the highest synchrony response and the ten images with the highest average firing rate response for the group. The extracted features were weighted by the magnitude of the response and summed to produce the final composite images. We found that the receptive fields of the cells were aligned on a complex contour in the image with the highest synchronized response. Furthermore, spline and receptive field analyses revealed that each complex contour was relatively conserved across images with similarly high synchronized responses.   In contrast, contours were not conserved in the images generating the highest average firing rate across the assembly.

The image sequence included 2 null stimuli and 336 images, each rotated at 9 angles (40° to 360°, in 40° increments), for an effective stimulus set of 3026 pictures. Each image was 18° x 18°. The images were displayed in a random order for 0.5 sec followed by 0.5 sec of mean luminance. The entire sequence was shown 10 times (in different random orders). Pictures were scaled to have the same global contrast. We recorded from 75 cells in the visual cortex of two paralyzed and anesthetized cats and randomly identified 4500 neural assemblies, ranging in size from 2-10 cells with 500 assemblies per size group. In practice, we have found that any arbitrary group of 8 cells or less will reliably synchronize to some of the 3026 images, and some groups of 9-10 cells will repeatedly synchronize to a few (e.g., 3/3026) particularly complex images.

These results support the role of synchrony as a contour-encoding mechanism. As a check on the validity of these predicted trigger features, we will filter all 3026
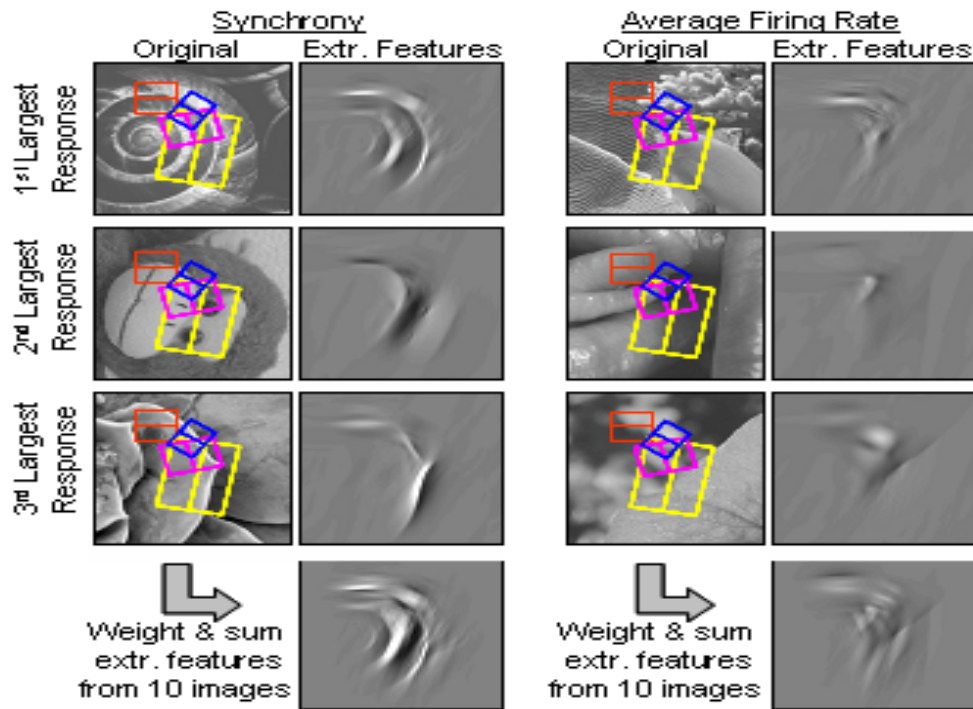
Figure 7.2 - 12 Natural images with the largest synchrony and firing rate responses (normalized to the maximum for each cell) for a given assembly of 4 neurons whose receptive fields and preferred orientations are outlined. To the right of each image are the extracted features (contrast enhanced 2.5x) for the assembly. Note that the extracted components with large synchrony responses tend to describe complex contours in the images. The top ten extracted images were summed and weighted by the magnitude of their response to produce the final images (contrast enhanced 10x)

images with the trigger feature associated with each assembly and compute a score for each image based on the resulting energy. A threshold score will be determined from those images known to generate synchrony above the chance level. Some images that did not trigger synchrony in a given assembly may yield energy above the threshold level, indicating cases in which the assembly "missed" a putatively effective feature. The control analyses will help to confirm whether or not linear summations are valid. They may also demonstrate the effects of contour occlusion. Naturally-occurring occlusions across continuous contours may disrupt synchrony, which would show up as "missed" features in the control analyses.

From data collected using the same stimulation protocol as above, we will perform a cluster analysis to determine how each assembly classified the natural image sequence. Hierarchical clustering (similar to Rolls & Tovee, 1995, 7.4-31) will be performed on the response correlation matrix, which contains the correlations between

103

the pairs of all responses to the image sequence for each assembly. Images within the same cluster will be analyzed for contour content by fitting a spline to large gradients of contrast information in the image near the focus of the assembly. A score will be determined for each cell based on the degree of fit of the cell's preferred orientation to a line tangent to the spline and receptive field distance from the spline. The mean score for the assembly represents a way to quantify the similarity between the assembly configuration and the contour content of the stimulus.

7.2.3.8 Dependence of Group Synchronization on Contour Structure

Our brains process and interpret sensory information in order to generate perceptions of the environment or motivate behavior. However, the underlying mechanisms by which salient stimulus features are represented in neuronal responses remain unresolved. We have previously shown that synchrony between cell pairs can represent curvilinear contours (Samonds et al 2006, 7.4-34), suggesting that synchrony within larger assemblies may be involved in encoding more complex contours. Extending assembly formation to cells with spatial relationships that are not collinear is vital in establishing whether synchrony might serve as a general mechanism for contour integration and shape detection.

To investigate the role of synchrony as a contour-encoding mechanism in natural vision, we measured the synchronous responses of large neural assemblies to a sequence of natural images. By correlating assemblies and image elements, we found circumstantial evidence to suggest that *the specific feature that best drives a synchronous assembly is a continuous, well-defined contour*. For a more thorough investigation, we quantitatively related the contour content of images to the spatial organization of the cells composing the synchronous assembly. Since measuring properties of contours in images (e.g. degree of presence or absence) is subjective and depends on the amount of blur, contrast, occlusion, etc., we chose to measure how well a contour structure matches the assembly configuration and then related the assembly configuration to the image.

We used criteria from the association field theory (Field et al. 1993, 7.4-15; Hess et al. 2003, 7.4-18) to quantify how well an assembly fits contour structure. Association field theory, which is based on studies of the perception of contours and continuity, predicts linking between orientation-tuned cells that is dependent on their joint relative orientation and spatial position. The probability for linking is strongest between contiguous elements with shallower relative angles and closer separations. Using measures that represent the distance between neighboring cells, the difference in orientation preferences, and contiguity, we created a three-dimensional vector (R), the length of which is inversely proportional to the degree of association (see Figure 7.2-13A). We defined the Contour Index, C, as a reversed, normalized version of R which represents the degree to which an assembly configuration fits a contour structure.
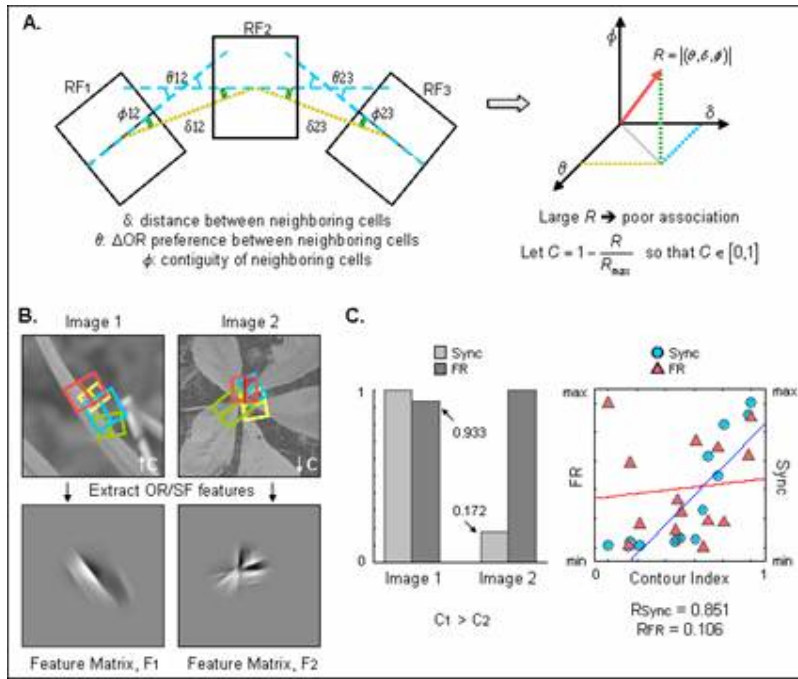
Figure 7.2 - 13 A. Measure to quantify how well an assembly fits contour structure using criteria from the Association Field Theory. B. The receptive fields of two assemblies superimposed on the images with the largest synchrony response and feature matrices depicting the local contrast structure in the image to which the assembly is responding C. Bar plot shows normalized synchrony and average firing rate responses for the assemblies depicted in B. The scatter plot shows synchrony and average firing rate versus Contour Index for assemblies chosen with a range of C values (N = 14). For each assembly, we measured responses across 1513 stimuli and chose the image with the largest synchrony response.

To determine how well the spatial organization of the assembly matched an image, we used the assembly's average firing rate response. Pooled cell activity is directly linked to local contrast structure (Weliky et al 2003, 7.4-44), so the degree of response is a reflection of how well the orientation and spatial frequency components in the image match the tuning properties of each cell in the assembly. Figure 7.2-13B shows the receptive fields of the cells comprising two assemblies and the corresponding images which generated the largest synchrony responses. The amount of response can be visualized by creating a local contrast structure feature matrix by extracting orientation and spatial frequency components in the image that match the tuning properties of each cell in the assembly (Weliky et al 2003, 7.4-44).

In this example, each assembly has a large average firing rate response (see Figure 7.2-13C bar plot), but assembly 1 also had a large synchrony response. The configuration of assembly 1 is more similar to a contour (higher Contour Index), which means the contrast structure to which it is responding is more likely to be arranged in a contour as compared to assembly 2. Results from twelve additional assemblies also reveal that synchrony is directly correlated with the Contour Index (see Figure 7.2-13C

scatter plot). These findings suggest that contoured assemblies synchronize to similarly arranged local contrast structure and provide quantitative evidence that synchrony signals contiguous, well-organized contours in natural images.

7.2.3.9 Sparse Coding as a Framework for Information Processing in the Brain

Although current technology allows us to monitor the interactions of hundreds of neurons simultaneously, we cannot understand their contribution to visual perception without a conceptual framework that describes the strategy for information processing. We investigated the selectivity of synchrony in large assemblies in the context of sparse coding, where information is represented by a small subset of cells from the population. *Population sparseness* describes the response probability of the cell population at one instance in time. The distribution of responses is leptokurtic with a large peak at zero (or chance), indicating that most of the population is inactive. *Lifetime sparseness* describes the activity of one neuron (or one assembly) in response to the set of all input images over time (Willmore & Tolhurst 2001, 7.4-45) also yielding a leptokurtic response distribution with a peak at zero (or chance). Across all input images, all cells have an equal response probability but have a low response probability for any single image. With sparseness, the dimensionality is not reduced, but the redundancy in the input is transformed into the redundancy in the firing pattern of the cells (Field 1994, 7.4-16). In this manner, information about the environment is distributed across all cells and objects are represented by which cells are active and not by the relative activity or overall amount of activity of a specific subset.

This approach has been found to be consistent with the representations of natural scenes (Field 1987, 1989, 1994, 7.4-13,14,16; Zetzsche 1990, 7.4-50). The degenerate mapping of highly correlated stimuli to a sparse representation is described as a fault-tolerant method of reliably learning and discriminating closely-related patterns (Leonardo 2005, 7.4-26). In the primary visual cortex of primates, neurons produce (lifetime) sparse responses when stimulated with natural image sequences (Vinje and Gallant 2000; 2002, 7.4-42,43) and high lifetime and population sparseness is found in V1 of ferret (Weliky et al 2003, 7.4-44).   Furthermore, responses are most sparse when the non-classical receptive field is stimulated implying that sparseness is modulated by context. Several findings also suggest the visual system may be optimized for processing the statistics of natural scenes (Barlow 1961, 7.4-6; Kersten et al 1987, 7.4-23; Simoncelli 2003, 7.4-36) by employing a sparse coding strategy (Olshausen and Field 1996, 7.4-28; Bell and Sejnowski 1997, 7.4-8; van Hateren and van der Schaaf 1998, 7.4-41; van Hateren and Ruderman 1998, 7.4-40; Hyvarinen and Hoyer 2000, 7.4-20).

There are several biological advantages for employing a sparse coding strategy. For instance, by utilizing a small number of neurons during any one task, sparse codes are energy efficient. Estimates of the energy required for signaling in cortical neurons suggest that less than 2% of the population can be significantly active at any given time (Attwell and Laughlin 2001, 7.4-3; Lennie 2003, 7.4-25). Experimental evidence has shown that average firing rates are low for natural images compared to that from optimal grating stimulation, which reduces the metabolic demands of visual processing (Baddeley et al 1997, 7.4-4; Guo et al 2005, 7.4-17). Also, several theoretical and computational studies have shown that sparse representations are most effective for storing patterns in

associative memory models (Willshaw et al 1969, 7.4-47) and they are advantageous for learning associations in neural networks (Palm 1980, 7.4-30; Baum et al 1988, 7.4-7; Zetzsche 1990, 7.4-50; Field 1994, 7.4-16). Furthermore, Hoyer and Hyvarinen (2002), 7.4-21, have shown that a multi-layer sparse coding network is capable of learning contour coding from natural images in an unsupervised fashion.

While sparse coding requires a subset of cells to be active for any given input, what properties of the input define the subsets formed? We hypothesized that this representation is reflected in the cooperative activity of the subset. In other words, synchrony is a way to implement a sparse coding strategy where higher-order stimulus information is represented in the precise temporal pattern of a neural assembly. Precise temporal coordination among neurons preserves the requirements for sparse coding in that information is transmitted efficiently (through cooperation) and by a few neurons (assembly).

We assessed the selectivity of synchrony on the basis of the probability distribution of such responses across presentation of numerous natural images. We measured the sparseness of synchrony-based and firing rate-based coding strategies using a natural image sequence of 3024 pictures. Groups of 2-8 cells were chosen for analysis. We tested and compared 6 sparseness metrics that can be alternatively computed for population or lifetime analysis by changing 2 variable definitions. We used 3 metrics defined by Olshausen & Field (1997), 7.4-29, kurtosis, the Rolls & Tovee (1995), 7.4-31, measure as modified by Willmore & Tolhurst (2001), 7.4-45, and the "activity (or response) sparseness" measure (Willmore & Tolhurst 2001, 7.4-45).

We found that synchrony response distributions (Figure 7.2-14A) were leptokurtic and the kurtosis increased nearly exponentially with group size (2 cells: $S_1 = 0.957$, 4 cells: $S_1 = 9.13$, 6 cells: $S_1 = 27.7$, 8 cells: $S_1 = 68.9$). The kurtosis for firing rate response distributions (2 cells: $S_1 = 0.149$, 4 cells: $S_1 = 0.249$, 6 cells: $S_1 = 0.484$, 8 cells: $S_1 = 0.889$) did not change as a function of group size ($p > 0.6$). Using the response sparseness metric (Figure 7.2-4B), we found that assemblies of 2 cells had significant cooperative activity for 10.6% of the stimulus sequence (321 images) and assemblies of 8 cells had significant cooperative activity for 4.1% (124 images). However, assemblies of 2 cells had significant average firing rate activity for 14.9% of the stimulus sequence (451 images) and assemblies of 8 cells had significant average firing rate activity for 8.4% (255 images). Overall, our results suggest that increasing assembly size enhances the ability of synchronous assemblies to discriminate among the natural image sequence more than a firing rate code. This was true for all 6 sparseness metrics tested and for both lifetime and population responses.
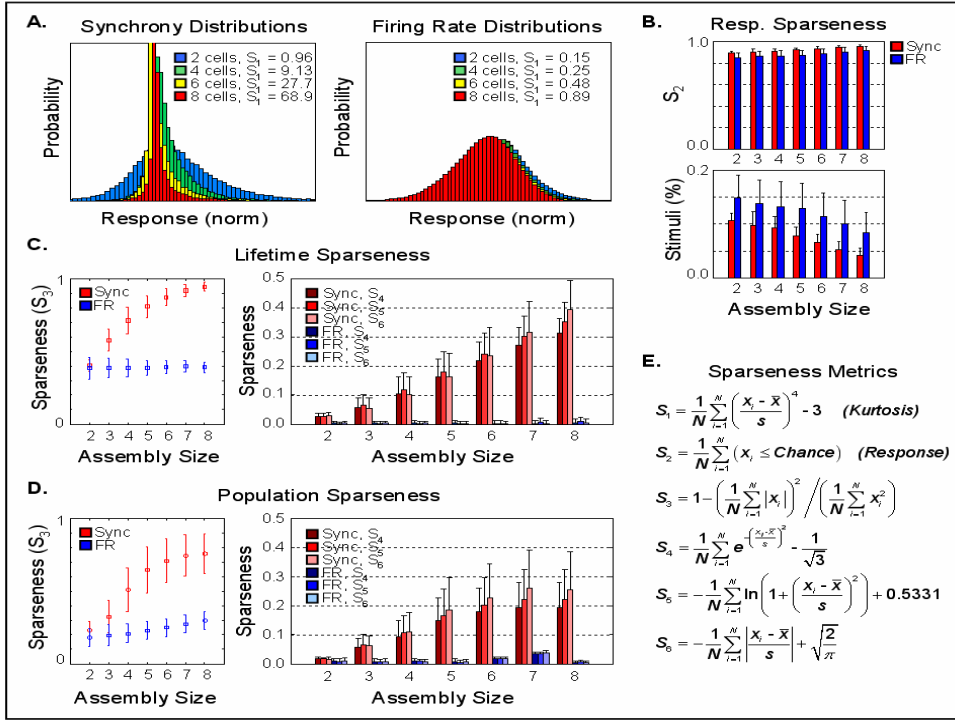
Figure 7.2-14 **(A) Average kurtosis for synchrony and firing rate response distributions with 2, 4, 6, and 8 cells per assembly. (B) Response Sparseness is computed as the number of images to which the assemblies did not respond (top; bottom plot shows [1-response sparseness] and represents the number of images with responses that were 1.96(stdev) above chance). (C) Lifetime and (D) Population sparseness as a function of assembly size using the last 4 metrics in (E). Population sparseness describes the response distribution of many assemblies to 1 image. Lifetime sparseness describes the response distribution of 1 assembly to many images. S3 is the formula proposed by Rolls and Tovee (1995), 31, as modified by Willmore and Tolhurst (2001), 7.4-45. S4-S6 are measures provided by Olshausen and Field (1997), 7.4-29 and Willmore et al. (2000), 7.4-46.**

7.2.3.10 Conclusions - Bio-Optics of Vision

Current models of visual processing (form extraction, contour detection) are based largely on the activity of individual filters (neurons) as opposed to population activities.   This is mainly a consequence of the technical challenges of recording simultaneously from larger populations of neurons.   Our laboratory was routinely successful in recording from >60 neurons simultaneously

We have pursued validation of the Binding By Synchrony hypothesis, in which complex visual structures are integrated by the synchronization of cellular assemblies on a msec scale. We have found:

♦ The formation of larger (>2) synchronized assemblies occurs much more often than would be predicted by chance
♦ Synchronization is stimulus-dependent and highly selective
♦ The analytical methods used to quantify synchrony (JPSTH and Coherency) are reliable and internally consistent
♦ Synchrony is highly dependent on fine temporal structure in spike trains and appears causal, in that reconstruction of sequences with identical overall firing characteristics nearly destroys all synchrony
♦ Synchrony is highly dependent on spatial coherence within an image
♦ Synchrony appears to be encoding contiguous contours of similar orientations
♦ Sparse coding via synchrony appears to be an efficient and viable substrate for the representation of coherent visual structures

7.2.3.11 Bio-Electrode Development

In a related area, we have discovered a process for creating a nanodiamond electrode of a new and novel nanostructure, denoted as a "Coral" Carbon Microprobe, Figure 7.2-15. These "coral"-type microstructure carbon films, with and without N2 incorporation, were grown on sharpened tungsten microprobes by plasma enhanced chemical vapor deposition (PECVD) using H2/CH4/N2 and H2/CH4 gas mixtures, respectively. The electrochemical behavior of the coral-type carbon coated tungsten microprobe, characterized in various concentrations of ferrocyanide in a background of 0.1M KCl, show excellent structural stability with similar microstructure before and after prolonged analysis without the need of surface pretreatment. The microprobes exhibit quasi-reversible kinetics with high signal-to-noise S/B ratio. The N2 incorporated microprobe shows a slightly wider potential window, no surface adsorption of the analyte and higher sensitivity as compared to the sample without nitrogen incorporation. Furthermore, the wide potential window of ~3V is very good comparing to the boron-doped highly quality diamond which has ~3.5V. The good electrochemical behavior and simple fabrication method make the "coral" carbon film microprobes an excellent candidate for electrochemical sensing.
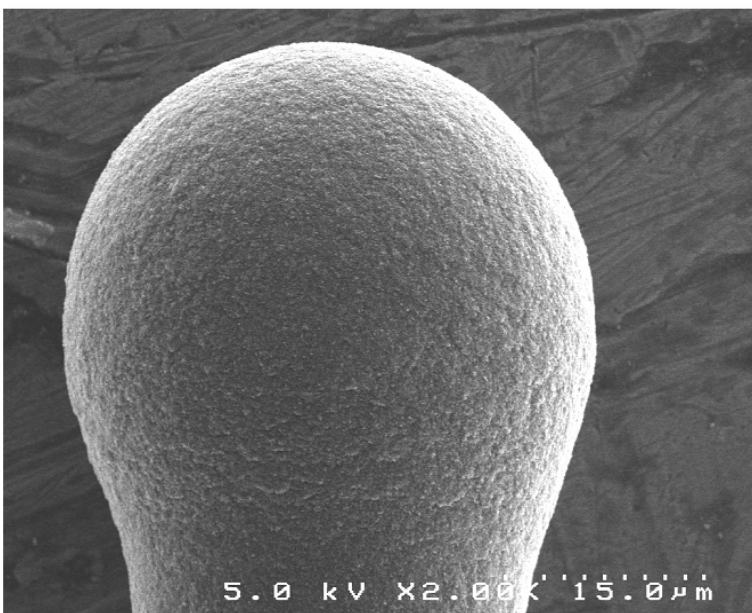
Figure 7.2-15 SEM of "coral" type nanodiamond grown on tungsten needle substrate for bio-electrode application

We proceeded with detail characterization of the novel "coral"-type nanodiamond electrode. Specifically, the electrode performance of the undoped and nitrogen incorporated nanodiamond films was begun
.

Figure 7.2.-16 shows the SEM micrographs of "coral"-type microstructure carbon films grown on sharpened tungsten microprobes by plasma enhanced chemical vapor deposition (PECVD) using H_2/CH_4 and $H_2/CH_4/N_2$ gas mixtures that give rise to the undoped (sample 1) and N_2 incorporated (sample 2) carbon microprobes, respectively. Sample 2, which has N_2 incorporation, has a smoother surface morphology as compared to that of the undoped sample 1.
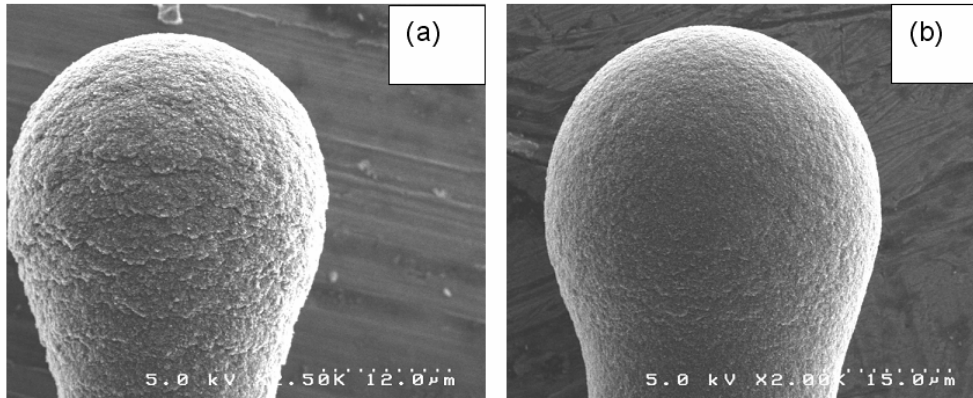
Figure 7.2-16 SEM micrographs of: (a) sample 1 (carbon film without nitrogen) and (b) sample 2 (carbon film with nitrogen)

However, the corresponding high magnification micrographs, Figure 7.2.-17, show similar microstructures for both the samples resembling naturally occurring coral. The EDS spectra confirm that the films are indeed carbon and show the presence of nitrogen in the N_2 incorporated carbon film.
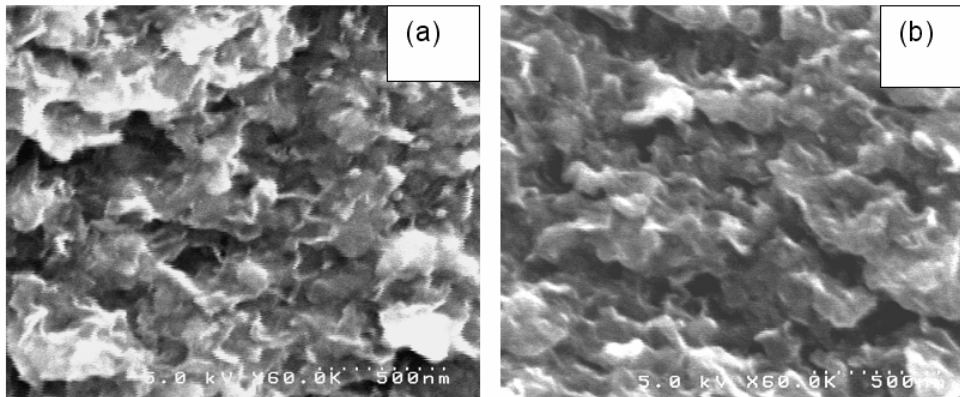
Figure 7.2-17 High magnification SEM micrographs of: (a) sample 1 (carbon film without nitrogen) and (b) sample 2 (carbon film with nitrogen)

111

The microprobes were used to establish the potential window and background current in 0.1M KCl at a scan rate of 100 mV/s. The voltammograms seen in figure 7.2.-7 indicate a wide potential window and low background current which makes them candidates for detection of a wide variety of analytes with a high signal to background ratio. Furthermore, sample 2 (N_2 incorporated carbon film) shows a slightly wider window of ~3V as compared to ~2.8V for sample 1 (no nitrogen). These values are impressively high, considering 'normal' boron doped diamond has a ~3.5V potential window (Xu J. (1997), (1998), 7.4-48, 49).
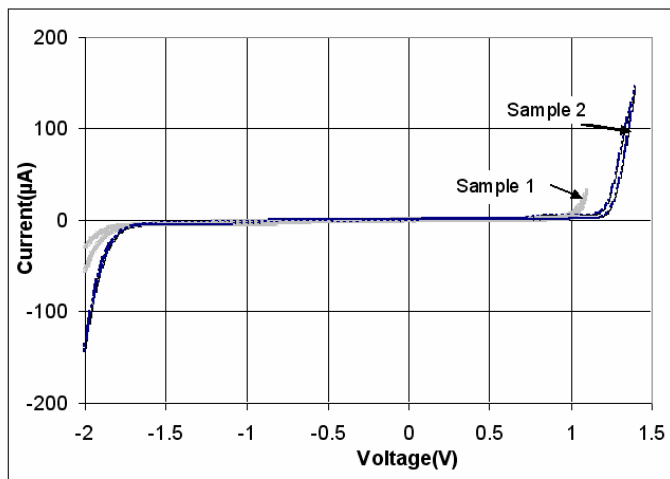
Figure 7.2-18 Cyclic voltammograms obtained from Sample 1 (Undoped carbon film) and Sample 2 (N2 incorporated carbon film) in 0.1M KCl at a scan rate of 100mV/s

Concluding the Bio-Electrode Development, the "coral" carbon films coated tungsten microprobe, with and without N2 incorporation exhibited excellent electrochemical behavior. Both the undoped and N2 incorporated carbon film microprobes have very similar microstructure, even though the latter showed smoother surface morphology. The electrochemical behavior was under further evaluation. As the funding level was reduced for the Vanderbilt subtask in Year 2, the task re: "Bio-Optic Sensor Electrode Development" took a diminished role and certain other tasks were reduced.

7.3 Research nanotechnology capabilities for enhancing imaging sensor performance, including advanced high definition infra-red displays

7.3.1 Overview

A need exists for an emitter in the infrared and related frequencies of the spectrum that is efficient, strong, responsive, tunable, miniaturizable, electronically addressable and cost effective. Present technology, which often resorts to "hot wires", an approach more than a century old, is fragile, unreliable, slow and expensive.

Vanderbilt has developed its diamond microfabrication capability to achieve **diamond thermal emitters**. The "glowing" diamond, Figure 7.3-1, can be patterned into a variety of configurations and sizes to achieve robust, efficient, cost effective, high-performance, IR (infrared) or other frequencies emission element by employing Vanderbilt's diamond deposition technology. It is possible to change the frequency in the device very rapidly across a wide range of electronically tunable options and further possible to combine these elements into a pixel array.
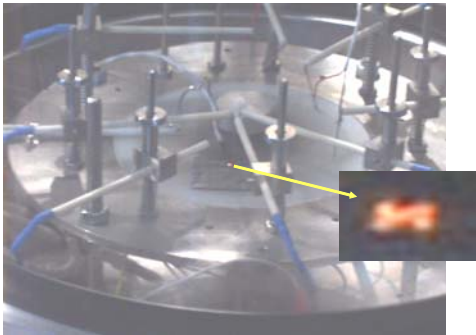
Resistor glows under high current loading.

Figure 7.3 - 1 Infra-red pixel of glowing diamond microresistor

The necessary elements to achieve this
have been demonstrated at Vanderbilt including:
A. Pattern emitting diamond elements with a monolithic microelectronic interconnect.
B. Power behavior including emission from deep IR to visible.
C. Processing capability to achieve emission elements on silicon or ceramic substrates, attached or suspended.
See Figure 7.3-2

Diamond power resistors have the advantage of rapid dissipation of joule heating, assured by the high thermal conductivity of the material. Diamond is excellent for accommodating temperature cycling because of its extremely small thermal coefficient of expansion. Thin film diamond resistors of various sizes have been designed and fabricated on an electrically insulative aluminum nitride substrate. The resistors are fabricated from microwave plasma assisted chemical vapor deposition process. Boron doping was from a trimethylboron (TMB) gas source. The resistance, and hence, Joule or I^2R heating/emission behavior of diamond, is controlled by the doping level in the diamond.

Resistor Micro-Array for IR Display Infrared emitter source comprised of diamond Microstructure pixel element in patterned array technology

The diamond array will be fabricated similar to conventional thin film resistors by processes developed by Vanderbilt. It will be doped with boron to be sufficiently conductive to have controlled Joule heating under applied power. Because the element is diamond, there are many advantages in addition to the modulated set point such as very 'crisp' on off illumination profiles because of diamond's none-higher thermal conductivity.
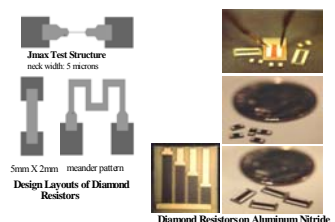
Delineation of the resistors is accomplished by direct etching using reactive ion etching with a patterned metal mask. Resistors with different device geometry and doping concentration have been examined for power density response. Arrays of microstructure resistors were exposed to controlled power levels to examine their thermal response. Temperature is correlated to the spectral irradiance of the blackbody thermal emission.

DIAMOND POWER RESISTORS

Jmax Test Structure
neck width: 5 microns

5mm X 2mm   meander pattern
Design Layouts of Diamond Resistors

Diamond Resistors on Aluminum Nitride

Figure 7.3 - 2 Tunable, miniaturizable, electronically addressable diamond micro-resistor thermal emitters

The technology transfer/commercial ramifications of this technology can be seen from this following short list from the many possible applications:

♦ A very fast digital "TV screen" in the IR region of the spectrum, which can be used for biomedical illumination or mapping, security monitoring, and combat/ weather/ medical image simulation. For example, present techniques for breast cancer involve thermal imaging. The "live" signals can be recreated on the diamond element "pixel" array, then enlarged, "morphed" or otherwise electronically manipulated for enhanced diagnostics and improved predictions.

♦ The diamond emitter will be a very unique illumination source for *chemical analysis*. Many analytical instruments for environmental quality monitoring (air, water, factory effluent, automotive standards, etc.) for food processing, pharmaceuticals, biological fluids (blood, plasma, etc.), oil refining {anywhere that the substances involve organic (Carbon-Hydrogen) materials} use an IR beam to illuminate, stimulate, or otherwise analyze known and unknown samples. The limits of detection (sensitivity), the range (variety of compounds), discrimination (ability to distinguish similar materials, e.g., "good" cholesterol from bad cholesterol) and many other parameters are directly dependent on the brightness (intensity or power), response time, tunability and complexity that can be achieved with the IR source. The diamond emitters can be superior to present materials in all these properties, resulting in purer drugs, faster/cheaper environmental monitoring, quicker/more widely deployed in line process control monitors for everything from food to plastics to fuel.

♦ The printing/copying process - an array of these IR elements, at the microsize achievable with this technology, could significantly alter the cost and size aspects of the entire thermal printing industry. With an addressable linear or 2-D array of rapid response diamond IR (thermal) elements, the fax or POS receipt or conventional copy could be generated in a fraction of the time and a fraction of the cost with a "fraction" of the presently configured printer countertop footprint.

114

7.3.2 Objectives

The development effort was:

♦ First, design and fabrication of a diamond IR emitting element as per Milestone Three (2005), Research nanotechnology capabilities for enhancing imaging sensor performance, including establishing design approach for advanced high definition infra-red displays.

♦ Second, characterization, design optimization and operating limit evaluation of diamond pixel element IR array as per future work in Years Two Through Five (2006-2009):

♦ Research nanotechnology capabilities for diamond based IR pixels, including construction of prototype advanced high definition infra-red displays for enhanced imaging sensor performance

The prototype diamond IR pixel element will be designed in the first year. In the second year and out years, the prototype diamond IR pixel element will be fabricated and tested as a feasibility demonstration. In subsequent years, the design and process will be further developed and characterized, the element performance evaluated for limit behavior. Preliminary design for a multi element array will be achieved and fabrication and characterization will be performed in year 2 to 3.

These objectives were achieved for the duration that the program was funded, said funding being terminated in the second year.

7.3.3 Results

A PDF emitter resistor test array, Figure 7.3-3, was designed and fabricated with a selection of process variables and geometries. This provided an initial data base, identifying the relative importance of various process variables and configurations on the resulting emitters. This evaluation began an assessment for determining methods for enhancing the performance of diamond film resistor IR emitters using plasma enhanced chemically vapor deposited (PECVD) diamond. A model was under development to interpret the observed emission performance.

Cross section of suspended diamond resistor

Cavity mask

Metal contact

Top view of the diamond resistor array
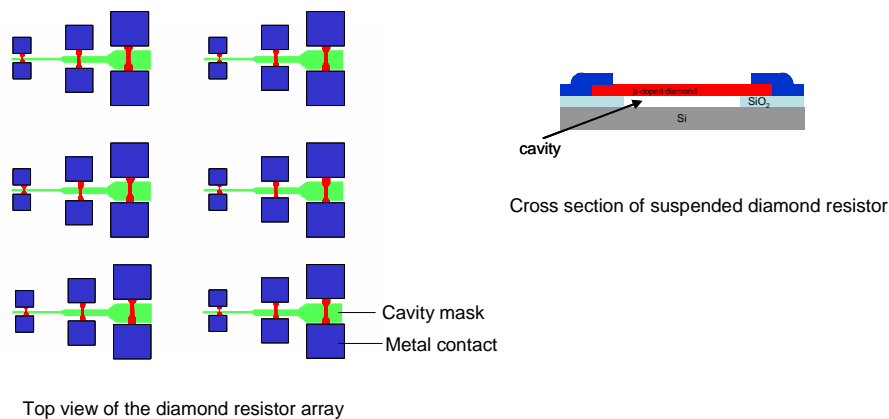
Figure 7.3 - 3 PDF emitter resistor test array

Diamond resistors were prepared and the data collection process improved so that more data could be collected to more accurately reflect the capabilities of the diamond resistors.

For resistor fabrication, diamond layers were grown on more samples. Attempts were made to grow diamond on 1 micron thickness silicon oxide. The growth was not successful as the diamond would not adhere to the oxide layer. The next attempt was to grow doped diamond onto a thin layer of i-diamond, performed with a bias enabled diamond machine to avoid damaging the surface of oxide. This experiment also failed to achieve the desired doped diamond layer due to the same adherence problem. Success was achieved by growing diamond on thicker oxide (about 3 micron thick) layers after preparing the oxide for nucleation.

Resistivity was measured on the sample using the van der Pauw method and found to be ~ 0.06 to 0.08 Ohm-cm. A better diamond film was observed on the thicker oxides.

Earlier measurements made were inferior due to the presence of a ripple in the output signals. This ripple is believed to originate from the power supply due to physical limitations of the pulse generator hardware as it switches current to a load. The power supply input will be tested and characterized to eliminate the ripple that was present in the output signal. Filtering circuitry may be necessary to isolate the ripple.

An interface for Data Acquisition was being built, Figures 7.3-4, 7.3-5, to enable the reading of the input voltage and output current as well as measure the light intensity from the photodiode in a synchronized manner. The voltage and current readings will be obtained synchronously in real time.

A signal isolator would be used to provide more precise input data through a clearer input signal. Adjustments can be made as needed to improve the filtering process in the measurement step.

Figure 7.3 - 4 Basic preliminary schematic drawing of input circuitry for DAQ system
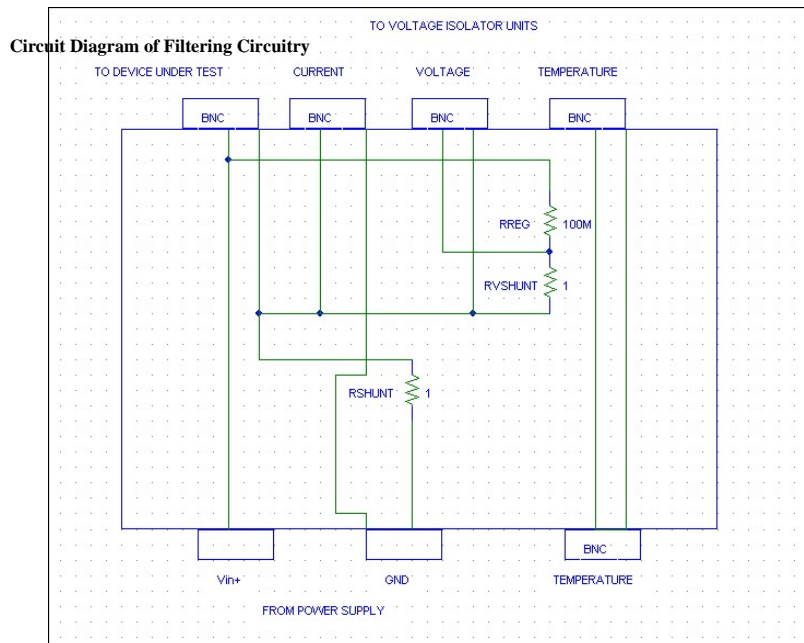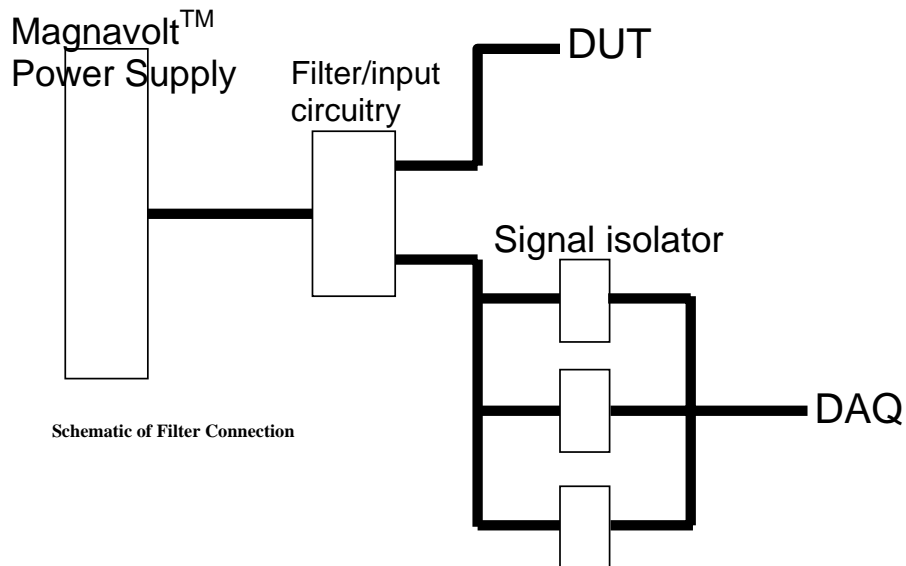

Figure 7.3 - 5 Overall preliminary design for device measurement

The diamond that was successfully grown was etched into the various resistor shapes. The preliminary fabrication results were encouraging and the decision was made to fabricate more resistors with the optimized procedure. A p-doped diamond layer was successfully grown on thick (~3 micron) SiO_2. The diamond layer was grown for 3.5 hours resulted in a thickness of about 3 micron of diamond. A thick insulating SiO_2 is desired for a deeper trench to ensure complete isolation. A 1 micron titanium layer was deposited through e-beam for masking the diamond during delineation process. The delineation process of the resistor was achieved by RIE process using the facility at Auburn University.

Eight samples were processed at Auburn and delineated with the RIE process. The etch rate for RIE from previous observation was ~ 0.1micron/min. However, the first attempt of RIE process failed to produce any resistor pattern because the titanium layer lifted off after 6 minutes of etching. Adjustment of the process parameters was made to reduce the etching rate but similar observations were seen on the second and third samples. The cause of the failure was determined. The 1x1 cm samples were thermally attached using a thermal conductive wax on a 4 inch wafer and this wafer sat on spacers that were attached to a separate 5 inch wafer (RIE machine only accepts a 5 inch wafer). Previously, the samples were attached directly onto the 5 inch wafer with thermal conductive wax in all processes. The gap between the 4 and 5 inch wafer created thermal isolation. The gas in the chamber that should be constantly cooling the wafer couldn't reach it and the high temperature caused an excessive etch rate at the top which nonuniformly removed the titanium and part of the diamond layer.

Although the problem was identified and resolved, the RIE process then suffered from a problem that caused its reflected power to be too high. This created an unsafe environment for the equipment and the process had to be stopped. This problem with the RIE took a long time to be resolved and was a major stumbling block for the fabrication of the diamond resistors. The RIE equipment was eventually fixed; another trip to Auburn completed the process.

Additional diamond resistors were fabricated, increasing our stock of samples available for characterization and measurement. The delineation was performed at Auburn University for the first batch of resistors. Additional samples were fabricated at Vanderbilt and work proceeded to finalize the characterization methods as the program was terminated.

The resistors in this work are freestanding and "necked" shaped in three different resistor dimensions (10 x 50μ, 50 x 100 μ, 200 x 500 μ), see Figure 7.3 -6. The wide range in resistor sizes and the freestanding structure led to problems which complicate optimal characterization of the resistors. The cavity for the freestanding structure is obtained by etching away the underlying oxide. To create the cavity of the largest dimension resistor structure fully excavated, the etching process has to be prolonged. However, this results in the smallest structure getting over etched, Figures 7.3-7 and 7.3-8. To get a properly defined resistor for the smallest structure, the etching process has to be shortened and this results in an improperly excavated cavity for the larger structure. The small number of samples that were previously fabricated didn't allow for resistor structures to be optimized so a trade-off was made such that the etching process etched away part of the smallest structure but was not lengthy enough to form a complete cavity for the largest structure. The resulting resistors were all compromised to a degree. To

obtain optimal resistors for every structure size, more samples need to be made so that each sample can be optimized for a particular resistor size while sacrificing the others.

Cavity area

Metal pad

15.0kV ×40.0
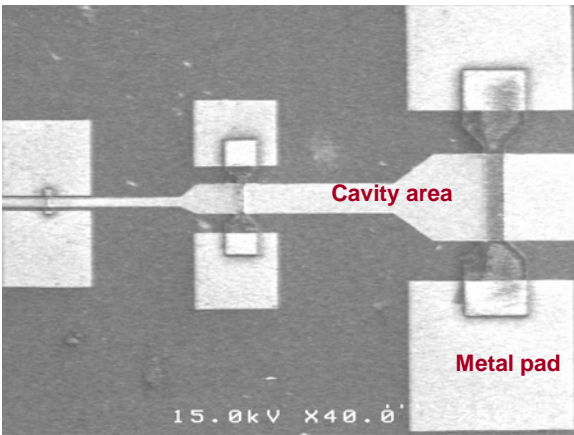
Figure 7.3 -6 Overall layout of the resistors.

15.0kV ×1.30K 23.1μm

15.0kV ×350 85.7μm
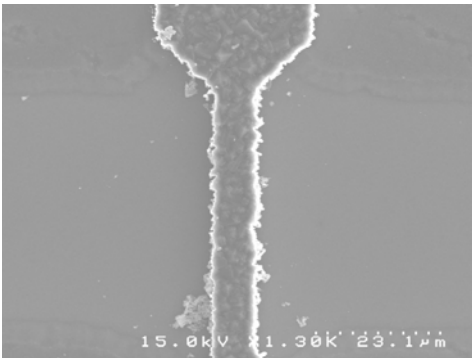
F**igure 7.3 - 7 Over-etched was observed on large small resistor.**
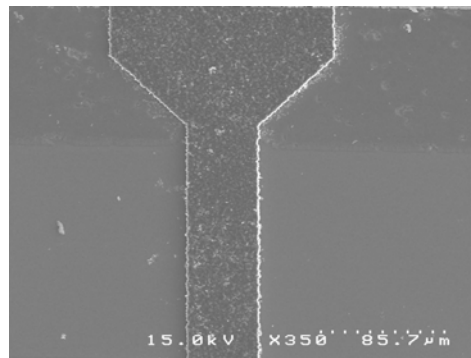
Figure 7.3 - 8   Good delineation for resistor in the same process.

A method of characterization has been developed to enable accurate and reliable data collection that would allow proper characterization of the device. Earlier characterization had anomalous spikes which might have been caused by the power supply. A way to negate this would be by building a buffer circuit that will smooth out any surges or dips from the power source. A prototype circuit was built and tested and further work would have been appropriate to complete this. In addition, a method for more accurate temperature measurement is in order. The current temperature probes are too far from the resistors to provide the best reading of their temperature. Ideally a remote temperature sensing device should be used, but there is no such equipment yet forthcoming.

As regards filtering the input signal, the presence of a ripple in the output signals is believed to originate from the input signal and not caused by the diamond resistors. A new interface for the data acquisition board was built to enable the reading of the input

voltage and output current as well as measure the light intensity from the photodiode in a synchronized manner. The voltage and current readings would be obtained synchronously in real time. A signal isolator would be used to provide more precise input data with a clearer input signal, (Singh J. (1995), 7.4-37). The Data Acquisition (DAQ) software would need to be reworked to be more intuitive towards this specific environment. The power supply input would be tested and characterized to eliminate the ripple that was present in the output signal. Filtering circuitry may be necessary to isolate the ripple that is believed to originate from the power supply hardware as described previously, Figures 7.3-4 and 7.3-5.

7.3.4 Conclusions

Final efforts on this project concentrated on fabricating more resistor test structures for availability and as well as preparing the characterization equipment and methods. The availability of fully optimized resistors in each of the targeted dimension will produce results that highlight the true capabilities of the freestanding diamond resistors. This work would lead to accurate data of the thermal behavior of free standing diamond resistors. The data that has been obtained points to the superiority of diamond resistors over other materials, especially for micro-thermal source purposes.

7.4 References

1. Abeles, M., Quantification, smoothing, and confidence limits for single-units' histograms., J Neurosci Methods. 5:317-325, 1982.
2. Aertsen AMHJ, Gerstein G.L., Habib M.K. & Palm G. Dynamics of neuronal firing correlation: Modulation of "effective connectivity". J. Neurophysiol., 61:900-917, 1989.
3. Attwell D., Laughlin S.B. An energy budget for signaling in the grey matter of the brain., J Cereb Blood Flow Metab. 2001 Oct;21(10):1133-45.
4. Baddeley R., Abbott L.F., Booth M.C., Sengpiel F., Freeman T., Wakeman E.A., and Rolls E.T. Responses of neurons in primary and inferior temporal visual cortices to
5. Bair W., Zohary E., Newsome W.T. Correlated firing in macaque visual area MT: time scales and relationship to behavior. J. Neurosci. 21:1676-1697, 2001.
6. Barlow H.B. Possible principles underlying the transformation of sensory messages. In Sensory Communication, ed. WA Rosenblith, Cambridge, MA: MIT Press, 217 234, 1961.
7. Baum E.B., Moody J., and Wilczek F. Internal representations for associative memory. Biol. Cybern. 59:217-228, 1988.
8. Bell A.J., Sejnowski.T.J., The "independent components" of natural scenes are edge filters. Vision Res. 1997 Dec;37(23):3327-38.
9. Brody C.D. Disambiguating different covariation types. Neural Comput. 11:1527-1535, 1999a.
10. Brody C.D. Correlations without synchrony. Neural Comput. 11:1537-1551, 1999b.
11. Challis R.E. & Kitney R.I. Biomedical signal processing (in four parts). Part 3. The power spectrum and coherence function. Med Biol Eng Comput. 29:225-41, 1991.
12. Eggermont J.J. Neural interaction in cat primary auditory cortex. Dependence on recording depth, electrode separation, and age. J. Neurophysiol. 68:1216-1228, 1992.

13. Field D.J. Relations between the statistics of natural images and the response properties of cortical cells. J. Opt. Soc. Amer. 4:2379-2394, 1987.

14. Field D.J. What the statistics of natural images tell us about visual coding. Proc. SPIE. 1077:269-276, 1989.

15. Field D.J., Hayes A., and Hess R.F. Contour integration by the human visual system: evidence for a local "association field". Vision Res. 33:173-193, 1993.

16. Field D.J. What is the goal of sensory coding? Neural Comp. 6:559-601, 1994.

17. Guo K., Robertson R.G., Mohamoodi S., and Young M.P. Centre-surround interactions in response to natural scene stimulation in the primary visual cortex. Eur. J. Neurosci. 21:536-548, 2005.

18. Hess R.F., Hayes A & Field D.J. Contour integration and cortical processing. J Physiol Paris. 97:105-119, 2003.

19. Hirabayashi T & Miyashita Y. Dynamically modulated spike correlation in monkey inferior temporal cortex depending on the feature configuration within a whole object. J Neurosci. 25:10299-10307, 2005.

20. Hoyer P.O. and Hyvarinen A. Independent component analysis applied to feature extraction from colour and stereo images. Network: Computation in Neural Systems. 11(3):191-210, 2000.

21. Hoyer P.O. and Hyvarinen A. A multi-layer sparse coding network learns contour coding from natural images. Vision Res. 42(12):1593-1605, 2002.

22 . Ito H & Tsuji S. Model dependence in quantification of spike interdependence by joint peri-stimulus time histogram. Neural Comput. 12:195-217, 2000.

23. Kersten D. Predictability and redundancy of natural images. J. Opt. Soc. Am. A 4:2395 2400, 1987.

24. Kohn A. & Smith M.A. Stimulus dependence of neuronal correlation in primary visual cortex of the macaque. J. Neurosci. 25:3661-3673, 2005.

25. Lennie P. The cost of cortical computation. Curr. Biol. 13:493-497, 2003.

26. Leonardo A. Degenerate coding in neural systems. J Comp Physiol A Neuroethol Sens Neural Behav Physiol. 191:995-1010, 2005.

27. M. C. Granger, M. Witek, J. Xu, J. Wang, M. Hupert, A. Hanks, M. D. Koppang, J. E. Butler, G. Lucazeau, M. Mermoux, J. W. Strojek, G. M. Swain, Anal. Chem. 72 (2000) 3793 [3]

28. Olshausen B.A. and Field D.J. Emergence of simple-cell receptive field properties by learning a sparse code for natural images. Nature 381:607 609, 1996.

29. Olshausen B.A. and Field D.J. Sparse coding with an overcomplete basis set: a strategy employed by V1? Vision Res. 37:3311-3325, 1997.

30. Palm G. On associative memory. Biol. Cybern. 36:19-31, 1980.

31. Rolls E.T. & Tovee M.J. Sparseness of the neuronal representation of stimuli in the primate temporal visual cortex. J Neurophysiol. 73:713-726, 1995

32. Samonds J.M., Allison J.D., Brown H.A. & Bonds A.B. Cooperation between Area 17 neuron pairs enhances fine discrimination of orientation. J Neurosci. 23:2416-2425, 2003.

33. Samonds J.M. & Bonds A.B. From another angle: Differences in cortical coding between fine and coarse discrimination of orientation. J. Neurophysiol. 91:1193-1202, 2004a.

34. Samonds J.M., Zhou Z, Bernard M.R. & Bonds A.B. Synchronous Activity in Cat Visual Cortex Encodes Collinear and Cocircular Contours. J. Neurophysiol. 95:2602-2616, 2006.

35. Shadlen M.N .and Newsome W.T. The variable discharge of cortical neurons: implications for connectivity, computation, and information coding. J Neurosci. 18:3870-3896, 1998.

36. Simoncelli E.P. Vision and the statistics of the visual environment. Curr. Opin. Neurobiol. 13:144-149, 2003.

37. Singh J., Semiconductor Optoelelectronics, McGraw-Hill, 1995

38. Smyth D., Willmore B, Baker G.E., Thompson I.D. & Tolhurst D.J. The receptive-field organization of simple cells in primary visual cortex of ferrets under natural scene stimulation. J Neurosci. 23:4746-4759. 2003

39. Ts'o D.Y., Gilbert C.D. & Wiesel.T.N. Relationships between horizontal interactions and functional architecture in cat striate cortex as revealed by cross-correlation analysis. J. Neurosci. 6:1160-1170, 1986.

40. van Hateren J.H., Ruderman D.L. Independent component analysis of natural image sequences yields spatio-temporal filters similar to simple cells in primary visual cortex. Proc Biol Sci. 1998 Dec 7;265(1412):2315-20.

41. van Hateren J.H., van der Schaaf A. Independent component filters of natural images compared with simple cells in primary visual cortex. Proc Biol Sci. 1998 Mar 7;265(1394):359-66.

42. Vinje W.E. and Gallant J.L. Sparse coding and decorrelation in primary visual cortex during natural vision. Science 287:1273 1276, 2000.

43. Vinje W.E. and Gallant J.L. Natural stimulation of the nonclassical receptive field increases information transmission efficiency in V1. J. Neurosci. 22:2904-2915, 2002.

44. Weliky M., Fiser J., Hunt R.H., and Wagner D.N. Coding of natural scenes in primary visual cortex. Neuron. 37:703-718, 2003.

45. Willmore B. and Tolhurst D.J.. Characterizing the sparseness of neural codes. Network 12:255-270, 2001.

46. Willmore B., Watters P.A. and Tolhurst D.J A comparison of natural-image-based models of simple-cell coding. Perception 29:1017-1040, 2000.

47. Willshaw D.J., Buneman O.P., Longuet-Higgins H.C. Non-holographic associative memory. Nature. 1969 Jun 7;222(5197):960-2.

48. Xu J., G. M. Swain, Anal. Chem. 70 (1998) 1502. [2]

49. Xu J., M. C. Granger, Q. Chen, J. W. Strojek, T. E. Lister, G. M. Swain, Anal. Chem. 69 (1997) 591A. [1] .

50. Zetsche C. Sparse coding: The link between low level vision and associative memory. In Parallel Processing in Neural Systems and Computers, R. Eckmiller, G. Hartmann, and G. Hauske, eds. North-Holland, Amsterdam, 1990.

8.0 Appendices

8.1 Appendix A

8.1.1

**Ontology Integration within a Service-Oriented Architecture for
Expert System Applications using Sensor Networks**

J. Caleb Goodwin and David J. Russomanno
Department of Electrical and Computer Engineering
The University of Memphis
Memphis, TN 38152 USA

Primary Contact:
David J. Russomanno
Herff College of Engineering
Department of Electrical and Computer Engineering
206 Engineering Science
The University of Memphis
Memphis, TN 38152 USA
Phone: 901-678-3253
Fax: 901-678-5469
E-mail : drussmnn@memphis.edu

Abstract:

Keywords:

Sensor ontology, Web services, Semantic Web, Service-oriented architecture, UDDI

1. Introduction

As sensor networks and stand-alone sensor deployments become more ubiquitous, expert system applications that use sensor data will become common in a variety of tasks, including natural disaster response and mitigation synthesis, persistent surveillance, including monitoring potential terrorist and criminal activity, military planning and battlefield management, as well as other applications in which sensors must be discovered, evaluated, and controlled. For example, the United States Department of Defense, Department of Homeland Security, NATO, and other government agencies and alliances are establishing ubiquitous, heterogeneous sensing environments due to the requirement of monitoring and detecting events of interest, as well as predicting future system states. Data obtained from a variety of sensors, such as acoustic sensors, can result in an expert system detecting a possible event of interest and initiating subsequent problem-solving activities. Integration and fusion of sensor data, such as visible and infrared images complemented by data from acoustic, radiation, vibration sensors, etc., may reveal further knowledge about items of interest resulting in an increased confidence in a given hypothesis or the pruning of a set of competing hypotheses.

Opportunistic composition of sensor services and dynamic fusion of data obtained from a variety of heterogeneous sensors will greatly benefit from formal knowledge representation techniques and service-oriented problem-solving models. Such models, which facilitate semantic markup of sensor metadata and the sensor data itself, along with a sensor service registry, will support the discovery of sensor services satisfying the constraints specified within expert system applications. Increasing numbers of sensors will be discoverable via the Web, making the use of sensor Web services critical in expert system applications.

The current standard specified by the Organization for the Advancement of Structured Information Standards (OASIS) for service discovery within a service-oriented architecture (SOA) is Universal Description, Discovery, and Integration (UDDI) (Clement et al., 2004). Despite wide commercial acceptance, the UDDI specification does not adequately facilitate autonomous discovery and interoperation of disparate Web services via queries that use semantic data models.

The search capability that conforms to the UDDI specification lacks adequate support for semantic descriptions of Web services, which is integral in the dynamic discovery and composition process (Paolucci et al., 2002a; Paolucci et al., 2002b; Sivashanmugam et al., 2003; Akkiraju et al., 2003; Srinivasan et al., 2004; Luo et al., 2005a; Luo et al., 2005b; Akkiraju et al., 2007; Goodwin et al., 2007). UDDI's search capability is syntax-based and relies solely on the Extensible Markup Language (XML), which enables syntactic, but not semantic query without additional knowledge layers,

124

such as those offered by the Semantic Web infrastructure. Syntax-based matching alone lends itself to application-specific software development where reuse of Web services by others is difficult. For example, the syntactic description of a Web service's output could be syntactically different than the input of a candidate service for composition, but the two services may be semantically compatible. However, an expert system application would not be able to discern the similarity without semantic descriptions and a plausible composition may be missed. The shortcomings of UDDI's syntax-based search capabilities are two-fold: i) there is no guarantee that the returned sensor service is correct even if it matches the keyword search due to the lack of semantics; and ii) opportunities to locate an appropriate sensor service are frequently overlooked. For instance, keyword searching for an infrared camera does not return the service entry for a mid-wave camera even though the mid-wave camera type is a specialization of the infrared camera type.

Search processes that utilize semantics facilitate generalization and specialization of queries that search for sensors of interest through the understanding of the relationships between ontological objects and services. For instance, semantic understanding of sensor performance capabilities, operational capabilities, and physical properties may aid in the discovery of sensor services through generalization or specialization of the initial query. The investment in UDDI makes the augmentation of semantic search capabilities within its existing infrastructure of great interest to those developing government and commercial applications.

The remainder of this paper describes an architecture and initial prototype for augmenting UDDI with semantics for the search of sensor services and is organized as follows: Section 2 provides an overview of the technologies and infrastructure leveraged in this paper, including the Semantic Web, service-oriented architecture (SOA), and current approaches for service discovery using semantics. Section 3 presents the SOA intended to support expert system applications. Section 4 discusses the implementation of the sensor SOA prototype. Section 5 summarizes the work presented in the paper and provides direction for future research.

2.0 Background

The sensor service architecture described in this paper leverages Semantic Web infrastructure, Web services, and service-oriented technologies. OntoSensor is a Semantic Web- compliant ontology developed using Protégé 2000 (Noy et al., 2002) for describing sensors for autonomous processing by expert system applications (Russomanno et al., 2005a, Russomanno et al., 2005b, Russomanno & Goodwin, 2007). OntoSensor remains a work in progress that is undergoing significant revision, but it does capture a subset of sensor attributes and operational parameters to support the prototype environment. A semantic matchmaker for OntoSensor was developed to aid in sensor service discovery. OntoSensor enhances the matching process of finding the appropriate sensor services to satisfy a subgoal or query within an expert system application. In the prototype, OntoSensor's taxonomic hierarchy is used to determine the type of a specific sensor instance that is listed in a service registry or to find generalized or specialized results that may partially match a given query to locate sensors having specific properties.

The matchmaker enhances the initial syntax-based UDDI search by extracting the portion of semantic metadata from OntoSensor that is pertinent to satisfying the query and storing the metadata in UDDI. If the expert system's query results in hits, that is, sensor services that match an expert system's particular subgoal are directly specified in the UDDI registry, then, these sensors' descriptions are returned; otherwise, the UDDI sensor service interface will attempt to use semantic processing via OntoSensor that may semantically match (to some degree) the expert system's query. If such matches are found, then, the ontological information from OntoSensor pertinent to the specific sensor facts that are published in the registry is inserted/updated into the UDDI tModels, much like a conventional cache, for use in subsequent queries.

Preliminary aspects of the development of the ontology-based SOA have been presented by Goodwin et al. (Goodwin et al., 2007; Goodwin & Russomanno, 2006; Russomanno & Goodwin, 2007); however, these work-in-progress publications do not contain the details presented in this paper.

2.1 Semantic Web

The Semantic Web effort seeks to establish a collaborative Web through sharing and reuse of machine-interpretable conceptualizations of knowledge that can be used by intelligent computer systems, including expert systems. The Semantic Web effort focuses on defining and moving ontologies and knowledge representation standards from traditional stand-alone systems to the highly-distributed World Wide Web (Berners-Lee et al., 2001, Fensel et al., 2003; McGuiness, 2003).

XML provides the syntax to describe documents, objects, attributes, and other resources on the Web. However, the context of the document is primarily intended for human interpretation, making interoperability difficult, since the meaning of the XML tags may only be known by the developer or may be ambiguous to others, particularly computer algorithms, without formal semantics. The Resource Description Framework (RDF) is an XML-based language to describe the XML tags providing an elementary, machine-interpretable knowledge representation and metadata for the Web (Brickley & Guha, 2000). Resource Description Framework Schema (RDFS) extends the capabilities of RDF by adding a vocabulary to describe properties and inheritance relations. The Web Ontology Language (OWL) (Smith et al., 2003) extends RDFS by adding the constructs to define properties, such as cardinality constraints and disjoint classes, and other semantic constructs. OntoSensor was implemented using OWL. RDF, RDFS, and OWL are the immediate layers above XML and comprise a portion of the Semantic Web infrastructure.

2.2 Service-oriented architecture (SOA)

Service-oriented architectures (SOAs) strive to establish principles and standards for description, discovery, connection, and communication of Web services (Singh & Huhns, 2005). Web services are distributed, functional units accessible via a network environment that are modular and self-describing. A Web service is identified by a universal resource identifier (URI) and contains an interface description describing the capabilities of the module, communication protocol, and port locations. Success of the SOA depends on communication standards for discovery and invocation of the

distributed applications. Furthermore, a framework is required for publishing and describing Web services so that applications can locate the requisite services.

UDDI is the current OASIS standard for Web service discovery. Figure 1 depicts a generic model for an SOA using UDDI which provides standards for description, discovery, connection, and communication between Web services. The architecture consists of the following: i) service provider that registers descriptions of services; ii) broker that maintains a registry of services and providers; and iii) service requestors who search the registry for available services.
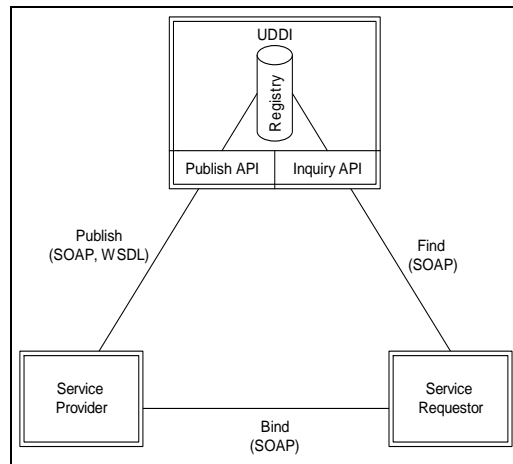

Figure 1. Generic model for SOA

The following description of the UDDI specification follows closely from (Singh & Huhns, 2005). UDDI is an on-line registry where service providers can register Web services providing descriptions that can later be discovered by service requestors. UDDI provides an application programmer's interface (API) to query and publish Web services using Simple Object Access Protocol (SOAP) for messages. Web Service Description Language (WSDL) provides XML descriptions for inputs, outputs, bindings, etc. The WSDL service descriptions are mapped to the UDDI data structures where they are later searched when fulfilling service requests. UDDI consists of two APIs: inquiry and publish. The APIs are a series of predefined functions that accept SOAP messages as input and return SOAP messages as output. The APIs are used to search and publish services and descriptions of the services in the UDDI repository.

UDDI's core XML data structures consist of five objects: publisherAssertion, businessEntity, businessService, bindingTemplate, and tModel. The businessEntity object contains information pertaining to a service provider, such as contact information, alias names, etc. A service provider is required to register in UDDI before it can provide service advertisements. The businessService object contains metadata describing the capabilities of the service and a key linking the service to the service provider. The bindingTemplate object provides the service requestor with the ability to access and invoke the Web service. The publisherAssertion object allows service providers to form associative links. For instance, a company may have many departmental organizations

127

that provide different Web services. Each of the data objects contains text fields and technical models (tModels) for inclusion of additional metadata. The tModel objects permit external links to resources outside of the UDDI framework providing overall extensibility for the system.

2.3 Approaches to augment UDDI with semantics

This section briefly outlines some of the representative approaches for augmenting UDDI with semantic search capabilities. The focus is primarily on the approaches presented by Luo et al. (Luo et al., 2005a; Luo et al., 2005b) and Akkiraju et al. (Akkiraju et al., 2007) since these applications were the most influential in the development of the sensor-based architecture presented in this paper.

A rough classification of representative approaches for augmenting UDDI with semantic capabilities is shown in Figure 2. This particular classification is based upon where the knowledge for semantic processing is stored, that is, internal semantic schema within UDDI tModels or external semantic schema.
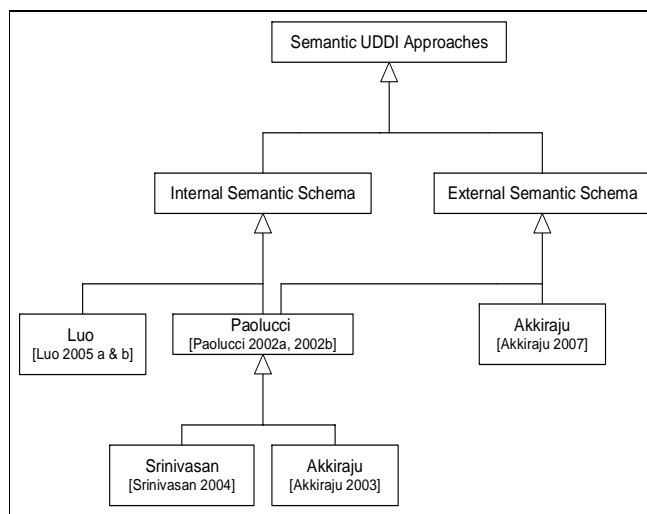
Figure 2. Approaches for augmenting UDDI with semantics

Approaches that include an internal semantic schema within UDDI must load semantic content into the UDDI registry via tModels, which often results in the loss of semantics. After the development of a matchmaker to process the internal schema, then, the tModels can be traversed to attempt to satisfy a query. Additional knowledge and data may be inserted into or deleted from the tModels. The external matchmaker resides outside of the UDDI registry and is invoked when a request is received. The semantic matcher may provide query expansion and generalization/specialization to locate semantically similar services.

Referencing external schema also involves the limited use of tModels. When a provider registers a particular service an accompanying reference is inserted in the tModel so that the semantic matcher can access the external semantic data model for subsequent processing. However, in this approach, the tModel is used exclusively to hold

128

the reference to the external semantic data model and does not hold the model, knowledge, or data itself.

UDDI API modifications are often coupled with an internal semantic schema, external matchmaker, or external semantic schema for query enhancement. Such modifications, such as (Sivashanmugam et al., 2003), allow for the extension of the existing search capabilities and the semantic registration of services via custom APIs. The disadvantages of such custom approaches are that they do not maintain the UDDI standard-API, possibly limiting reuse in a variety of applications.

The Luo et al. (Luo et al., 2005a, Luo et al., 2005b) approach bulk loads entire ontologies into the UDDI registry via extensive use of tModels. An ontology aware matchmaker can then make use of the ontology stored in UDDI, as well as service instances that reference the stored ontology. The OWL-S service description for a new service maps to the UDDI data model objects. The data objects in the tModels reference the ontology, which was bulk loaded into UDDI. The realization of the system is analogous to developing an object-oriented conceptual model, but losing semantics when implementing the conceptual design in a relational database. For instance, OWL language constructs such as *subPropertyOf*, *Class*, and *subClassOf* are retained, but the semantics entailed from *minCardinality*, *maxCardinality*, and *FunctionalProperty* are lost. Furthermore, the reliance upon the elementary query capabilities of UDDI will further limit the inference capabilities of an expert system application.

The architecture developed by Akkiraju et al., 2007 uses a variety of techniques; hence, it is classified as an approach that uses multiple inheritance as shown in Figure 2. This approach is composed of a generic Web service proxy, constraint checker, dynamic binder and invoker, and semantic UDDI infrastructure. The generic Web service proxy receives service requests. The generic Web service proxy can be viewed as the moderator among semantic UDDI, constraint checker, and the dynamic binder and invoker. The generic Web service proxy sends a request to the UDDI registry to find available services based upon the user query. The UDDI registry invokes a semantic matching engine and returns the set of available services to the proxy server. The generic Web service proxy then invokes the constraint checker which takes the set of candidate services and checks for compatibility between the services and ensures that they meet the service constraints of the initial query. Finally, the generic Web service proxy invokes the dynamic binder and invoker. The dynamic binder orchestrates the execution chain among the candidate Web services and then the invoker invokes the chain to satisfy a particular goal. TModels are used to reference additional external RDF semantic information, such as ontologies or instance-specific data. The architecture allows for the registry use with or without semantic matching depending on the specification of the service requestor. The semantic matcher is registered in the UDDI registry as a service. The matcher is invoked dynamically based upon its specialized domain allowing for selection of the best matcher given the query criteria. The matchmaker architecture is viewed as a service so the inference capabilities are constricted only by the implementation of the matchmaker.

3.0 Prototype Overview

This section presents the design of an SOA that can be used to support expert system applications. Section 3.1 provides additional details about OntoSensor, which is used in the prototype for knowledge base support for discovering sensor services. Section 3.2 presents the design of the sensor discovery architecture. Section 3.3 discusses the use of the sensor registry knowledge base as a cache whereby a subset of OntoSensor pertinent for satisfying a query is stored in the registry's tModels to aid in satisfying subsequent queries.

3.1 OntoSensor

Ontological engineering focuses on developing shared, machine-readable conceptualizations of knowledge discernable by intelligent computer systems (Lenat & Guha, 1989; Skuce & Monarch, 1990; Uschold & Gruninger, 1996; Chandrasekaran et al., 1999). For purposes of this paper, a conceptualization of declarative knowledge as described by Genesereth and Nilsson (Genesereth & Nilsson, 1987) defines an ontology and it includes, but is not necessarily limited to, the following as described in (Russomanno et al., 2005a; Russomanno et al., 2005b):

- the classes to which objects belong (e.g., sensor types)
- the class hierarchy or taxonomic structure (e.g., set of radiant sensors is a subset of all sensors)
- the relational basis set among the classes (e.g., a sensing element is part of a sensor)
- the functional basis set among the objects (e.g., bandwidth('JERS SAR') = 1.275 GHz)
- the capability for executing special programs or procedures for evaluating the truth of literals or other properties (e.g., procedural attachment)

Once a basic ontology has been defined, a language, which can be unambiguously interpreted by a computer, can be used to express knowledge using concepts defined in the ontology. OntoSensor is a Semantic Web-compatible ontology initially developed using Protégé 2000 (Stanford, 2004) and is exportable to OWL. OntoSensor references and extends the IEEE Suggested Upper Merged Ontology (SUMO) (Niles & Pease, 2001), which defines general concepts and associations. OntoSensor was influenced in-part by a preliminary definition of SensorML (Botts et al., 2004), which provides a framework consisting of a series of UML class diagrams with associations realized in XML for describing sensors. OntoSensor deviates from SensorML in that SensorML lacks the semantic richness provided by ontologies, such as axiomatic-grounded terms, which may be required for automated data fusion and inference in a distributed sensing environment.

OntoSensor includes knowledge models for a variety of data acquisition boards, sensors, and processor/radio units common in commercial wireless sensing environments, as well as preliminary definitions for a variety of wired imaging sensors, such as those provided by Sony and FLIR (forward looking infrared system) Systems. OntoSensor contains a taxonomic hierarchy of sensor classes and the knowledge model for a given sensor type includes metadata, such as sensitivity and other performance parameters for the sensing elements, as well as physical characteristics, such as mass, radio frequencies, dimensions, and power supply information for wireless motes. An excerpt of OntoSensor

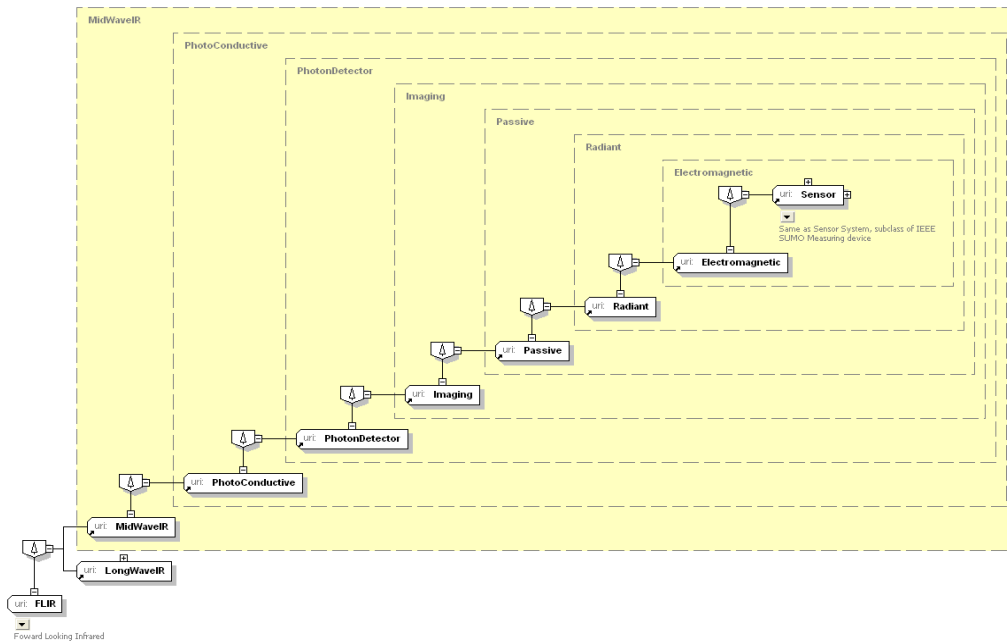showing the taxonomic hierarchy from the class FLIR up through the Sensor class is shown in Figure 3.

Figure 3. Excerpt of OntoSensor

3.2 Overview of sensor service-oriented architecture (SOA)

Service-oriented architecture (SOA) provides the standard communication protocol, as well as methodology to discover, invoke, and publish sensor Web services. As shown in Figure 4, the prototype realization of SOA creates a sensor service provider that includes the base stations that serve as a connectivity points between the sensor service requestor and the physical sensors. The sensor service provider registers its respective services with a broker, aggregates and stores data from its respective sensor deployments, and processes queries either by retrieving archived data or tasking the deployed sensors in its network. Stand-alone sensors may also serve as providers.
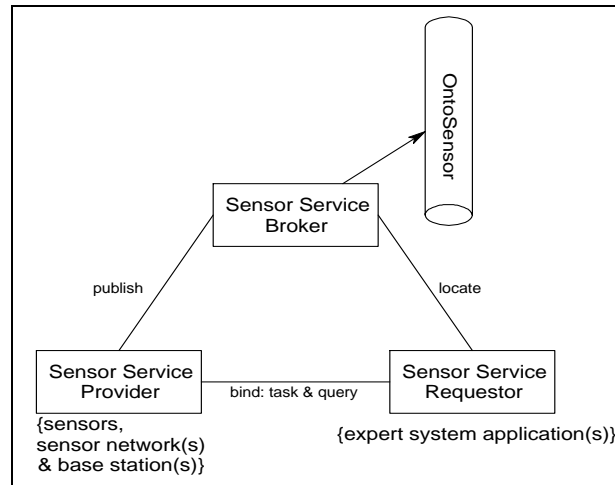
Figure 4. Generic model for sensor services

The prototype environment is comprised of two computers that serve as base stations and store the data collected from the MIB510 and MIB520 network gateways provided by Crossbow (Crossbow, 2006). The base stations register their respective services with the sensor service broker. The sensor service broker facilitates semantic discovery of the registered services. Each base station receives data from a sensor network. The wireless sensors form ad-hoc communication links to route the collected data back to the base station. The base stations run Crossbow's MoteView application to retrieve data from the network gateways and the data is stored in a PostGRE database. In addition, each base station executes custom software that extracts sensor data and metadata into OWL repositories that commit to OntoSensor. The software is a preliminary implementation of a Web service that is evoked at the base stations for selectively storing sensor data that references OntoSensor within the networked environment.

Successful reference of OntoSensor requires a priori knowledge of the sensor platform class associated with a given node identification number. Later development will circumvent this dependency through custom software development on the processor boards so that they are self describing. The platform class is used as a primary key to retrieve inherited and unique properties defined through constraints in OntoSensor that are exported to OWL.

The base stations also serve as a logical interface for tasking the individual sensors through Web services. Base stations also provide physical storage aggregation nodes for sensor data and metadata that can be used in response to queries by expert system applications or other agents, rather than involving the individual sensor nodes in responding directly to queries. Figure 5 depicts an abridged view of the prototype environment.
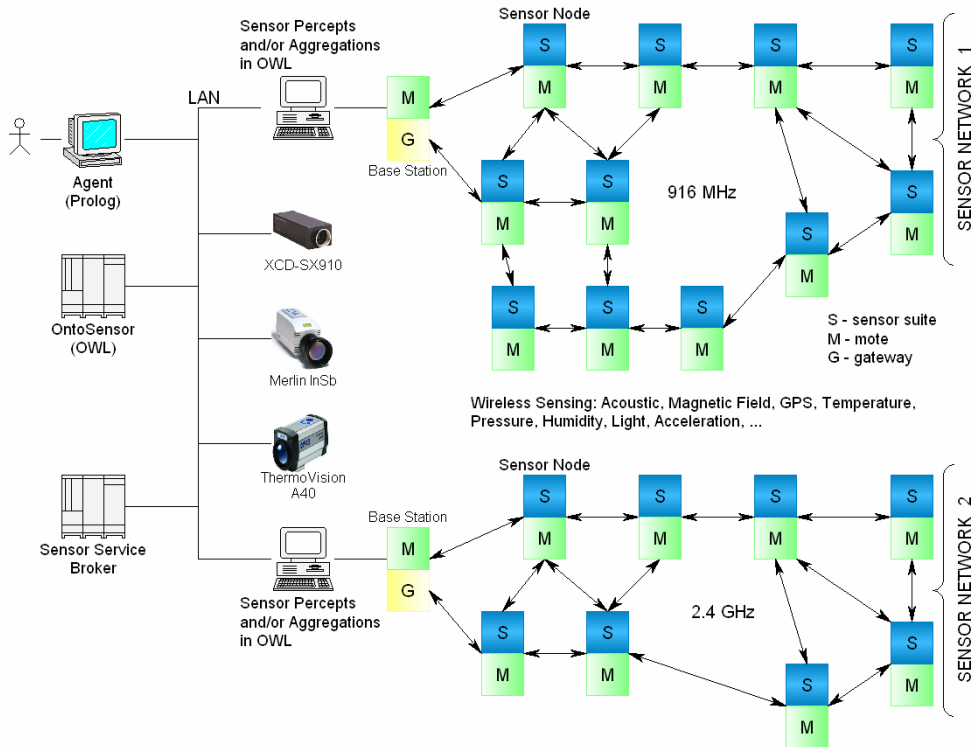
Figure 5. Prototype Environment (Abridged) (Russomanno & Goodwin, 2007)

3.3 Sensor service-oriented architecture (SOA)

The service-oriented architecture (SOA) is composed of three modules; i) sensor service interface, ii) UDDI, and iii) semantic sensor matchmaker. The sensor service interface is a preprocess that can be thought of as a proxy server that routes requests and invokes matchmaking services when needed. The semantic sensor matchmaker is invoked by the sensor service interface, if the service requestor specifies semantic matching and works in conjunction with UDDI to discover sensor services using semantics. The semantic matchmaker has the following capabilities when searching for sensors; i) generalization of sensor types; ii) specialization of sensor types; iii) metadata processing of specific sensor instances; iv) supported application processing; and v) performance property processing.

The overall architecture is shown in Figure 6 and leverages the architecture proposed by Akkiraju et al. (Akkiraju et al., 2007) and allows for maximum inference capabilities

by an expert system, query of instance specific metadata, and the use of multiple matchmakers. The adopted approach avoids precluding various inference capabilities, such as functional properties whose use is limited in (Luo et al., 2005a; Luo et al., 2005b) and provides semantic capabilities beyond input/out generalization as in (Paolucci et al., 2002a; Paolucci et al., 2002b). Furthermore, the architecture allows for domain-specific matchmakers and use of external semantic schema which is required for sensor service discovery not present in some of the proposed architectures (Paolucci et al., 2002a; Paolucci et al., 2002b; Sivashanmugam et al., 2003; Akkiraju et al., 2003; Srinivasan et al., 2004; Luo et al., 2005a; Luo et al., 2005b).

Figure 6. Sensor discovery service-oriented architecture (Goodwin et al., 2007)

The UDDI sensor service interface facilitates communication among the agent or expert system application, matchmaker, and registry. The sensor service interface allows for extension of the UDDI API while keeping the standard API intact. If the expert system application or agent specifies semantic matching, the UDDI registry is searched to discover the external ontologies associated with the registered services. The sensor service interface then searches the UDDI registry to find matchmakers that provide services within the domain of a given ontology. If a matchmaker is discovered, the sensor service interface invokes the matchmaker which performs semantic matching on the query in conjunction with the registered services in the UDDI registry.

A semantic sensor matchmaker, utilizing OntoSensor, aids in the discovery of sensors and sensor Web services. The semantic sensor matchmaker can be viewed as an instance of a matchmaker Web service. Regarding matchmakers as instances allows for future addition of sensor matchmakers that can be specialized within a domain of sensor types or composition of sensor services. For example, sensor Web services can be composed of specific algorithms that take raw sensor data as input and provide some service on the data, such as noise reduction or a classification task on the data that may be directly used by the expert system application or serve as input to another service. This

framework allows for specialized matchmakers that can work collaboratively to locate the appropriate sensors and other algorithms capable of processing the data from the given sensors, to compose these services, and to satisfy a high-level goal of an expert system application.

It is a goal that OntoSensor will ultimately contain the majority of the semantic data model required for search for several types of sensors. However, specific sensor instances may contain properties that the matchmaker must load at query time. For instance, the geo-location, orientation, and lens type will vary among the various instances of thermal infrared imaging cameras. An external reference is adopted in the prototype to provide external links to instance specific data. The *DescribedUsing* tModel allows for instances to reference additional semantic schema or instance data by including a pointer to the location of the external description. The external description is then loaded by the matchmaker when needed.

A robust matchmaker is required for sensor service discovery and is beyond the scope of input/output matching or simple capability matching. Input/output matching is crucial in service compositions where a binding may be missed or mistaken for compatibility due to the lack of semantics. However, sensor Web services require support for queries, such as supported applications, day/night operation, and instance specific properties such as lens type, resolution, geo-location, etc. For example, the semantic sensor matchmaker receives the following request: "Infrared_Camera location=xxx." The matchmaker first searches the UDDI to see if there are any instances of *Infrared_Camera*. In this scenario, the UDDI does not contain any entries. The matchmaker then finds all subclasses of *Infrared_Camera* and searches the UDDI again. *FLIR_ThermaCam* is found in the registry which is a subclass of *Infrared_Camera*. The matchmaker then obtains the external link to the instance specific data and determines that the camera is in location "xxx." The bindings of the services are then returned to the service requestor.

3.4 UDDI tModel as cache

This section describes using the UDDI tModel as a form of cache to enhance syntax-based search. This section follows closely from (Goodwin et al., 2007). A portion of the UDDI model shown in Figure 6 can be viewed as a cache. If the service requester's query is satisfied directly by the service specifications in the UDDI repository, then, the sensors' bindings are returned; otherwise the sensor matchmaker is invoked to find generalizations or specializations that are semantically similar to the initial query. Ontological knowledge pertinent to the semantically similar sensor is updated/inserted into the UDDI tModels. The functionality is similar to a conventional cache whereby subsequent queries can be satisfied using the registry without the aid of the matchmaker. The sequence diagram in Figure 7 depicts the use of the UDDI repository as a form of cache in the implemented prototype to satisfy a query for a sensor with the specified capability.

The approach does not seek to seamlessly integrate or bulk load OntoSensor into the UDDI tModel, but it provides a means to enhance the syntactic matching initially used for queries. For example, in Figure 7 the request for a sensor service with capability Y initially fails without matchmaking being specified in the query, but it is satisfied using semantic matching in conjunction with the knowledge about sensors in Figure 8. The

matchmaker uses the knowledge to deduce that Sensor X is a subclass of Sensor Y; therefore, it also has capability Y. A subsequent analogous query succeeds without matchmaking due to the explicit assertion of these deduced facts in the tModel in UDDI.
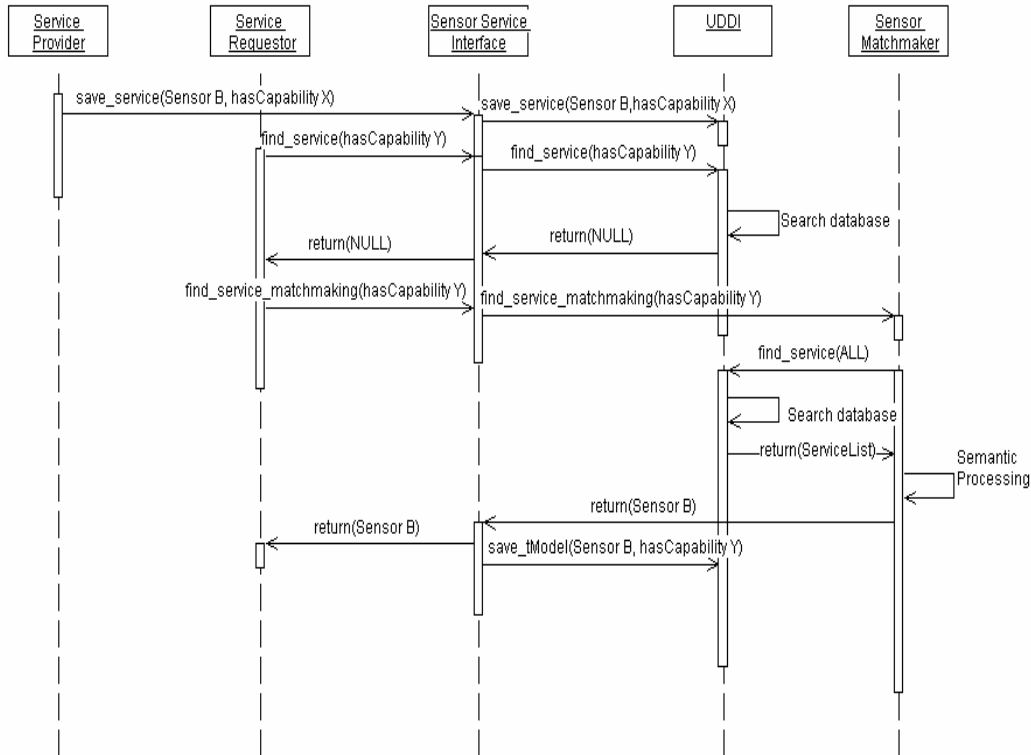

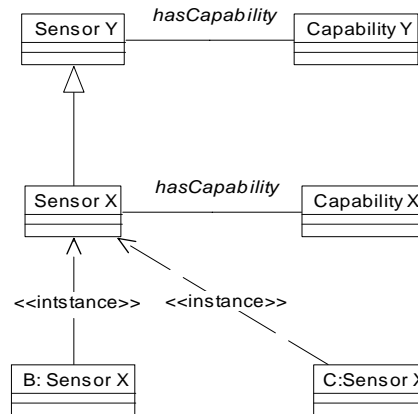**Figure 7.** Sequence diagram for matchmaking search (Goodwin et al., 2007)

Figure 8. Excerpt of ontological sensor knowledge (Goodwin et al., 2007)

136

Saving the relevant portion of the semantic data model in the UDDI tModels after matchmaking using an external ontology can be thought of as a deep knowledge approach that supports subsequent shallow queries using a heuristic approach. Consider the following events in which steps 1-8 correspond with Figure 7:

1. A service provider registers sensor B with capability X.
2. A service requestor queries for a sensor with capability Y.
3. UDDI is searched and no hits are found for the request.
4. A service requestor requests matchmaking for a sensor with capability Y.
5. The matchmaker discovers that sensor B is an instance of Sensor X which has capability Y.
6. UDDI is searched for sensor B and it is found.
7. The bindings for sensor B are returned to the requestor.
8. Data for sensor B is saved in the UDDI tModel so that it is explicit that it has capability Y.
9. A service provider registers sensor C with capability X.
10. A service requestor queries for a sensor with capability Y.
11. Sensor B is found in UDDI and returned to the service requestor (sensor C is not found).

In response to the query in step 10, sensor B is found in step 11 through syntax-based search via the UDDI tModel since the explicit knowledge needed to satisfy the query was loaded into "cache" from a prior deep query (step 1-8). In step 11, sensor C is not found in the UDDI repository by the service requestor's initial syntax-based query (step 10). On initial inspection, this may appear to be an oversight. However, the returned services can be evaluated by the requestor to determine if they fulfill the needs of the expert system application or agent. If the returned services are not satisfactory, the agent will query again by specifying semantic matching. For example, a subsequent deeper probe, as shown by operation N in Figure 9 would discover that sensor C has capability Y. The process is analogous to using a set of compiled heuristics first (that is, the explicit facts in the UDDI tModel repository) then, falling back on deeper knowledge (the sensor ontology), if the heuristics do not provide an acceptable solution.
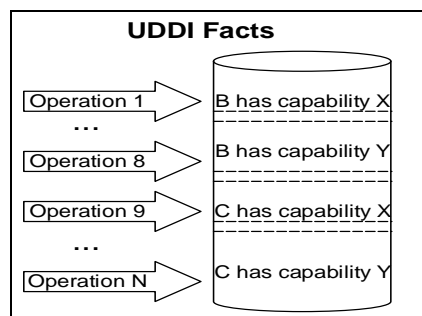

Figure 9. UDDI repository (Goodwin et al., 2007)

4.0 Prototype Implementation

This section provides a detailed review of the design and implementation of the sensor service-oriented prototype. This architecture includes the Prolog implementation of a UDDI- inspired repository (referred to as the Prolog UDDI registry), sensor matchmaker, and sensor service interface.

4.1 Prolog UDDI schema

The conceptual model developed for the UDDI prototype, which was implemented using Prolog, is shown in Figure 10. This model omits some of the class definitions from the full UDDI-standard specification and focuses on the subset of the model that is pertinent for representing semantic sensor services.

The UDDI conceptual model in Figure 10 is realized using a UML to relational database conversion strategy and implemented using Prolog. The Prolog facts corresponding to a particular functor and arity are analogous to tuples within a given table, while foreign key attributes represent relations between tables. Example Prolog functors include: businessEntity/9 which represents the sensor service provider; businessService/6 which represents the sensor services offered by the provider that are described using the businessService/6 descriptions.
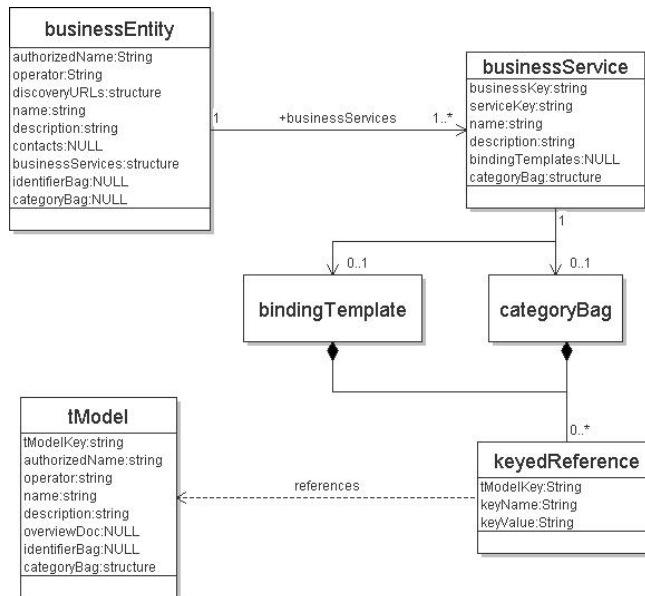

Figure 10. Excerpt of the UDDI conceptual model used in prototype

As an example of the implementation details, Figure 11 is the Prolog schema representing businessService/6. In this schema, Name is the unique key reference to a class that is described in an ontology. The registered service is an instance of a class in the ontology defined by the Name attribute. For example, in Figure 12, the Name attribute has value *MEP410_Platform*, which is an instance of the *MEP410_Platform* class described in OntoSensor. The Name attribute is used when matchmaking is specified to aid in semantic processing. Services provided by a businessEntity/9 are

138

retrieved using the foreign key BusinessKey attribute stored in the businessService/6 fact of a sensor service.

businessService(Name, Description, BindingTemplates, CategoryBag, ServiceKey, BusinessKey).	businessService('MEP410_Platform',_, [['accessPoint', 'URL']], [['describedUsing', 'OntoSensor.owl']], '1', '1').
Figure 11. Prolog businessService schema	**Figure 12.** Prolog businessService fact

The CategoryBag and BindingTemplate attributes represent the categoryBag and bindingTemplate XML structures and are composed of lists containing KeyReference and KeyValue attributes. The CategoryBag attribute is used to provide categorical or descriptive metadata for a service. The BindingTemplate attribute is used to provide metadata for accessing, tasking, and invoking a service. The KeyReference attribute references a domain tModel and is instantiated using the KeyValue attribute. In Figure 12, the KeyReference attribute has the value *describedUsing*, which is instantiated with the KeyValue attribute having value *OntoSensor.owl,* which indicates the businessService is described by OntoSensor. The *describedUsing* tModel is used to link registered services to external knowledge stores. In the prototype implementation, the KeyReference with value *accessPoint* is used to describe the URL for connecting with the sensor service to obtain metadata or to task the service.

4.2 Mapping semantic data models to UDDI data structures

In the UDDI specification, the tModel XML structure is an independent reference table allowing for domain definition and instantiation using the keyedReference structure of the categoryBag (Clement et al., 2004). The categoryBag schema, shown in Figure 13, is composed of references that point to existing tModels via the tModelKey attribute. The tModelKey attribute points to the domain that the KeyValue attribute instantiates. The UDDI repository uses the categoryBag structure to represent shallow taxonomic properties and is used here to store semantic data into the UDDI tModels. Existing approaches use tModels and the categoryBag structure of the tModels to bulk load the entire ontology into a UDDI database (Luo et al., 2005a, Luo et al., 2005b). The approach taken in the implementation of the prototype seeks to enhance subsequent syntactic search after matchmaking by saving metadata in the UDDI tModels and not explicitly loading an entire ontology into the UDDI repository.
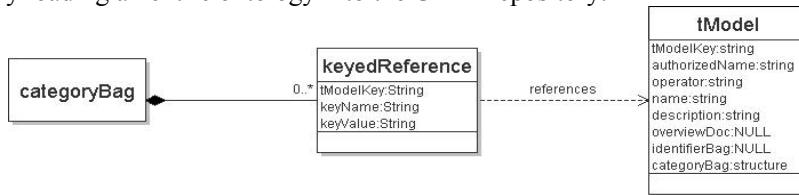

Figure 13. categoryBag schema

TModels are used to describe properties such as inheritance relations, applications, and capabilities. For instance, *subClassOf*, *describedUsing*, and *hasCapability* relations can be represented using tModels with the instantiation being stored in the CategoryBag attribute of a businessService fact. Figure 14 contains an excerpt of a taxonomic relationship in OntoSensor and Figure 15 contains the corresponding OWL export. An instance of a *ThermacamSC500* could be stored as a sensor service in the UDDI registry and is described initially using the Prolog fact businessService('ThermacamSC500', _, _, _, 'AserviceKey', 'AbusinessKey'). The fact contains no knowledge corresponding with the taxonomic hierarchy in Figure 14. Syntax-based queries for sensor service instances that are members of a specialization of *PhotoConductive* or *MidWave* would fail to find instances of *ThemacamSC500* and would require semantic matching to locate such sensors. Storing the taxonomic relationships represented in Figure 14 in UDDI is feasible using the service's categoryBag schema and will enhance syntax-based search.
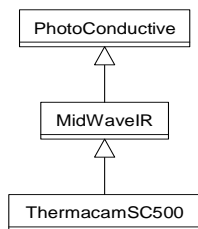

	`<owl:Class rdf:ID=”ThermacamSC500”/>`
	`<rdfs:subClassOf>`
	`  <owl:Class rdf:ID=”MidWaveIR”/>`
	`</rdfs:subClassOf>`
	`<rdfs:subClassOf>`
	`  <owl:Classrdf:ID=”PhotoConductive”/>`
	`</rdfs:subClassOf>`

Figure 14. OntoSensor excerpt	**Figure 15.** OntoSensor OWL excerpt

Mapping the knowledge in Figure 15 into the UDDI repository requires the creation of *subClassOf* and *describedUsing* tModels. Shown in Figures 16 and 18 are the UDDI XML representations of the *describedUsing* and *subClassOf* tModels. Shown in Figures 17 and 19 are the Prolog facts representing the *describedUsing* and *subClassOf* tModels implemented in the prototype.

   The taxonomic hierarchy shown in Figure 14 can be realized using the *subClassOf* tModel along with the *describedUsing* tModel to provide a link to the external ontology. Shown in Figure 20 is the UDDI XML representation of Figure 14 while Figure 21 is the corresponding Prolog implemented in the prototype. The CategoryBag attribute of a sensor service, for example, a deployed instance of the *ThemacamSC500* sensor, references the tModels *subClassOf* and *instanceOf* to capture the taxonomic relationships in Figure 14. Relationships, such as *hasCapability,* are saved using similar tModel structures and corresponding Prolog implementations of the tModels.

`<tModel`
`tModelKey=”uddi:describedUsing”>`
`   <name>describedUsing</name>`
`</tModel>`
	`tModel('describedUsing', _, _, _,`
	`[['describedUsing','URL:OntoSensor.owl']],`
	`Uddi:describedUsing, _, _).`

Figure 16. UDDI *describedUsing* tModel	**Figure 17.** Prolog *describedUsing* tModel fact

`<tModel`
`tModelKey=”uddi:subClassOf”>`
  `<name>subClassOf</name>`
  `<categoryBag>`
  `<KeyedReference=”describedUsing”`
`keyValue=”URL:OntoSensor.owl”>`
  `</categoryBag>`
`</tModel>`
	`tModel(‘subClassOf’, _, _, _,`
	`[[‘describedUsing’,’URL:OntSensor.owl’]],`
	`uddi:subClassOf, _, _).`

Figure 18. UDDI *subClassOf* tModel	**Figure 19.** Prolog *subClassOf* tModel fact

```
<BusinessService>
   <name>ThermacamSC500</name>
<categoryBag>
   <KeyedReference=’describedUsing’
keyValue=”url:OntoSensor.owl”>
   <KeyedReference=’subClassOf’
keyValue=”PhotoConductive”>
   <KeyedReference=’subClassOf’ keyValue=”MidWaveIR”>
   </categoryBag>
```
Figure 20. UDDI businessService tModel

```
businessService(‘ThermacamSC500’, _, _,
   [[‘describedUsing’, ’URL:OntoSensor.owl’],
   [‘subClassOf’, ’PhotoConductive’],
   [‘subClassOf’, ’MidWaveIR’],
 ‘AserviceKey’, ‘AbusinessKey’).
```
Figure 21. Prolog businessService tModel fact

4.3 Prolog UDDI API

The Prolog realization of the UDDI model implemented in the prototype omits some of the capabilities of the UDDI API. The search capabilities maintained are find_service and find_tModel. The Prolog implementation of find_service has the following arguments: Name, Description, BusinessTemplate, CategoryBag, ServiceKey, BusinessKey, ServiceList, and, Operator. The Operator argument can have values *OR* and *AND* which performs logical operations on the search parameters. If Operator is NULL the default behavior is logical AND. If the CategoryBag argument is not NULL, the find_tModel/2 predicate is invoked to find syntactic matches among the registered services' categoryBags.

4.4 Sensor service interface

The sensor service interface intercepts service requests to the UDDI repository and invokes matchmaking services, if specified by the requestor. If the requestor does not specify semantic matchmaking, the service request is passed to the UDDI repository. Shown in Figure 22 is a state-chart diagram depicting the process of the sensor service interface attempting to satisfy a find_service query.
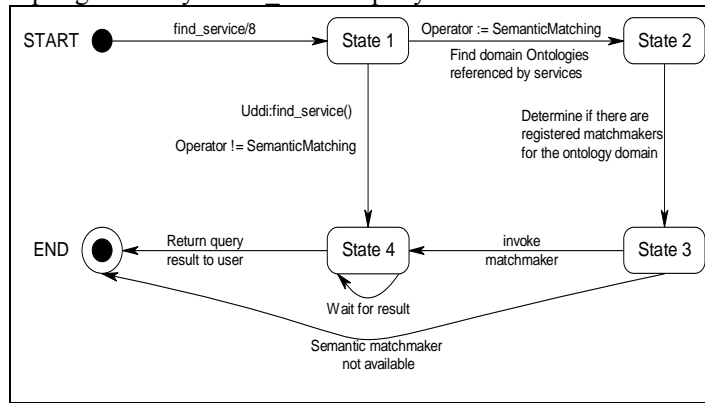

Figure 22. Sensor service interface state-chart diagram

The Operator argument of the find_service permits the values *AND*, *OR*, and *SemanticMatch*. If the argument does not have the value *SemanticMatch*, the service request is passed to the UDDI repository. Otherwise, the sensor service interface searches the UDDI repository to find the ontologies referenced by the services. The matchmaker then searches the UDDI registry for matchmakers that perform matchmaking services within the domain of the referenced ontology. If a matchmaker is discovered, it is invoked using the API invocation command described in the service description.

4.5 Semantic sensor matchmaker

The semantic sensor matchmaker is capable of performing generalization, specialization, performance property, supported applications, and instance semantic processing. The query command lists that control the behavior of the sensor matchmaker along with the corresponding predicates invoked are shown in Table 1. The valid operations that can be performed on query command list results are shown in Table 2.

Table 1. API query definitions

API Query Commands	Description
['specializationOf', CLASS]	Invokes find_specialization/2 predicate. Find specialization of argument CLASS.
['generalizationOf', CLASS]	Invokes find_generalization/2 predicate. Find generalization of argument CLASS.
['supportedApplication', Capability]	Invokes application_query/2 predicate. Find sensor service that has the supported application Capability.
[Object, Value]	Invokes find_performance/2 predicate. Find sensor service that has performance property Object and Value. If the performance_query/2 predicate fails then instance_query/2 predicate is invoked to attempt to satisfy the query. The instance_query/2 predicate loads instance metadata for the services to satisfy the query.

Table 2. Operations on query lists

List Operation	Description
['OR', QueryList]	Performs logical OR on QueryList result.
['AND', QueryList]	Performs logical AND on QueryList result.
[OP1, OP2, OP3, List1, List2]	Performs OP1(OP3(List2), OP2(List1)). OP1, OP2, and OP3 perform logical OR or AND operations

The SWI-Prolog Semantic Web library (Wielemaker et al., 2003) is used in the prototype to load and query external ontologies. The rdf_db module is used to assert OntoSensor into the Prolog knowledge base as RDF triples. The rdf_load/1 predicate is used to load the OntoSensor ontology into rdf/3 facts with arguments that can be viewed as Subject, Verb, and Object. The RDF triples are queried using Prolog predicates.

The matchmaker retrieves the services in the UDDI registry that subscribe to OntoSensor. The UDDI find_service/7 predicate is used to narrow the search space for the matchmaker as well as to minimize the number of queries issued to the UDDI model. Locating the services that subscribe to the domain ontology OntoSensor requires only one call to the UDDI registry.

The semantic processing continues until the list of query commands is exhausted. Once the list is empty, the operations in Table 2 are performed, if specified. The RDF triples are retracted from memory and the result of the semantic processing is then returned to the sensor service interface. Retracting the RDF triples from the matchmaker's knowledge base introduces computational overhead. The ontology used by the matchmaker can be updated and requires reloading RDF triples into Prolog's memory for each request. A paging methodology or expiration window for reloading the ontology could circumvent the computational overhead, but that process is beyond the scope of the initial prototype.

4.5.1 Specialization query

The specialization processing of a query for sensor services satisfying a given sensor type constraint is performed by invoking the Prolog predicate is_platform_specialization/3 developed for the prototype. A unique list of deployed platforms (note that a platform may contain several sensor types) is created from the UDDI list of registered sensor services and is one argument of the is_platform_specialization/3 predicate. The predicate uses depth-first search to determine if one of the platform's sensors is a specialization of the sensor type specified in the query. In the prototype, the argument, which is the sensor type to be specialized in the original query, must be a class in OntoSensor. This argument is used as the root node to produce a sensor-type taxonomic hierarchy that will serve as a search tree. The subtree produced from the root node is searched to determine if a deployed sensor is an instance of a class within the subtree. If a class is found in which a registered sensing component is an instance, the corresponding sensor service is accumulated in a list and the search resumes until the registered service list is empty. If matches are found, the portion of the semantic data model pertinent to satisfying the query is stored in the UDDI tModels via the methodology discussed in Section 4.2.

4.5.2 Generalization query

The generalization processing implemented in the prototype discovers registered sensor services that are direct members of a generalization of the specified class in the query or sensor services that are members of a specialization of one or more of the generalized classes. The generalization processing is performed by the find_generalization/3 predicate, which works in two steps using the predicates find_generalization/3 and is_platform_specialization/3. The predicate find_generalization/3 searches for the classes that are a generalization of the sensor type specified in the query, which must be a class specified in OntoSensor. The predicate is_platform_specialization/3 is invoked to find specializations of the generalized classes.

Determining the appropriate degree of generality for a query is beyond the scope of the current implementation of the prototype. Possible future approaches are to quantify the degree of generality needed to satisfy a particular query or to iteratively generalize the query until matches are found and there are no additional parent classes. The implementation in the prototype uses a very liberal definition of generalization. For example, the OntoSensor class *Sensor* is the most general sensor type, that is, it is the parent node for all sensor classes. The maximum extents of the generalization for a sensor type specified in a query are the direct subclasses of *Sensor*. These generalized classes serve as root nodes to generate subtrees consisting of sensor type subclasses. In the initial prototype implementation, the registered sensor platforms having components that are instances in this search space are considered instances of generalizations of the sensor type specified in the original query.

4.5.3 Supported application and performance property query

Figure 23 is an excerpt of a class diagram used in OntoSensor. A sensor's capabilities have been captured through the class *CapabilitiesDescription*. This class in turn is linked to the *GenericProperty* class through two associations. A specific sensor's sensitivity and resolution can be derived through query of the *performanceProperty* association. For example, noise equivalent temperature difference (NETD), which is one

gross measure of sensitivity, can be determined by obtaining the values of certain sensor parameters, such as focal length, horizontal and vertical field of view, frame rate, and overscan ratio. Through the supportedApplications association queries can determine the types of sensors to attempt to locate and task based on some application criteria like GPS capability, night operation capability, foliage penetration, all weather capability, etc.
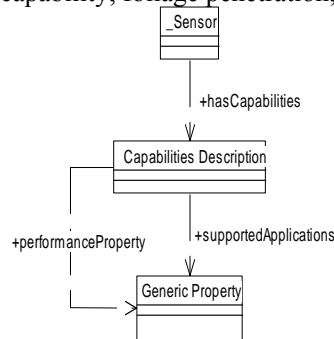

Figure 23. Capabilities description UML (Russomanno & Goodwin, 2007)

Two separate predicates are used for finding supported applications and performance processing in the prototype, but the process of satisfying the queries is similar. The *CapabilitiesDescription* facts are queried to determine if any of the registered sensors satisfy either the supported application or performance property constraint. The query processing continues until the unique list of registered services is exhausted. The semantic metadata used to satisfy the query is explicitly stored in the UDDI businessService tModel descriptions of the registered sensor services that satisfied the query.

Instance metadata for registered services is loaded, if the query cannot be satisfied through the matchmaker's performance property knowledge gained from OntoSensor. The external metadata is loaded into the matchmaker's knowledge base using the bindingTemplate of the businessService description, which contains the URI for obtaining the metadata. The metadata is loaded into the knowledge base and the matchmaker attempts to use the additional knowledge to satisfy the query. If a semantic match is found, the semantic data pertinent for satisfying the query is saved in the UDDI tModels via the methodology discussed in Section 4.2.

5.0 Conclusions

This paper has described an architecture and prototype implementation that integrates a sensor ontology within a service-oriented architecture (SOA) to support the development of expert system applications. The prototype environment supports the query of sensor services, which are registered in a UDDI-compliant repository, augmented with semantics and supports queries using generalization and specialization via reference to an external ontology, as well as queries of sensor performance properties, supported applications, and metadata about deployed sensor instances. The prototype was implemented utilizing Semantic Web infrastructure to overcome some of the limitations of the current service-oriented approaches that rely solely on XML-data structures and syntax-based search mechanisms for discovery of Web services.

145

Areas of future research and development include integrating the prototype environment with a geographical information system containing both land-base references, as well as inside plant or building graphics to aid in the discovery and query of sensors deployed in a variety of locations. The composition of sensor services with other Web services, including algorithms that take sensor data as input, perform an operation, and return a classification or output for processing by subsequent services, is also of high priority.

ACKNOWLEDGEMENT

REFERENCES

Akkiraju, R., Colgrave, J., Verma, K., Akkiraju, P. and Goodwin, R. (2007) "Dynamic Discovery and Binding of Web Services to Abstract Web Process Flows*," International Journal of Web Services Research,* To Appear.

Akkiraju, R., Goodwin, R., Akkiraju, P. and Roeder, S. (2003) "Method for Semantically Enhancing the Service Discovery Capabilities of UDDI," *Proceedings of the Workshop on Information Integration on the Web*, pp. 87-92.

Berners-Lee, T., Hendler, J. and Lassila, O. (2001) "The Semantic Web: A new form of Web Content that is meaningful to Computers will unleash a revolution of new possibilities," *Scientific American*, May, pp. 34-43.

Botts, M. et al. (2004) "Sensor Model Language (SensorML) for In-Situ and Remote Sensors," http://vast.nsstc.uah.edu/SensorML/Sensor.

Brickley, D., and Guha, R. V. (2000) "Resource Description Framework (RDF) Schema Specification," World Wide Web Consortium, http://www.w3.org/TR/2000/CR-rdf-schema-20000327.

Carman, M., Serafini, L. and Traverso, P. (2003) "Web service composition as planning," *International Conference on Automated Planning and Scheduling 2003 Workshop on Planning for Web Services*, 2003.

Chandrasekaran, B., Josephson, J. and Benjamins, V. (1999) "What are ontologies and why do we need them?" *IEEE Intelligent Systems*, 14(1):20-26.

Clement, L., Hately, A., Von Riegen, C. and Rogers, T. (2004) "UDDI Version 3.0.2," OASIS, Tech. Rep., http://uddi.org/pubs/uddi v3.htm.

CrossBow Technology Inc. (2006) *Wireless Sensor Networks: Product Reference Guide*.

Fensel, D., Harmelen, F. V. and Horrocks, I. (2003) "OIL and DAML+OIL: Ontology Languages for the Semantic Web," In *Towards the Semantic Web: Ontology-Driven Knowledge Management*, Davies, J., Fensel, D. and van Harmelen, F. (eds.), West Sussex, England: John Wiley & Sons, Ltd, pp. 11-31.

Genesereth, M. and Nilsson, N. (1987) *Logical Foundations of Artificial Intelligence*, Palo Alto, CA: Morgan Kaufmann.

Goodwin, J. C. and Russomanno, D. J. (2006) "An Ontology-Based Sensor Network Prototype Environment," *Fifth International Conference on Information Processing in Sensor Networks*, http://www.cs.virginia.edu/~ipsn06/WIP/goodwin_1568983444.pdf.

Goodwin, J. C. and Russomanno, D. J. (2007) "Survey of Semantic Extensions to UDDI: Implications for Sensor Services," *The 2007 International Conference on Semantic Web and Web Services*, pp. 16-22.

Lenat, D. and Guha, R. V. (1989) *Building Large Knowledge-Based Systems: Representation and Inference in the CYC Project*, Reading, MA: Addison-Wesley.

Luo, J., Montrose, B. and Kang, M. (2005a) "Adding Semantic Support to Existing UDDI Infrastructure," *Report No. NRL/MR/5540—05-8918*, Naval Research Laboratory, Code 5542.

Luo, J., Montrose, B., and Kang, M. (2005b) "An Approach for Semantic Query Processing with UDDI,*" First International Workshop on Agents, Web Services, and Ontology Merging*.

McGuinness, D. (2003) "Ontologies Come of Age," In *Spinning the Semantic Web*, Fensel, D., Hendler, J. Lieberman, H., and Wahlster, W. (eds.), Cambridge, MA: MIT Press, pp. 171-195.

Niles, I. and Pease, A. (2001) "Towards a Standard Upper Ontology," *The Second International Conference on Formal Ontology in Information Systems,* pp. 2-9.

Noy, N., Sintek, M., Decker, S., Crubezy, M., Fergerson, R. and Musen, M. (2002) "Creating Semantic Web Contents with Protégé-2000," *IEEE Intelligent Systems*, 16(2):60-71.

Paolucci, M., Kawamurea, T., Payne, T. and Sycara, K. (2002a) "Importing the Semantic Web in UDDI," *Proceedings of Web Services, E-Business, and Semantic Web Workshop*, pp. 225-236.

Paolucci, M., Kawamura, T., Payne, T. and Sycara, K. (2002b) "Semantic Matching of Web Services Capabilities," *Proceedings of the First International Semantic Web Conference*, pp. 333-347.

Peer, J. (2005) "Web service composition as AI planning - a survey," Technical report, University of St. Gallen, Switzerland.

Pistore, M., Barbon, F., Bertoli, P., Shaparau, D. and Traverso, P. (2004) "Planning and monitoring web service composition," *Proceedings of Planning and Monitoring Web Service Composition Artificial Intelligence: Methodology, Systems, and Application.*

Russomanno, D. J., Kothari, C. and Thomas, O. (2005a) "Building a Sensor Ontology: A Practical Approach Leveraging ISO and OGC Models," *The 2005 International Conference on Artificial Intelligence*, pp. 637-643.

Russomanno, D. J., Kothari, C. and Thomas, O. (2005b) "Sensor Ontologies: From Shallow to Deep Models," *Proceedings of the 37th Southeastern Symposium on Systems Theory*, pp. 107-112.

Russomanno, D. J. and Goodwin, J. C. (2007) "OntoSensor: An Ontology for Sensor Network Application Development, Deployment, and Management," In *Handbook of Wireless Mesh and Sensor Networking*, G. Aggelou (ed.), New York, NY: McGraw Hill, To Appear.

Singh, M. and Huhns, M. (2005) *Service-Oriented Computing*, West Sussex, UK: John Wiley & Sons.

Sivashanmugam, K., Verma, K., Sheth, A. and Miller, J. (2003) "Adding Semantics to Web Service Standards," *Proceedings of the 1st International Conference on Web Services,* pp. 395-401

Skuce, D. and Monarch, I. (1990) "Ontological Issues in Knowledge Base Design: Some Problems and Suggestions," *CMU-CMT-90-119,* Pittsburgh, PA: Carnegie Mellon U.

Smith, M., et al. (2003) "OWL Web Ontology Language Guide: W3C Proposed Recommendation," Available at: http://www.w3.org/TR/2003/PR-owl-guide-20031215/.

Srinivasan, N., Paolucci, M. and Sycara, K. (2004) "Adding OWL-S to UDDI, Implementation and Throughput," *First International Workshop on Semantic Web Services and Web Process Composition*, pp. 6-9.

Stanford Medical Informatics (2004) "The Protégé Ontology Editor and Knowledge Acquisition System," http://protege.stanford.edu/.

Uschold, M. and Gruninger, M. (1996) "Ontologies: Principles, Methods, and Applications," *Knowledge Engineering Review*, 11(2):93-115.

Wielemaker, J., Schreiber, G. and Wielinga, B. (2003) "Prolog-Based Infrastructure for RDF: Scalability and Performance," *Second International Semantic Web Conference*, pp. 644-658.

8.2 Appendix B

Develop Image Quality Metrics for Fused Imagery

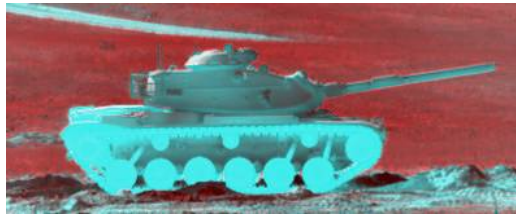**Figure 5: 8-bit visible TV image.**

Figure 6: MWIR image

Figure 7: Color Fused image to show registration

Figure 8: Pixel-averaged (superposition) image
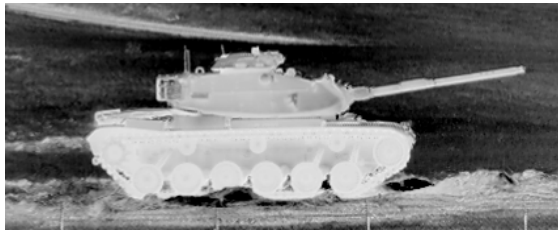
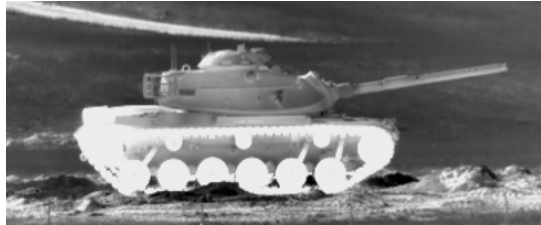**Figure 9: Opponent A processing**

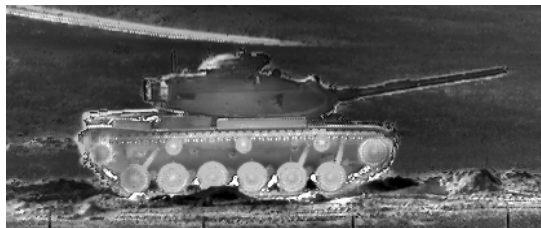**Figure 10: Multiscale image fusion**

Figure 11: Laplacian A image fusion

Figure 12: Contrast Ratio A image fusion

Figure 13: Discrete wavelet (DWT) image fusion

152

Figure 14: Shift invariant DWT image fusion

Figure 15: Gabor image fusion

Figure 16: Principal component analysis image fusion

Figure 17: Pixel averaging image fusion